

University of Alberta

Novel Materials for the Design of Cantilever Transducers

by

Nathaniel Nelson-Fitzpatrick

A thesis submitted to the Faculty of Graduate Studies and Research
in partial fulfillment of the requirements for the degree of

Doctor of Philosophy

in

Micro-Electro-Mechanical Systems (MEMS) and Nanosystems

Department of Electrical and Computer Engineering

©Nathaniel Nelson-Fitzpatrick

Fall 2011

Edmonton, Alberta

Permission is hereby granted to the University of Alberta Libraries to reproduce single copies of this thesis and to lend or sell such copies for private, scholarly or scientific research purposes only. Where the thesis is converted to, or otherwise made available in digital form, the University of Alberta will advise potential users of the thesis of these terms.

The author reserves all other publication and other rights in association with the copyright in the thesis and, except as herein before provided, neither the thesis nor any substantial portion thereof may be printed or otherwise reproduced in any material form whatsoever without the author's prior written permission.

To Dennis and Caryl

Abstract

Micro and nanocantilever structures have been used as transducers for a plethora of sensor applications. These transducer technologies have similar shapes, but the material properties and geometrical optimizations needed to improve sensitivity are rather different. This is a record of two different material and design strategies undertaken for static and resonant cantilever sensors.

For resonant cantilever sensors we desire a material that is stiff and light. We fabricated silicon nanocantilevers using electron beam lithography and a cryogenic etching technique and assayed their resonance frequencies. The brittle nature of surface machined Si necessitated the move towards nanocantilevers made from glassy materials like Si_3N_4 and SiCN , which are difficult to deposit reliably in thicknesses below 50 nm. Alternatively, we fabricated and characterized atomic layer deposited (ALD) TiN films for nanocantilevers. We assayed chemical and physical characteristics of TiN films deposited between 120°C and 300°C with XPS, XRD, ellipsometry, and wafer bowing. We then fabricated nanoresonator beams out of TiN deposited at 200°C .

For static cantilever sensors we designed an Au-Ta nanocomposite alloy. Combining Au and Ta using magnetron co-sputtering we synthesized a material

with low intrinsic stress while retaining the chemical affinity of Au to thiolized molecules. XRD, SEM, AFM, nanoindentation, stress measurements and nanocantilever resonance tests were performed to determine the bulk and surface characteristics of these Au-Ta alloys. The FCC $\langle 111 \rangle$ structure of Au was retained in films below 50 at.% Ta. Young's modulus was increased slightly by the addition of Ta while hardness was increased fivefold. The film's deposited stress was relieved upon inclusion of 5 at.% Ta. Chemical characteristics of Au-Ta films over the range of Pure Au to Au 40 at.% Ta was assessed using contact angle measurements, XPS, FTIR and cantilever measurements. As Ta concentration was increased the binding of 1-dodecanethiol was hindered. Low Ta films (5 and 10 at.% Ta) exhibited reduced but significant thiol binding, while higher concentrations displayed insignificant binding. We fabricated geometrically optimized cantilevers with a theoretical spring constant as low as $10.5 \frac{mN}{m}$. The detection of dodecanethiol was demonstrated with these cantilevers, confirming intrinsic sensitivity to thiolized molecules.

Acknowledgements

I want to thank my supervisor, Dr. Stéphane Evoy for the opportunity to work on this project and his helpful insights over the course of it. I would also like to acknowledge the staff of the Nanofab (in particular Dr. Ken Westra, Keith Franklin, Les Schowalter and Scott Munro) for their helpful advice regarding the fabrication aspects of this project. I would also like to thank Colin Ophus, Nick Glass, Vince Sauer, Steve Buswell, Ravendra Naidoo, Jason Ng, and Nilufar Poshtiban for being great sources of technical expertise and personal advice. Nick in particular was a great labmate who was always motivating me to work late into the night and on weekends to try new ideas and techniques, I am indebted to him. Ishan Sharma also deserves special recognition, though our work together did not yield anything directly the experience helped me greatly in static cantilever experiments. Amit Singh, David Rider, Ken Harris and Brian Worfolk deserve special thanks for always being open to answering my questions regarding chemistry. I would also like to thank Amit Singh and Nilufar Poshtiban for their help in proofreading this work. My friends Sam Johnson and Christine Wilson and Ian Roberge deserve recognition for helping me keep my sanity when things weren't working in the lab. Lastly, there was the support of Haley Zaharia who is my everything.

Nomenclature and Abbreviations

AFM	Atomic force microscope
ALD	Atomic layer deposition
BCC	Body-centred cubic
BOE	Buffered oxide etch
BOx	Buried oxide
BSA	Bovine serum albumin
CMOS	Complimentary metal-oxide semiconductor
CVD	Chemical vapour deposition
DC	Direct current
DI	Deionized water
DNA	Deoxyribonucleic acid
DRIE	Deep reactive ion etch

ELISA	Enzyme-linked immunosorbent assay
FCC	Face-centred cubic
FTIR	Fourier transform infrared spectroscopy
FWHM	Full width half maximum
HF	Hydrofluoric acid
HRTEM	High resolution transmission electron microscopy
IC	Integrated circuit
IPA	Isopropyl alcohol
KOH	Potassium hydroxide
LN ₂	Liquid nitrogen
LPCVD	Low pressure chemical vapour deposition
MEMS	Microelectromechanical systems
MIBK	Methylisobutylketone
MOCVD	Metal organic chemical vapour deposition
NEMS	Nanoelectromechanical systems
OPL	Optical path length

PBS	Phosphate buffer saline
PC	Personal computer
PDE	Partial differential equation
PDMS	Polydimethylsiloxane
PECVD	Plasma enhanced chemical vapour deposition
PMMA	Polymethyl methacrylate
PSA	Prostate specific antigen
PSD	Position sensitive detector
PVD	Physical vapour deposition
PZT	Lead zirconate titanate
QCM	Quartz crystal microbalance
RF	Radio frequency
RIE	Reactive ion etch
RMS	Root mean square
SAM	Self-assembled monolayers
SAW	Surface acoustic wave

SEM	Scanning electron microscope
SIMOX	Separation by implantation of oxygen
SMR	Suspended microchannel resonator
SOI	Silicon on insulator
SPR	Surface plasmon resonance
ssDNA	Single-stranded deoxyribonucleic acid
SWLI	Scanning white light interferometry
TMAH	Tetramethyl ammonium hydroxide
VASE	Variable angle spectroscopic ellipsometry
VOC	Volatile organic compound
XPS	X-ray photoelectron spectroscopy
XRD	X-ray diffraction

Contents

1	Introduction	1
1.1	The Promise of Small: MEMS, NEMS, and Nanotechnology . . .	1
1.1.1	Feynman Talk and Nanotechnology	1
1.1.2	MEMS	3
1.1.3	NEMS	5
1.2	Biological and Chemical Sensors	7
1.2.1	What is a Sensor	7
1.2.2	Motivation for Biosensors	9
1.2.3	Motivation for Chemical Sensors	11
1.2.4	Sensor Technologies for Biological and Chemical Sensors	12
1.3	Micro/Nanocantilever Background	19
1.3.1	Why Micro/Nanocantilevers?	19
1.3.2	Previous Work in Micro/Nanocantilever Chemical Sensors	21
1.3.3	Previous Work in Micro/Nanocantilever Biological Sensors	23
1.4	Rationale and Thesis Outline	26
1.4.1	Metal Nanocomposites	26
1.4.2	ALD synthesized materials	28
1.4.3	Outline	29

2	Cantilevers	30
2.1	Introduction	30
2.2	Fabrication Methodologies	31
2.2.1	Bulk Machining	31
2.2.2	Surface Machining	35
2.3	Dynamic Versus Static Cantilever Operation	37
2.4	Dynamic Mode	38
2.4.1	Spring Constant	38
2.4.2	Euler-Bernoulli	40
2.4.3	Quality Factor and Losses	42
2.4.4	Mass Sensitivity	45
2.5	Static Mode	47
2.5.1	Stoney's Equation	48
2.5.2	Stress Sensitivity	49
2.6	Contrasting Transduction Methods	51
2.7	Readout Methods	51
2.7.1	Optical Methods	52
2.7.2	Electrical Methods	57
2.8	Summary	60
3	Silicon Nanocantilevers	61
3.1	Introduction	61
3.2	Silicon on Insulator	61
3.3	Cantilever Fabrication	62

3.3.1	Electron Beam Lithography	64
3.3.2	Cryogenic Reactive Ion Etch	65
3.4	Resonance Data	68
3.5	Summary	71
4	Gold Tantalum Material Development	73
4.1	Introduction	73
4.2	Metals as a Structural Material for Cantilever Transducers	74
4.3	Physical Vapour Deposition and Sputtering	76
4.4	Generalized Method for Sputtering Metal Alloys with Stoichiometric Control	79
4.5	Film Characterization	82
4.5.1	X-Ray Diffraction	82
4.5.2	Microscopy	85
4.5.3	Film Stress	89
4.5.4	Film Resistivity	90
4.5.5	Nanoindentation	91
4.6	Fabrication of Cantilevers	94
4.7	Resonance Data	96
4.7.1	Room Temperature	97
4.7.2	Cryogenic	101
4.8	Finite Element Modelling	102
4.9	Summary	107

5	Gold Tantalum Static Cantilevers	109
5.1	Introduction	109
5.2	Background	110
5.3	Self-Assembled Monolayers	112
5.4	Contact Angle Measurements	114
5.5	X-Ray Photoelectron Spectroscopy	117
5.6	Fourier Transform Infrared Spectroscopy	122
5.7	Au-Ta Coated Silicon Cantilevers	124
5.7.1	White Light Interferometry	125
5.7.2	Temperature Sensitivity	126
5.7.3	Stress Induced by Dodecanethiol Attachment	128
5.8	Gold-Tantalum Cantilevers	130
5.8.1	Fabrication	130
5.8.2	Alternate Release Methods	133
5.8.3	Initial Conditions	133
5.8.4	Sensitivity Comparison	135
5.8.5	Stress Induced by Dodecanethiol Attachment	137
5.9	Summary	139
6	Atomic Layer Deposition Cantilevers	141
6.1	Introduction	141
6.2	ALD Background	142
6.3	Film Thickness and Deposition Rates	145
6.4	Film Stress	148

6.5	X-Ray Diffraction	150
6.6	X-Ray Photoelectron Spectroscopy	152
6.7	Cantilever Resonator Fabrication	157
6.8	Summary	159
7	Conclusions	161
7.1	Summary	161
7.2	Future Directions	164
 Appendices		
A	Appendix	194
A.1	Wafermap for Static Au-Ta cantilevers	194
B	Appendix	197
B.1	Reactive Sputter Background	197
B.2	XPS	198
B.3	Stress	200
B.4	Fabrication	200
C	Appendix	203
C.1	AFM, Nanoindentation and Stress measurement Data for Au-Ta films	203
D	Appendix	207
D.1	Analysis for speed of sound in Au-Ta nanocantilevers	207

List of Tables

2.1	Values of βL that satisfy equations 2.19 and 2.25	43
2.2	Summary of suitable environments, sources of noise and desirable properties for static and dynamic cantilever transducers. .	51
3.1	Process steps for cryogenic etching.	68
3.2	Summary of physical values of SOI material as measured by the resonating cantilever beam method.	72
4.1	Resonant frequencies and quality factors of a series of Au-Ta 5% at. Ta cantilevers with width $w = 800$ nm and thickness $t = 51$ nm.	98
4.2	Summary of the mechanical properties used in COMSOL finite element modelling of eigenfrequencies of Au-Ta 5% cantilever resonators.	104
4.3	Summary of the speed of sound of COMSOL cantilever models and comparison to measured values	105
5.1	Theoretical temperature-induced tip deflection and stress noise in Ti/Au coated Si cantilevers, Ti/Au coated SU-8 cantilevers, the most stress sensitive Au-Ta “metal-only” cantilever fabricated (with 10 nm Ta adhesion layer), and the same Au-Ta cantilever scaled up to $500\mu\text{m}$ long (a common length for commercial static cantilever sensors). Values are calculated from equations 5.2 and 5.3	127
5.2	Comparison of spring constants of recently published and commercially available highly compliant microcantilevers and the Au-Ta cantilevers fabricated in this study.	136

6.1	Mechanical properties for CVD synthesized Nitrides and Oxides (1)	144
6.2	ALD TiN deposition recipe used in this chapter. All films were deposited for 3000 cycles.	145
6.3	ALD TiN composition as determined by X-ray photoelectron spectroscopy. Note that as Temperature is increased Ti / N ratio approaches 1.	153
B.1	Reactively sputtered TiN recipe summary	197
B.2	Reactively sputtered TiN composition as determined by X-ray photoelectron spectroscopy.	198
B.3	Deposited stress of reactively sputtered TiN films.	200
C.1	Data from nanoindentation testing - Nanohardness	204
C.2	Data from nanoindentation testing - Reduced modulus	204
C.3	Data from nanoindentation testing - Contact depth	205
C.4	Data from atomic force microscopy testing - roughness	205
C.5	Data from film stress testing	206
D.1	Assayed cantilever data - Au-Ta nanocantilever beams	209

List of Figures

1.1	Schematic diagram of an Atomic Force Microscope.	6
1.2	Generalized block diagram of a sensor	8
1.3	Schematic diagram of an Quartz Crystal Microbalance	12
1.4	Schematic diagram of an Love-wave type Surface Acoustic Wave transducer.	14
1.5	Schematic diagram of a prism coupler based SPR sensor	16
2.1	Process flow for fabricating a bulk machined cantilever. Step 1: start with a Clean Si wafer with implanted p ⁺⁺ layer. Step 2: Use photolithography to define the cantilever shape. Step 3: Etch down through the etch stop layer using a fluorine RIE. Step 4: Protect top and bottom with a mask to prevent KOH etching(Protek, SiO ₂ , Si ₃ N ₄). Step 5: Use lithography to open up a window on the backside for KOH etch. Step 6: Perform KOH etch. Step 7: Remove protective mask layer.	33
2.2	The process of a cantilever undergoing stiction. First, the cantilever is immersed in deionized water. Second, the cantilever is being pulled towards the substrate by capillary force. Lastly, the cantilever comes into contact with the substrate and is bonded by Van der Waals forces.	36

2.3	Process flow for fabricating a surface machined cantilever. Step 1: Start with a clean SIMOX wafer. Step 2: Define a cantilever shape with photolithography. Step 3: Etch down to buried oxide with a fluorine RIE. Step 4: Release the cantilever by etching away the buried oxide below it with an HF based etchant. (critical process drying may be required depending on device dimensions)	37
2.4	Sample cantilever resonance spectra, with half power and frequency bandwidth annotated.	44
2.5	Schematic diagram of the bending of a substrate due to stress induced by the deposition of a compressive or tensile thin film.	48
2.6	Schematic diagram of a cantilever undergoing bending due to surface stress	50
2.7	Schematic diagram of a resonance assaying interferometer setup.	54
2.8	Graph of intensity vs difference in optical path length for a white light interferometer. As the optical path lengths of the two arms of the interferometer become further apart the fringe intensity is drastically reduced.	55
2.9	Schematic diagram of a white light interferometer setup.	57
3.1	Output from CASINO simulation displaying electron trajectories for 10kV and 30kV electron beam lithography spot.	65
3.2	Illustration of anisotropic and isotropic etch profiles on a trench feature.	66
3.3	Schematic diagram of the cryogenic reactive ion etch process. Silicon oxyfluoride passivation is deposited all over the trench structure. The passivation layer is etched physically by ion bombardment exposing the trench bottom to chemical attack from radical species.	67
3.4	150 nm wide silicon cantilever beam etched by cryogenic process and released with buffered HF and CPD. Artifacts below the cantilever are believed to be an artifact of the SOI synthesis and unrelated to our processing.	69
3.5	Resonance spectra of the first mode of a 400 nm wide, 4 μ m long, 200 nm thick silicon cantilever etched using the cryogenic RIE process.	70

3.6	Frequency vs cantilever length plot for 400nm wide SOI cantilever beams. Note that error bars corresponding to frequency measurement are vastly smaller than the data point icons.	71
4.1	Schematic diagram of a magnetron co-sputter system used to deposit Au-Ta alloy films.	77
4.2	Calibration plot of deposition rate versus sputter gun power for Au and Ta used to control for stoichiometry of the film. Note that the introduction of extra electrons in the plasma by co-sputtering causes a minor $\sim 2\%$ variation in Ta deposition rate versus applied power.	80
4.3	X-ray diffraction scans of Au-Ta films of different compositions	83
4.4	Au-Ta lattice parameters calculated from the $\langle 222 \rangle$ XRD peaks, with Vegard's law plotted for the first five points.	84
4.5	Scanning electron micrographs of various Au-Ta concentrations	86
4.6	Atomic force micrographs of various Au-Ta concentrations	87
4.7	Film roughness versus Au-Ta composition	88
4.8	Au-Ta film stress vs. Ta content for a 400nm film. Error bars correspond to the standard deviation of six separate wafer bowing measurements 30° apart.	89
4.9	A semi-logarithmic plot of Au-Ta electrical resistivity as a function of Ta content. A best fit to Nordheim's rule is superimposed onto the datapoints.	91
4.10	Graph of nanoindentation hardness versus Ta concentration for a series of Au-Ta films, as measured by nanoindentation. The error bars in this graph were obtained by the standard deviation of 25 separate indentation tests performed on each composition film.	92
4.11	Graph of elastic modulus versus Ta concentration for a series of Au-Ta films, as measured by nanoindentation. The error bars in this graph were obtained by the standard deviation of 25 separate indentation tests performed on each composition film.	93
4.12	Process flow illustration for the fabrication of resonant Au-Ta nanocantilevers.	95

4.13	Scanning electron micrograph of an Au-Ta nanocantilever with dimensions $w = 800$ nm, $t = 51$ nm, $l = 3$ μm	97
4.14	Resonant response of an Au-Ta 5 at. % Ta cantilever with a length $L = 5$ μm , width $w = 800$ nm and thickness $t = 51$ nm.	98
4.15	Resonance quality Q as a function of pressure for a Au-Ta 5% at. Ta cantilever with dimensions $L = 5\mu\text{m}$, $w = 800$ nm, $t = 51$ nm, and a resonant frequency of 708 kHz.	99
4.16	Linearized graph of resonance frequency versus length for a series of cantilevers Au-Ta 5% at. Ta with dimensions $w = 800$ nm and $t = 51$ nm. The fit of data to equation 3.1 provides a speed of sound ($\sqrt{\frac{E}{\rho}}$) of $2493.64 \pm 132.19 \frac{m}{s}$	100
4.17	Measured quality factor versus substrate holder temperature for a $3\mu\text{m}$ long, 800 nm wide, 51 nm thick Au-Ta cantilever.	102
4.18	Illustration of the cantilever geometry constructed in COMSOL 3.5a for finite element simulations of resonance frequency.	103
4.19	Fundamental resonance frequency vs number of mesh elements for a $1\mu\text{m}$ long 800 nm wide Au-Ta cantilever.	105
4.20	Fundamental resonance frequency vs cantilever length for measured cantilevers (black lozenges) and COMSOL modeled cantilevers using a reference value for Young's modulus (red squares) and a nanoindentation derived for Young's modulus (green triangles).	106
5.1	Diagram of the chemical structure of dodecanethiol	113
5.2	Diagram highlighting the organization of S atoms (large green circles) from Alkanethiols on the $\langle 111 \rangle$ surface of Au (smaller yellow circles).	113
5.3	Diagram of three phases of SAM formation. Firstly, alkanethiols bind to the Au surface with alkane chain lying down on the Au surface. Second, as SAM formation evolves thiol molecules transition into a denser stacked lying down phase. Finally SAM reaches its fully formed "standing up" phase.	115
5.4	Images from contact angle goniometer. Left: Deionized water droplet on clean Au. Right: Deionized water on Au exposed to dodecanethiol vapour for 2 hours.	116

5.5	Contact angle of deionized water versus Ta content in Au-Ta film for clean and dodecanethiol exposed films.	117
5.6	X-ray photoelectron spectroscopy curves for dodecanethiol exposed Au-Ta films. Two peaks are visible, one at 168 eV corresponding to nonspecific, unbound SO_x and one at 162 eV corresponding to elemental S from bound dodecanethiol molecules. Control samples showed only peaks at 169 eV.	118
5.7	Bargraph of proportion of X-ray photoelectron spectroscopy counts attributed to SO_x and elemental S. As Ta is introduced to the Au-Ta films the proportion of elemental S decreases, corresponding to decreased dodecanethiol formation efficiency. . .	120
5.8	Bargraph of carbon signal for a series of clean (control) and dodecanethiol exposed Au-Ta films.	121
5.9	FTIR absorption spectra peaks of dodecanethiol on Au-Ta 5% film. Peaks between 2850 cm^{-1} and 3000 cm^{-1} correspond to absorption by CH_3 and CH_2 bonds of alkane chain.	123
5.10	Stress induced by the attachment of dodecanethiol on silicon cantilevers coated with a series of Au-Ta compositions. As Ta content is increased induced stress decreases, corresponding to poorer dodecanethiol binding.	129
5.11	Process flow for the fabrication of Au-Ta 5% static microcantilever transducers.	131
5.12	Scanning electron micrograph of a static Au-Ta 5% microcantilever with dimensions $l = 140 \mu\text{m}$, $w = 20\mu\text{m}$ and $t = 370 \text{ nm}$	132
5.13	Stress gradient of identically deposited Au-Ta 5% cantilevers with varied release times. Stress gradient was also obtained for the same cantilever samples after UV- O_3 cleaning.	135
5.14	Deflection versus stress sensitivity for a suite of Au-Ta 5% cantilevers exposed to dedecanethiol. Cantilever deflections correspond to an induced stress of $\sim 1.07 \frac{\text{N}}{\text{m}}$ after two hours dodecanethiol exposure.	138

6.1	Thickness of 3000 cycle TiN films deposited at different temperatures. Red squares are measurements taken with a filmetrics reflectometer and blue lozenges are measurements taken with a spectroscopic ellipsometry.	147
6.2	Stress of ALD deposited TiN films by deposition temperature. Blue lozenges represent the measured stress while the green line is the ideal stress due to thermal mismatch. The red squares represent stress not due to thermal mismatch sources.	149
6.3	XRD scans of the <200> peak of TiN. This was the only peak in the XRD scan that could not be attributed to the Si wafer.	151
6.4	Crystallite size derived by application of Scherrer's formula to XRD scans of the <200> peak of TiN.	152
6.5	Bargraph of TiN film composition by temperature. As temperature increases we see a decrease in O and Cl and an increase in N. Cl is attributed to unreacted TiCl ₄ precursor and O is attributed to oxidation of unreacted Ti.	154
6.6	High resolution XPS spectra of ALD synthesized TiN films.	156
6.7	Scanning electron micrograph of a fabricated TiN beam resonator from the 200°C deposition run. Beam dimensions are 11.3μm long, 30 nm wide and 72.9 nm thick.	158
A.1	Mask pattern for the AuTa static cantilevers.	195
A.2	One cell of AuTa static cantilever mask, with cantilever dimensions.	196
B.1	High resolution XPS scans of Ti, N and O for reactively sputtered TiN films.	199
B.2	Scanning electron micrograph of a beam structure fabricated from reactively sputtered TiN. All beams fabricated in this manner experienced similar fracturing.	202
D.1	Plot of inverse square root of frequency versus cantilever length for Au-Ta 5% nanocantilevers	210

CHAPTER 1

A Case for Cantilever Sensors, From The Feynman Talk to Today

1.1 The Promise of Small: MEMS, NEMS, and Nanotechnology

1.1.1 Feynman Talk and Nanotechnology

There has been much talk and fascination about the advent of nanotechnology over the past ten to twenty years (2). Richard Feynman's speech "There's Plenty of Room at the Bottom" (3) is seen by many scientists and science writers as the genesis of the field of nanotechnology. In his speech to the 1959 meeting of the American Physical Society, Feynman outlined that the problems faced by chemists and biologists could be greatly alleviated by being able to see the processes that they intended to study. The resolution of electron microscopes then was one hundred times too poor to image the structures and processes that biologists were describing; like the structure of DNA (4). Inspired by the efficiency with which nature could store the genetic information for remarkably complex life in such a small volume, Feynman outlined the unexplored possibilities of being able to manipulate matter on the atomic

scale. His talk pulled examples from biology, chemistry, physics and computer science and was hugely prescient in that the field of nanotechnology has been notable for its interdisciplinary nature.

The National Science Foundation of the United States has outlined that “The essence of nanotechnology is the ability to work at the molecular level, atom by atom, to create large structured with fundamentally new molecular organization” (5). They highlight that as materials are scaled down below 100 nm their physical, chemical and biological characteristics change so that they are no longer similar to the bulk characteristics that scientists and engineers are already familiar with. These scale induced changes in characteristics arise from the increased influence of interfacial and quantum mechanical phenomena. Chemists and biologists have been working with molecules of these characteristic dimensions for a very long time, but the newly found ability to characterize and control matter at these scales are the reason behind all the fuss being made over nanotechnology today. The advent of advanced electron and probe microscopy (6) techniques have brought the mechanisms studied by physics, biology and chemistry in to view at the same time enabling scientists to see the complimentary nature of their techniques at this atomic scale.

Most authors separate the tools and methods of manipulating matter at the nanoscale into two categories, “Top Down” and “Bottom Up” when describing nanotechnology. Bottom up nanofabrication is the approach whereby nanostructures are assembled from individual atoms or molecules, and the tools of the trade in this field are very diverse. These tools largely originate from the understanding of molecules that chemists have discovered over centuries and the exploitation of the tools of natural life by biologists. Examples of chemistry inspired bottom up nanofabrication would be to exploit the phenomena of self assembled monolayers (SAMs) (7), block copolymers (8; 9), use tools like templated electrodeposition (10) or nanoparticle catalyzed chemical vapour deposition (11; 12; 13). Some examples of biology inspired bottom up nanofabrication would be to exploit the highly selective binding characteristics of biological molecules like lipid bilayers (14), ssDNA, streptavidin-biotin (15),

or bacteriophages (16) in order to create layers of biomolecules. There are also physical tools like STM to manipulate individual atoms (17; 18) or dip pen nanolithography (19) to pattern molecules onto a surface. The self directed and highly parallel nature of many of these bottom up nanotools has made them a very attractive subjects for study but this very same nature often times make them difficult to control and exploit beyond a few niche applications.

Top down nanofabrication is the approach where techniques are used to take a bulk structure and remove matter in order to achieve the desired nanostructure. Common tools of the top down nanofabricator are optical and electron beam lithography, physical and chemical vapour deposition and reactive ion etchers. These are all tools that were developed by physicists and engineers and have strong ties to the meteoric improvements in integrated circuit technologies. Moore's law (20) is often talked about in nanotechnology because its prescient prediction of a doubling of integrated circuit components every 12 months (this later became 18 months, then 24 months). This prediction necessarily required that technologies used to fabricate these circuits would have to improve at a complimentary pace in order to accommodate so many transistors on a single silicon die. Many technologies for nanomachining have grown out of the fertile soil of silicon integrated circuits.

1.1.2 MEMS

Microelectromechanical systems or MEMS is an umbrella term for mechanical systems that are based on silicon microfabrication technologies. In Europe (21) the term "Microsystems" is used, as it is more inclusive and doesn't imply the need for electrical functionality. The discussion of MEMS in this thesis will take the widest possible view of the technological landscape, encompassing mechanical, electrical, thermal, magnetic, fluidic and optical interaction with the mechanical domain. MEMS are a branch off the growing tree of top down nanotechnology in that they are a family of devices who can tie their genesis to the maturity of silicon microfabrication technologies brought about by the IC

revolution and the economics of its parallel batch production methodologies (22). MEMS technologies have become ubiquitous in roles that require small, accurate and low cost sensors or actuators with the possibility of integration with active electronics. Examples of MEMS technologies include sensors (accelerometers (23), gyroscopes, pressure sensors), actuators (optical switches (24), digital light processors (25), read-write heads in disk drives), inkjet nozzles, and microfluidic devices for lab on a chip applications (though these are also commonly fabricated from Glass or PDMS (26)).

Silicon is an optimal material for so many applications that the advent of MEMS was an unavoidable consequence of the CMOS revolution. Silicon is the semiconductor of choice for microelectronics since it is plentiful, relatively cheaply manufactured into high purity single crystals and forms a stable oxide. Additionally, being a semiconductor, one could exploit the high piezoresistive gauge factors achievable with doped silicon to make a strain sensor that could be used for applications such as a pressure sensor membrane. Unfortunately, silicon is a rather brittle material with a low yield strength. This property can be viewed positively, since it implies that silicon MEMS are not prone to mechanical hysteresis (plastic deformation), but would fracture instead. This can be a positive feature if one desires an extremely accurate sensor without concern towards mechanical longevity. In the case where mechanical robustness is desirable in a sensor it would be preferable to employ polycrystalline or glassy materials like Poly-Si, Si_3N_4 , or bulk metallic glasses.

The unifying theme of the work in this thesis is the application of cantilever sensors and a prominent example of MEMS in the research environment is a cantilever sensor called the atomic force microscope (AFM).

Atomic Force Microscopy

The development of MEMS cantilever devices was initially motivated by the development of Atomic Force Microscopy (AFM) in 1986 by Binnig, Quate and Gerber (27). AFM is a form of scanning probe microscopy where a micro-

fabricated cantilever with an extremely sharp tip is brought into near-contact with a sample that is to be imaged and the cantilever is then scanned across the surface. In a tapping mode AFM, the cantilever is driven to resonance as it is scanned across the surface. An image of the sample is generated by the change in the cantilever's resonance frequency brought about by tip-surface interaction forces. In a contact mode AFM the cantilever is deflected by the tip-surface interaction forces as it is scanned across the sample surface. The deflection is correlated to the cantilever's location on the sample to generate an image of the surface (28). In either type of AFM measurement, the cantilever resonance frequency or deflection is monitored by a split photodiode. A laser spot is aligned onto the tip of the cantilever, which is then aligned to reflect onto the intersection of a split photodiode. The difference in the photovoltage generated between the photodiode sections can be correlated to the cantilever's position and resonance frequency to generate the image. Figure 1.1 is a schematic drawing of an AFM in operation. The AFM is an extremely powerful microscopy tool that was quickly refined to achieve atomic resolution (29) and more recently has been used to resolve the chemical structure of pentacene (30). AFM's demonstration that a microscale cantilever can be sensitive to such minute forces has inspired researchers to apply micro and nanocantilevers to measure other physical phenomena.

1.1.3 NEMS

Most examples of commercially successful MEMS devices provide an inexpensive, more integrated or more accurate way of performing a task or measuring a signal that can be performed in the macroscale world. AFM is an exception to this observation, as it uses a microscale machine to interface and query nanoscale properties. If one is able to assay the interaction forces between the tip of a microcantilever and individual atoms what other interactions may be observed if the cantilever dimensions are scaled down further? This question has inspired the development of nanoelectromechanical systems.

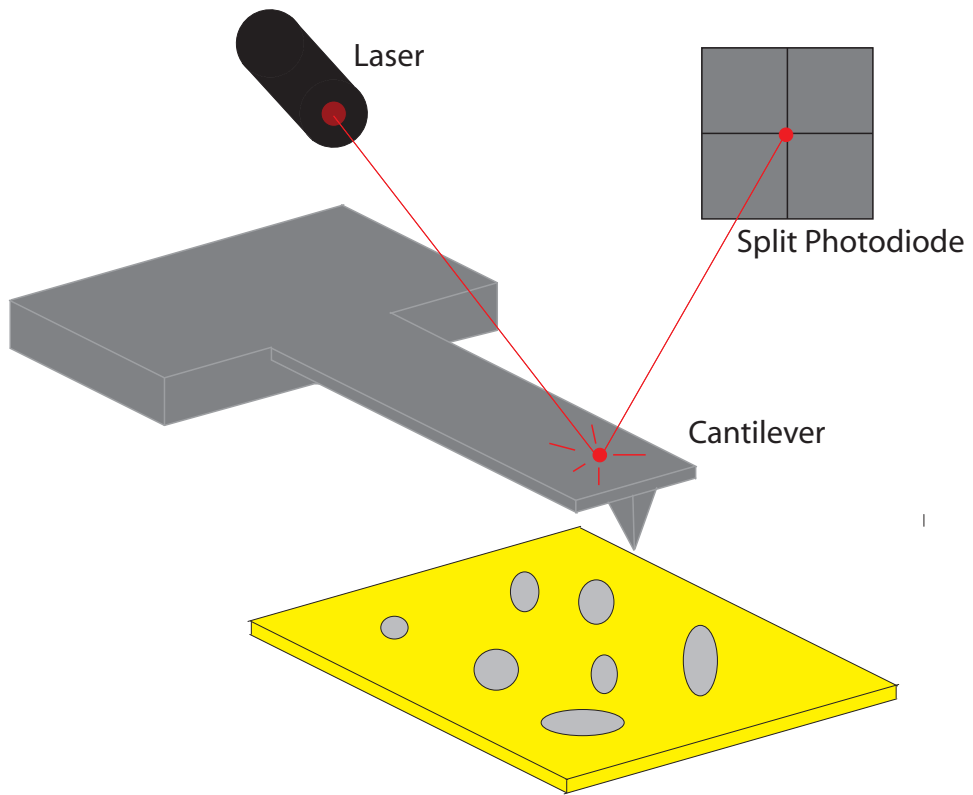


Figure 1.1: Schematic diagram of an Atomic Force Microscope.

In terms of microcantilever gravimetric transducers Ilic *et al.* (31) were able to demonstrate fg/Hz (10^{-15} g) level sensitivities, allowing the detection of single bacteria binding events, as bacteria weigh on the order of hundreds of femtograms. However, if one wanted to probe the inner working of the cell, much more sensitive gravimetric sensors must be pursued. A general relation between the minimum detectable mass of a resonant cantilever transducer and the transducer's mass is as follows.

$$\Delta m_{min} \propto \frac{m_{cant}}{Q} \quad (1.1)$$

where Δm_{min} is the minimum detectable mass, m_{cant} is the cantilever transducer mass, and Q is the quality factor (a measure of spectral purity). Due to the proportionality of the minimum detectable mass and the cantilever mass NEMS devices are needed to assay the elements of life inside the cell wall. The field of NEMS has progressed from bacterial detection to individual virus particle detection (32) (single femtogram level masses) and attogram (10^{-18}) levels of mass sensitivity allowing the detection of binding of many proteins or SAM molecules (33; 34). Most recently Naik *et al.* (35) have demonstrated NEMS mass spectrometers which are able to distinguish between single and multiple (2x, 3x, etc..) binding events of BSA molecules. We can see that NEMS represent an evolutionary offshoot of MEMS devices for the measurement of extremely small physical phenomena, though these sensitivity gains seem to be mainly confined to dynamic mode gravimetric sensors.

1.2 Biological and Chemical Sensors

1.2.1 What is a Sensor

Oxford defines a sensor as “a device which detects or measures a physical property and records, indicates, or otherwise responds to it”. Thus, sensor functionality can be broken up into two components; a recognition element

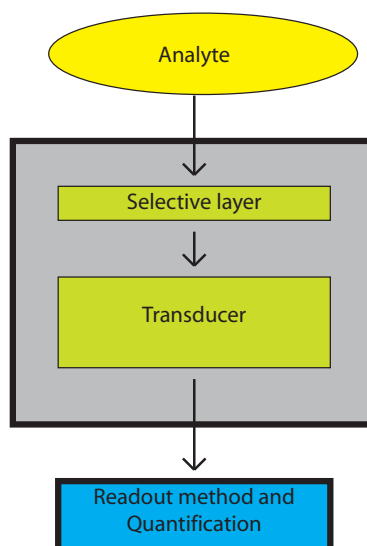


Figure 1.2: Generalized block diagram of a sensor

and a transduction element (36). A generalized block diagram of a sensor is provided in figure 1.2. A supermarket produce scale would be a good sensor example, its recognition element is the basket where the queried weight is placed. The basket is attached to a spring that undergoes displacement due to the added weight. This spring is the transduction element. The spring is in turn attached to a calibrated dial that moves as the spring elongates and indicates the weight of the produce in the basket. This is the readout element. Often a transduction technology can be applied to many different sensing problems (with varying degrees of success) through trivial modifications to its recognition element. This is the case for cantilever sensors and every competing sensor technology that is outlined in this thesis.

In order to get any value out of this discussion of sensors, it is important to take a moment to think about what properties are important in a sensor. Fundamentally we desire a sensor that fulfills the “3S” criteria of being highly sensitive, selective and stable (10). In addition, we can highlight some

secondary desirable properties such as having a fast response to stimuli, providing quantitative information, being rugged and compact, being simple to use and not requiring highly trained operators, and finally being inexpensive. Not all of these secondary properties may be required for a given application, for example compactness may not be necessary for an emissions sensor on a coal fired powerplant but it is certainly important in the emissions system of an automobile.

1.2.2 Motivation for Biosensors

The journal *Biosensors and Bioelectronics* defines a biosensor as “analytical devices incorporating a biological material (e.g. tissue, microorganisms, organelles, cell receptors, enzymes, antibodies, nucleic acids, natural products etc.), a biologically derived material (e.g. recombinant antibodies, engineered proteins, aptamers etc) or a biomimic (e.g. synthetic receptors, biomimetic catalysts, combinatorial ligands, imprinted polymers etc) intimately associated with or integrated within a physicochemical transducer or transducing microsystem, which may be optical, electrochemical, thermometric, piezoelectric, magnetic or micromechanical.”. Basically, a biosensor is a sensor in which the recognition element is made with biological, biologically derived, or biomimetic material. There are a wide array of real-world problems that motivate the development of biosensor platforms; some examples are provided below.

Pathogenic Bacteria

The detection of pathogenic bacteria is of great importance for the protection of food and water supplies all around the world. For example, *Escheria coli* is a common bacteria that lives symbiotically in the digestive tract of many animals. Certain strains such as *E. coli* O157:H7 can cause food poisoning which may be fatal for young, old, or immune compromised individuals. *E. coli* O157:H7 is a common concern in ground beef but has also been spread

through contaminated groundwater (37) and produce (38). The vast increase in scale of production for beef in the past fifty years (from small farms to vast feedlots with tens of thousands of cattle) and the changes in feeding this entails have been identified as a major cause of increased prevalence of Shiga toxin producing *E. coli* in the food supply (39). The incidence of *E. coli* in tested ground beef samples in the United States dropped 43% between 2004 and 2006, much of this was attributed to intensified regulatory programs and testing. Tertiary reservoirs for *E.Coli* are not currently being targeted for testing and consequently, the proportion of *E.Coli* infections from sources like drinking water, milk and leafy vegetables has been increasing in past years. The availability of more rapid and inexpensive tests for bacterial illnesses like *E.Coli* could enable widescale testing of tertiary reservoirs near industrial livestock centres, improving the response of regulatory agencies and lowering the toll on human life.

Disease Biomarkers

Early detection can be a critical factor to the treatment of many diseases such as cancers, where to maximize survivability it is important to detect cancer biomarkers before the cancer has metastasized. Other maladies can also benefit from rapid detection like diabetes where early detection provides the opportunity to introduce lifestyle changes early and mitigate damage caused to the individual. There has been much interest in using three dimensional lateral flow assays for applications such as these (40; 41) so that the advances in cancer and chronic disease screening could be translated to countries with poor health infrastructure. Lateral flow assays are well suited to determine the qualitative presence of biomarkers, which is why they are used in drug and pregnancy tests where one is only interested in the presence or absence of a biomarker above a certain threshold amount. A compact MEMS biosensor would present a similar solution to this problem, without the calibration problems inherent in translating a colour on the lateral flow assay to an actual analyte level.

1.2.3 Motivation for Chemical Sensors

In the past few years, there has been increased interest in technologies to detect explosives as the threat of terrorism has become more prevalent in the west. For environments that are well controlled and can support large and expensive infrastructure (like airports), there exist a number of satisfactory technologies for detecting explosives like ion mobility spectroscopy, mass spectroscopy and gas chromatography (42). As airports have become more secure terrorists have shown some examples (Madrid 2004, London 2005) of attacks on less controllable places such as public transit hubs. In addition to explosive threats, nerve gases have also been used in the past to target public transportation (Tokyo 1995). An ideal solution to these threats would be a compact and portable sensor technology that could be easily carried by transit employees or law enforcement personnel. The possibility of tagless detection of volatile organic compound (VOC) signatures (43) and organophosphates (nerve agents) (44; 45) has already been demonstrated with MEMS cantilever transducers. The refinement of this technology (improvement of preconcentrators and transducer integration) would enable sensors to foil new terrorist attacks in less controllable environments.

Another problem that could benefit from the availability of a portable chemical detection platform is that of groundwater contamination by toxic heavy metals like mercury, cadmium, and lead. Mercury contamination poses a serious health risk because it is non-biodegradable and tends to bioaccumulate. The development of low cost and effective tests for these metals would enable more widespread testing. This would enable early detection which would mitigate environmental damage and lower cleanup costs (46). Another source of groundwater contamination is hexavalent chromium, a known carcinogen. Chromium is the second most prevalent inorganic contaminant at hazardous waste sites. Chromium contamination commonly comes from industrial processes like electroplating and corrosion protection. Hexavalent chromium forms chromate and bichromate which are both highly soluble, while less toxic forms of Cr (like Cr(III)) form insoluble precipitates. The solubility of Cr(VI) leads

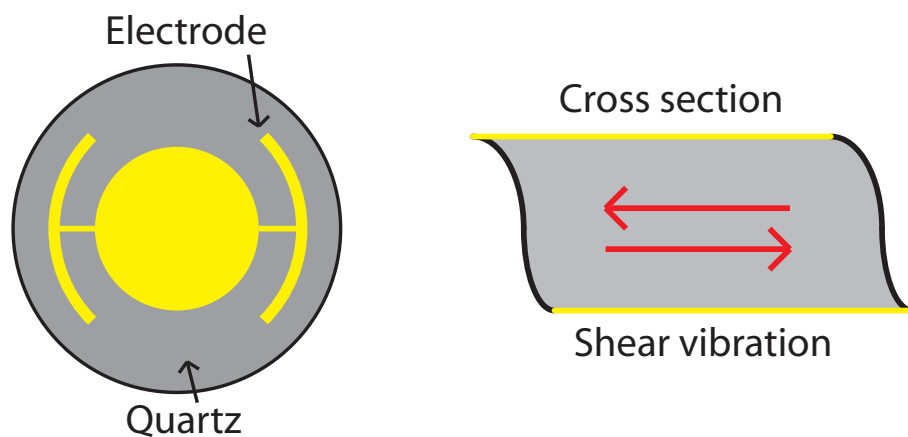


Figure 1.3: Schematic diagram of an Quartz Crystal Microbalance

to high mobility of the contaminant away from the Cr contamination source and into aquifers where it may be consumed in drinking water (47). The ability to inexpensively detect the presence of Cr(VI) would enable prompt water remediation before aquifers are contaminated beyond acceptable levels.

1.2.4 Sensor Technologies for Biological and Chemical Sensors

Quartz Crystal Microbalance

A quartz crystal microbalance (QCM) is a sensor that is fabricated using a quartz crystal and its operational principle is primarily gravimetric. Several review articles have been published in recent years illustrating the fundamentals of QCM operation, its application as a transducing platform (48; 49) as well as putting its strengths and weaknesses in context with other sensing platforms (50; 51). The microbalance device relates the resonant frequency of a cut slab of quartz material to environmental changes at the surface of the quartz chip. This change in frequency takes place when the QCM's acoustic impedance is changed by adsorbed masses or modified damping conditions at

its surface. The fundamental frequency of the disc's resonance is dictated by its dimensions, elastic modulus and density (52). A Y-cut of the quartz crystal is employed to ensure that the disc is resonating in a shear mode, and the thickness of the cut should be a multiple of a half wavelength of the desired resonance frequency.

To apply a QCM as a sensing platform, electrodes are deposited on each side of the quartz disc and the disc is electrically excited to resonance. The QCM disc is functionalized using a suitable probe to bind to a targeted chemical or biological element of interest. It is then exposed to the analyte we wish to interrogate. If the targeted chemical or biological element is present, it will bind to the surface of the QCM thereby adding mass and reducing the resonance frequency. A diagram of a QCM disc is illustrated in figure 1.3. An illustrative, simple and common application of QCMs are to monitor the thickness of a deposited thin film in an evaporation system. The QCM sensor is placed in the vacuum chamber and exposed to the evaporated flux. Knowing the density of the material being evaporated, one can determine the thickness of the film that has been deposited. This technique was first demonstrated by Sauerbrey (53) and his model shows a linear relationship between added mass and QCM frequency. With the development of more accurate models for resonant behaviour, QCMs has been applied to measure a vast array of chemicals or biologically important targets such as humidity, volatile organic compounds, pollutants, gas chromatography, antibodies, polymers and DNA.

Like any chem/bio transduction platform, QCMs have their advantages and drawbacks (54). QCMs are rather inexpensive, they are macroscale and well established in terms of technology and thus an easily accessible transduction technology to develop a chem/bio sensor. Additionally, their electrical readout makes them amenable to sensing applications in opaque solutions or situations where a bulky optical readout system would be impractical. As a drawback, the size of QCMs would inhibit large scale integration and lead to a rather low mass sensitivity (on the order of $\frac{ng}{cm^3}$) compared to similar tagless gravimetric sensors like SAW or cantilever devices. Lastly, QCMs like any tagless chem/bio

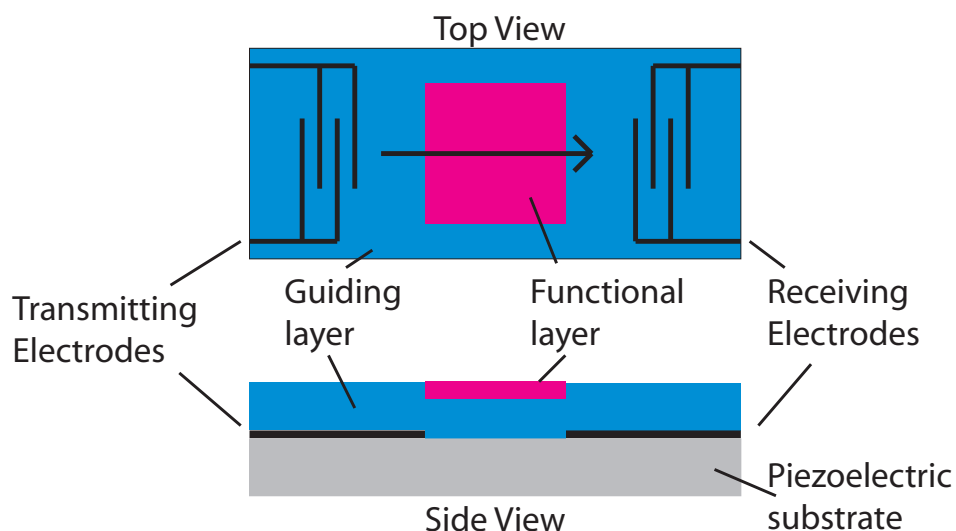


Figure 1.4: Schematic diagram of an Love-wave type Surface Acoustic Wave transducer.

transducer are inherently nonspecific and thus special care must be taken to deconvolve or eliminate signals coming from sources such as viscous damping (if used in a solution), temperature fluctuations or nonspecific binding during the course of measurement.

Surface Acoustic Wave

A surface acoustic wave probe (SAW) is another gravimetric and tagless chem / bio transduction technology. An in depth discussion of the operating principles behind SAW is well illustrated in a review by Wohltjen and Dessy (55), while Lange *et al.* (56) provide a recent overview of SAW biosensor applications. The principle behind a SAW device is to generate an acoustic wave that is constrained to the surface of the device unlike QCM where it permeates through the bulk of the device. To generate this surface wave, interdigitated electrodes are deposited on a piezoelectric substrate such as quartz, lithium niobate, or lithium tantalate. When voltages are correctly applied across these electrodes, the underlying piezoelectric lattice is alternately strained and re-

laxed, creating an acoustic wave that propagates across the surface of the piezoelectric substrate. The frequency of this wave is dictated by the spacing between the fingers of the interdigitated electrode. The acoustic wave generated is very sensitive to changes in the interface between the substrate it propagates along. To create a chemical or biosensor, one must functionalize an area on the substrate between the exciting electrode and the readout electrode where the target analyte will bind and modify the acoustic impedance of the SAW device. A diagram of a SAW transducer is provided in figure 1.4.

Initial work on SAW chemical and biosensors was impeded by the fact that initial “Rayleigh-wave” SAW devices suffered from massive attenuation when immersed in buffer solutions (57; 56). Nonetheless, some preliminary applications were explored in gas chromatography (58) and polymer characterization (59). The development of shear wave modes of operation greatly improved the applicability of SAW to chemical and biosensor applications due to their minimal interaction with surrounding solutions. A further refinement of shear mode SAW was the development of Love wave sensors, whereby the SAW propagates preferentially in a guiding layer between the substrate and the environment. Thoughtful design of this guiding layer (appropriate thickness and choosing a material with low intrinsic attenuation) can achieve an acoustic wave resonance that increases device sensitivity. Additionally, this guiding layer can protect the SAW electrodes from corrosion due to immersion in solution. Love wave sensors have been used to detect antibodies, DNA, bacteria and small molecules such as glucose and urea (56).

Putting SAW sensors into context the point is often made that SAW is not influenced by the bulk of the piezoelectric substrate enabling development of sensors that operate in the 100 MHz to low GHz range, improving sensitivity to small masses. When the practical concerns of deconvolving attenuation from guiding layers and solutions is considered, it becomes clear that SAW devices are not universally more sensitive than QCM as a gravimetric sensor (60). SAW is certainly more appropriate than QCM for large scale integration, since there are several CMOS compatible SAW fabrication processes. SAW is

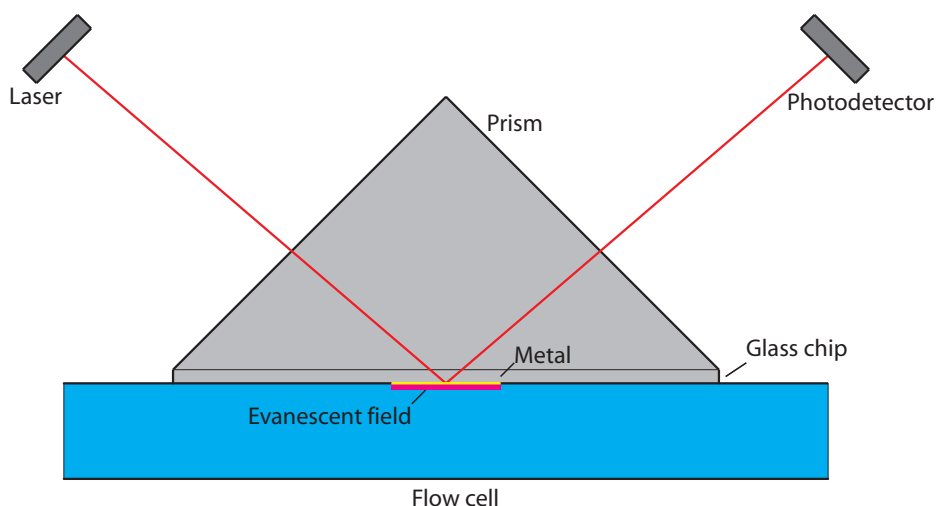


Figure 1.5: Schematic diagram of a prism coupler based SPR sensor

also more suitable than QCM for microfluidic integration since electrodes are easily isolated from solution. Ultimately, SAW devices are of similar though potentially improved sensitivity compared to QCM, better suited to some applications, but still susceptible to many of the same drawbacks as a QCM based chemical and biosensors.

Surface Plasmon Resonance

Surface Plasmon Resonance (SPR) is an optical phenomena that has been used as the basis of a number of tagless chemical and biomolecular sensors in recent years. An SPR sensor works by illuminating a thin metal film (typically ~ 30 nm of Au or Ag) through a prism at a precise wavelength (typically IR or visible) and angle and reading back the reflected intensity with a photodetector. At a certain angle and wavelength, the reflected intensity drops off precipitously as the evanescent wave tunnels through the metal layer and excites a charge density oscillation (surface plasmon wave) along the metal-dielectric interface (61; 62). This electromagnetic field associated with the surface plasmon wave is contained mainly in the dielectric and decays exponentially (like

an evanescent field) with increased distance from the interface. The angle and wavelength at which this reflected minima occur is highly sensitive to changes in the index of refraction within this evanescent field (typically ~ 300 nm in depth). This effect is exploited in applying SPR as a chemical or biosensor. Attachment of the analyte of interest is either quantified by a change in the reflected intensity (for fixed angle and wavelength), change in angle of SPR (for a fixed wavelength), or change in wavelength of SPR (for a fixed angle). Similarly to other tagless chemical or biotransduction technologies one must take care to be able to distinguish between SPR change due to attachment of the desired analyte and SPR change due to nonspecific binding. A schematic of a prism coupler based SPR system is provided in figure 1.5.

The fact that SPR is an optical technique rather than gravimetric (SAW and QCM), it is meaningless to make a comparison in terms of sensitivity to an attached mass. There have been some case specific comparisons of biomarker sensitivity between SPR and gravimetric technologies. Kosslinger *et al.* (51) fabricated an SPR-QCM flow cell for a direct comparison of the two technologies applied to detect the presence of HIV-antibodies in rabbit sera, and monoclonal antibodies to bovine serum albumin. In both cases, the detection limits were very similar.

SPR provides some contrasting advantages and disadvantages to other tagless biosensors like SAW and QCM which does make it an attractive platform for some applications. Firstly, since the principle of operation is optical, SPR is very attractive for assaying solutions, as there is no loss in sensitivity due to viscous damping. SPR is therefore quite amenable to integration into flow cells in order to achieve real time detection. Also, since SPR commonly leverages Au as the metal layer, SPR systems are intrinsically enabled to use the vast array of thiolized molecules that are commercially available to functionalize a surface for biosensing. The main drawback of the SPR approach is that the optical system for excitation and readout is rather large and bulky. Additionally, the probing range is limited to approximately 300 nm from the interface which enables the detection of small biomolecules, but bacteria are so large that the

evanescent wave will not fully encompass them, hurting sensing efficiency.

Waveguide Sensors

Another tagless optical sensor transduction platform would be a waveguide sensor (63). Waveguides are structures that transmit electromagnetic signals with very low loss. Electromagnetic loss is prevented by transmitting the EM wave in a guiding material (typically called the core) which is surrounded by another material (typically called the cladding) and choosing indices of refraction for these materials that would prevent transmission of the EM wave across the interface between them. Conventional optical and infrared waveguides accomplish this task by employing a high refractive (glass, silicon) index material as the core and surrounding it with a lower index material. This configuration creates a total internal reflection condition, confining the electromagnetic radiation in the core (except the evanescent wave). Another type of waveguide is a photonic crystal waveguide (64) which works by introducing an ordered defect lattice into the material to induce a photonic bandgap in regions of the material where we wish to forbid photon presence.

To apply a waveguide as a transducer for a chemical or biosensor the cladding is removed in a small region of the waveguide and this portion is immersed in a solution containing the target analyte. The evanescent wave in this portion of the waveguide is thus exposed to the solution we are querying and binding of the target analyte can be detected by numerous methods including absorption, fluorescence, Raman scattering, surface plasmon resonance, or mode cutoff by modification of refractive index (65; 66). It is important to note that a waveguide structure is really more of a technology for integrating and reducing the scale of an optical sensor and is not specific to any physical phenomena we are exploiting. Some examples of successful application of tagless waveguide sensors include the Corning Epic system which uses a resonant waveguide grating (integrated into microplates) to monitor the change in refractive index due to cell activity in the microplates (67). Recently some nanophotonics researchers have applied photonic crystal waveguides to biosensing problems. Jensen *et*

al. (68) detected fluorophore labelled antibodies with a photonic crystal fibre while Rinsdorf *et al.* (69) detected DNA by a change in resonance frequency of a grating inscribed in the photonic crystal fibre. Buswell *et al.* (70) have also demonstrated detection of streptavidin binding to a biotin functionalized planar waveguide by monitoring the change in mode cutoff wavelength.

Ultimately, waveguides provide a tool to integrate many of the elements of an optical sensor technology like SPR so that we can assay a solution for many different targets in parallel. The advantages and disadvantages of this technology as a sensor transducer is in line with those noted for SPR. Waveguide sensors are amenable to use in fluids since there is no loss due to damping and they have the potential for many more parallel assays than a traditional SPR system (71). The main drawback to waveguide transducers is the inability to detect any analyte beyond a few hundred nanometres from the core.

1.3 Micro/Nanocantilever Background

A cantilever is a single beam of material, rigidly supported at one end. The application of cantilevers as a transduction technology for biological and chemical structures has largely followed from studies of the AFM, a scanning probe microscopy technique outlined earlier in this chapter. Though much of the recent interest in micro and nanocantilevers stems from the development of AFM, it is important to note that there have been notable macrocantilever sensor demonstrations before the advent of AFM.

1.3.1 Why Micro/Nanocantilevers?

The question of why a micro or nanocantilever is an attractive transducer platform goes back to why any mechanical structure would make a good transduction platform. A resonant cantilever is an acoustic sensor like QCM or SAW sensors, it can be used to determine the presence or absence of a bound analyte

by the change in its resonance characteristics. There are four response parameters that can be measured (72), the resonance frequency, resonance quality, resonance amplitude and cantilever deflection. Changes in these properties are caused by changes in mass, surface stress and damping environment.

One advantage that cantilever sensors have over QCM or SAW devices is that there are a litany of optical and electrical readout methods at the designer's disposal (73) so limitations of readout do not generally limit the application of cantilever devices to a limited few transduction tasks. Another huge advantage that cantilever sensors have is that they can be machined to very thin dimensions, so that the ratio of analyte mass to transducer mass to be much higher than QCM or SAW devices, allowing much greater sensitivity. Thundat *et al.* (72) used AFM cantilever sensors as transducers and compared their sensitivity to QCM and SAW device sensitivities tabulated by Ward and Buttry (74), showing the increased potential of cantilever sensors. Indeed the readily available AFM cantilevers, which had not been optimized for mass transduction, were already ten times more sensitive per unit area than the most sophisticated SAW devices of the time.

Unlike QCM and SAW, cantilever transducers can also be used in static mode, measuring the stress imparted by analyte adsorption events. The interaction of analytes with the surface of a cantilever may modify the cantilever's temperature or surface free energy inducing a stress which causes cantilever bending. This mode of operation is not susceptible to viscous damping from the environment (like resonant cantilevers, QCM and SAW) and is ideal as a transduction method in aqueous environments.

Cantilever sensors, while much more sensitive than QCM or SAW, nonetheless have their drawbacks. The three dimensional nature of a microfabricated cantilever means that it is much more susceptible (than QCM and SAW) to breakage if there is any incidence of mishandling. Additionally, like QCM and SAW but unlike SPR and waveguides, microcantilevers are prone to viscous damping if used in liquids or air, compromising their ultimate sensitivity. Being a tagless sensing technology, it is imperative that the sensor designer

isolates sources of noise like changes in temperature, viscous environment, or surface stress so that the cantilever's change in frequency can accurately be correlated to increased analyte mass.

1.3.2 Previous Work in Micro/Nanocantilever Chemical Sensors

Barnes *et al.* (in 1994) (75; 76) provided one of the first reports of microcantilever transducers being applied as chemical sensors by demonstrating femtojoule level calorimetry with a static microcantilever. That same year Gimzewski *et al.* (77) used a Pt coated AFM cantilever to monitor the catalytic conversion of H_2 and O_2 to H_2O by monitoring its static deflection caused by heat of the catalytic reaction causing a bimorph (or bimetallic strip) effect. Thundat *et al.* (78) published another early example of a microcantilever chemical sensor when they demonstrated the sensing of relative humidity by change in resonance frequency. The humidity sensors utilized two different humidity sensitive coatings (phosphoric acid and bovine skin gelatin) and it was shown that two different mechanisms could affect the resonance frequency of the cantilevers. In the case of the phosphoric acid coating, adsorbed water caused the resonance frequency of the cantilevers to drop due to mass loading. In the case of the gelatin coating, adsorbed water caused the gelatin to swell and increase the cantilever's resonance frequency. Concurrently, Chen *et al.* (79) reported on the same humidity experiment and used deflection data taken simultaneously to decouple the effects of stress and mass loading on the cantilever.

Alkanethiols are a class of organic molecules with a sulfur atom at one end that form well ordered monolayers on gold surfaces (80; 81). The incredible stress sensitivity of static cantilever sensors has led to their application to study the mechanics of alkanethiol adsorption and assembly. Berger *et al.* (82) initially used an AFM type setup to detect the surface stress induced by the assembly of different chain length alkanethiols, and reported that longer alkanethiol

chain lengths indeed induce a different surface stress. Godin *et al.* used a similar setup, but with a simultaneous reference experiment and ellipsometry to monitor SAM thickness. They showed that the ordered assembly of the SAM and the induced surface stress was dependant on large Au grain sizes (83) and that when large grain size Au was employed as a cantilever coating, there was no appreciable difference in surface stress induced by alkanethiol SAM (84). Desikan *et al.* (85) used a piezoresistive readout technique for their static cantilever assaying of alkanethiol SAMs and did confirm the results of Berger *et al.* by finding discernable surface stress variation between longer and shorter alkanethiol SAMs. It must be noted that the surface stresses observed by Berger *et al.* and Desikan *et al.* were much smaller than those observed by Godin *et al.* and consensus on the mechanics of alkanethiol stress has not been reached.

More practical applications of micro and nanocantilevers as chemical transducers have been published in the form of hydrogen sensors. Hydrogen has been increasingly researched in the past few years as a chemical method to store energy for conversion in fuel cells. Unfortunately, practical solutions to hydrogen storage have been elusive. If breakthroughs are made in hydrogen storage, the ability to detect hydrogen concentrations and hydrogen leaks will be of great importance. With such foresight, some researchers have looked to cantilever transducers as a potential solution. Lang *et al.* (43) demonstrated the sensing of Hydrogen by adsorption onto Pt coated static microcantilever transducers at a flow rate of $1 \text{ mbar} \frac{l}{s}$ in air. Thundat *et al.* (86) developed a dynamic mode hydrogen sensor utilizing AFM cantilevers coated with PtO_2 . The reduction of PtO_2 on the cantilever's surface lead to a loss of mass which was detectable in hydrogen concentrations as low as 4% in an argon carrier gas. A drastically different approach for hydrogen sensing was taken by Huang *et al.* (87) who fabricated Au-Pd alloy nanowire resonators that were under tension. The resonators were actuated under vacuum and upon exposure to hydrogen at 10^{-5} torr, the resonance frequency of the nanowires decreased drastically. This resonance frequency decrease was attributed to a relief in the stress of the nanowire cause by its swelling as hydrogen atoms began occupying

interstitial sites in the alloy.

The detection of explosives and volatile organic compounds (VOCs) has also been demonstrated using microcantilever transducers. One of the telltale signs of a homemade explosive device is the presence of VOCs such as acetone. Lang *et al.* (43) demonstrated static and dynamic cantilever transducer based detection of a series of different alcohols with PMMA coated Si cantilevers. Then *et al.* (88) further expanded on this idea by employing an array of different types of polymer coatings on their resonant cantilever sensors and were able to discriminate between various VOC “signatures”. Both Lang *et al.* and Then *et al.* exploited the swelling of polymers to generate their signal. Pinnaduwaage *et al.* (89) detected more sophisticated explosives like TNT and PETN on AFM cantilevers through both static cantilever bending and by monitoring resonance frequency as temperature was pulsed to cause deflagration of the explosive compounds.

1.3.3 Previous Work in Micro/Nanocantilever Biological Sensors

Cantilever Bacteria Sensors

One of the earliest reports applying cantilever transducers to bacterial sensing is that of Ilic *et al.* (90) who used a resonant cantilever to detect the binding of *E. coli* O157:H7. Silicon nitride cantilevers were functionalized with antibodies to *E. coli* O157:H7 and then their resonance response was monitored in a split photodiode setup. The cantilevers were then exposed to a bacterial solution and dried before the resonance frequency was assayed again. In the case of exposure to *E. coli* O157:H7 the resonance frequency underwent significant shift, while exposure to *Salmonella* bacteria caused no shift. Ilic *et al.* further refined this method to demonstrate single bacteria detection (31). This method of liquid exposure followed by drying and measurement is colloquially known as a “dip and dry” measurement and is typical of these early bacte-

rial sensors. Similar “dip and dry” measurement based bacterial sensing was performed by Gupta *et al.* (91) who detected the presence of *Listeria innocua* with single crystal silicon cantilevers using a split photodiode readout method. Unfortunately, the cantilever dimensions in this case made them susceptible to stiction and all solution exposure steps were followed by a time consuming critical point dry step.

The “dip and dry” method is nonideal for biosensing applications since many biomolecules like proteins and antibodies may be damaged by drying, and the sensing cannot take place in real time. Investigators have looked into overcoming the limitations of a “dip and dry” method by designing cantilever sensors more suitable for use in solution. Campbell and Mutharasan (92) used PZT film connected to a glass cantilever to detect different concentrations of *E. coli* in solution, demonstrating strain specificity with a lower limit of detection of 700 bacteria / mL. A much more interesting bacterial detection solution was published recently by Burg *et al.* (93) where microcantilevers were fabricated with built-in microchannels. The microchannel cantilevers (generally referred to as suspended microchannel resonators or SMRs) were fabricated using SOI wafers and vacuum packaged so that no external vacuum pump would be required to mitigate viscous damping effects. The cantilevers had a high Q factor which showed no observable degradation upon filling the microchannel cantilever with PBS solution. The cantilevers were able to detect the presence of different individual bacterial cells (*E.Coli* and *B.subtilis*) due to their different sizes and densities relative to the PBS carrier solution. Arlett and Roukes (94) provided a theoretical review of these suspended microchannel resonators and showed that in a “flow through” regime, devices should be easily capable of measuring single virus particles and small numbers of proteins. This analysis also showed that in an affinity capture mode of operation the SMRs should be capable of building up a detectable mass of proteins or antibodies much more quickly than the conventional biodetection method ELISA (enzyme-linked immunosorbent assay).

Cantilever Virus Sensors

The detection of virus particles is a greater challenge than bacteria due to their small mass compared to bacterial cells (10^{-13} g for bacteria vs 10^{-15} g for viruses). Gupta *et al.* (95) demonstrated nonspecific “dip and dry” detection of single *vaccinia* virus molecules on microcantilevers with laser doppler vibrometry. Shortly thereafter, Ilic *et al.* (32) demonstrated specific detection of *baculovirus* using an antibody functionalized polysilicon nanocantilever resonated in vacuum.

Other Cantilever Biosensors

Cantilever sensors have also been applied to detect the presence of many biologically derived molecules like nucleic acids, proteins, vitamins, and antigens. For the sake of brevity, only a few papers will be summarized here. One of the more common detection targets is the biotin-streptavidin binding complex. Biotin is a vitamin that binds selectively to the streptavidin protein and there are a number of commercially available products to immobilize either biotin or streptavidin on a surface in order to detect its complement. Fischer *et al.* (33) provide one such cantilever biosensor example by detecting the binding of streptavidin on biotin derivitized SiCN resonator beams.

Some static microcantilever biosensors have garnered even more attention in literature. Hansen *et al.* (96) were able to demonstrate detection of DNA molecules. Thiolized ssDNA was immobilized on a static AFM cantilever and solutions containing complementary and slightly mismatched ssDNA strands was flowed through a liquid cell. This technique was able to discriminate between single base pair mismatches. Wu *et al.* (97) used a similar transducer setup to detect the presence of prostate specific antigen (PSA, the typical prostate cancer biomarker) in human serum albumin and human plasminogen at identical levels to ELISA techniques that are currently used. This advancement shows that static cantilever transducer technology could drastically reduce time and cost of PSA and other disease biomarker tests. Lastly, an

emerging problem in public health is the emergence of antibiotic resistant bacteria like methicillin-resistant and vancomycin-resistant *Staphylococcus aureus* (MRSA and VRSA). Ndieyira *et al.* (98) demonstrated the ability to probe the effectiveness of antibiotics (at clinical concentration levels) on simulated VRSA and non-VRSA bacterial cell walls using static microcantilevers. This advancement could further illuminate the mechanisms of interaction between antibiotic and cell wall and improve the speed of drug development.

1.4 Rationale and Thesis Outline

This project is an exploration of the fabrication of micro and nanocantilever sensors in alternative materials. Specifically we explore the application of metal nanocomposites as materials to improve the sensitivity of static cantilever sensors, and the application of atomic layer deposition (ALD) synthesized materials to improve the sensitivity of resonant cantilever sensors.

1.4.1 Metal Nanocomposites

Metal nanocomposites are metal alloys with multiple distinct phases. It has been shown that through alloying techniques like rapid quenching, ion mixing or co-sputtering, one can fabricate alloys that are not at thermodynamic equilibrium. When these principles are applied to FCC-BCC metal alloys with numerous complex intermetallic phases, the formation of metallic glasses has been observed. These principles have been applied to alloy systems like Al-Mo (99; 100), Ni-Mo (101), and Cu-Hf (102) in order to tailor the microstructure of metal films so that they may be applied to MEMS and NEMS devices.

Traditionally, micro and nanocantilever transducers have been fabricated out of materials like single crystal Si, Polysilicon and Si_3N_4 since they are stiff and light materials. Additionally, these are the materials commonly used in IC fabrication so there is a wealth of fabrication technologies available for them.

Metals have largely been overlooked for dynamic cantilever transducers due to their low elastic modulus, high density, polycrystalline nature, and large intrinsic sources of mechanical loss. While co-sputter alloy development has ameliorated some of these characteristics, it is unlikely that such microstructural refinement will be able to overcome these inherent material limitations. However, the figures of merit for the sensitivity of a static cantilever transducer are much more strongly affected by the dimensions of the cantilever than its microstructure, mass or elastic stiffness. The development of a metal nanocomposite material presents an elegant solution to achieve excellent sensitivity in static microcantilevers because it enables fabrication of ultrathin static cantilevers which are inherently less susceptible to brittle failure.

As explained earlier in this chapter, the function of a sensor can be broken up into two parts, the recognition element and the transduction element. Typically, to sensitize a micro or nanocantilever to the desired analyte entails coating the device with a recognition element like a self-assembled monolayer (SAM), a polymer or a metal. In the case of a dynamic cantilever sensor, this recognition element typically degrades the fidelity of the sensor. In the case of a static cantilever transducer, the designer must ensure that only one side of the cantilever transducer is coated, so that adsorbed analytes will induce a differential stress. Additionally, we typically do not desire the functionalizing layer to have a dissimilar thermal coefficient of expansion from the cantilever's mechanical layer, so that temperature noise is not confused with signal from analyte adsorption. In all these cases, it would be advantageous to design a cantilever that is intrinsically sensitive to our analyte of choice. Many investigators employ gold as an intermediate layer on their cantilever transducers so as to take advantage of the wide array of commercially available thiolized molecules that could be used as a recognition element. In this study, we apply co-sputtering principles to explore the fabrication of ultrasensitive static cantilever sensors using the Au-Ta alloy system. The development of an Au-Ta alloy presents the possibility of cantilever transducers that are sensitive to thiolized molecules requiring less complicated surface modification before being employed as a chemical or biosensor. In this case, the transduction and

recognition elements of the cantilever sensor are one.

1.4.2 ALD synthesized materials

Early nanocantilever and nanobeam structures were fabricated out of silicon on insulator substrates due to their availability, ease of machining, and good mechanical characteristics. Single crystal silicon is a rather brittle material, on the microscale it tends to fail before it deforms plastically (22). Saif *et al.* citeSaif:1998p1629,Saif:1996p1611 have shown that at the microscale the yield and tensile strength of single crystal Si were improved with decreased device dimensions. Increased fracture strength has also been observed in Si nanowires grown by Vapor-Liquid-Solid (VLS) synthesis techniques (105). However this trend of improved yield strength been observed to break down in surface machined nanocantilevers. There have been reports of limited yield in single crystal Si nanobeams (below 50 - 60 nm) being machined by reactive ion etching (106; 107). The lack of examples of single crystal Si nanobeams surpassing the dimensions reported by Carr *et al.* (108) provides further evidence of these yield issues. The cause of these yield problems has been attributed to lattice damage from the reactive ion etching step. RIE induced lattice damage would not be a problem in VLS grown nanowires and would only affect a minute fraction of the volume of microscale beams. Since VLS techniques are difficult to harness, most of the literature regarding NEMS cantilevers still relies on surface machining methodologies. To further pursue surface machined NEMS cantilevers, investigators have migrated away from single crystal Si and towards glassy materials like Si_3N_4 (109) and SiCN (110) fabricated by CVD processes. The motion of dislocations in these materials is impeded by their lack of grain structure, impeding plastic deformation and improving yield.

Developments in low voltage electron beam lithography are enabling the patterning of sub- 10 nm lines (111). Conventional chemical vapour deposition (CVD) synthesis of these glassy materials has not been able to keep pace at reducing film thicknesses. ALD is a CVD method whereby films are grown by

adsorption and reaction of one monolayer of precursor chemicals. ALD has been used to synthesize thin conformal films of many materials like TiO_2 , SiO_2 , Al_2O_3 and TiN (112). ALD is inherently self limited and a suitable candidate for the formation of glassy or nanocrystalline materials at thicknesses that can enable the machining of sub- 10 nm cantilever beams. The application of ALD materials like TiN for resonant cantilever transducers would enable great scaling down in device dimensions, and thus entail the unprecedented mass sensitivity.

1.4.3 Outline

This thesis is organized into seven chapters. Chapter two is a summary of fabrication methods applied to MEMS and NEMS devices, the theory behind resonant and static cantilever transducers, and a summary of various cantilever transducer readout techniques. Chapter three is an overview of silicon nanocantilever work that was performed to develop an electron beam lithography recipe that is amenable to lift-off patterning of metal alloys and was also used to test our resonant cantilever readout interferometer. The electron beam lithography and readout interferometer were directly applied to subsequent work in both nanocomposite metal cantilevers and ALD TiN cantilevers. Chapter four reports on the development of the Au-Ta material, its microstructure, physical characteristics, and work on machining nanocantilever structures to assess the alloy's mechanical characteristics. Chapter five is a summary of the surface chemistry of the Au-Ta material and the development of ultrasensitive static cantilever sensors using a dry etch method. Chapter six is work that was pursued to develop nanoresonator beams out of ALD TiN, including characterizing the film's deposition rate, chemical structure, crystal structure, and developing tools to machine the TiN into beam structures with electron beam lithography and reactive ion etching.

CHAPTER 2

Fabrication Methodologies for Cantilever Sensors, the Theory Behind Their Applications, and Methods for Transduction

2.1 Introduction

This chapter outlines the general principles involved in the use of cantilevers as a transduction platform. These principles have been broken up into three main components, fabrication, theory and readout. In the fabrication sections, fabrication methodologies, specific techniques and pitfalls are highlighted for MEMS and NEMS cantilever devices. In the theoretical summary, the theories behind the operation of a cantilever sensor in static or dynamic modes (such as the Euler-Bernoulli PDE or Stoney's equation) are highlighted and explained. Limitations of these models and the pitfalls associated with these transduction methods are also discussed. Lastly, in the readout section, a brief review of various methods used to measure signals generated by various cantilevers are explained.

2.2 Fabrication Methodologies

The suite of tools that are used to fabricate MEMS and NEMS devices are largely due to the amazing progress brought forth by the development of silicon integrated-circuits over the past 50 years. Researchers realized that the tools that were being used to pattern silicon and metals could also be used to pattern the same materials to make mechanical devices at dimensions that were unaccessible using conventional machining. Consequently, MEMS and NEMS design concepts follow the same paradigm as silicon ICs whereby structures are defined by repeated cycles of planar deposition, patterning and etching (113; 114). In the deposition step, a thin film is deposited on a silicon or glass substrate by physical vapour deposition (sputtering, evaporation, molecular beam epitaxy), chemical vapour deposition (low pressure, plasma enhanced or traditional CVD) or other methods (spin-on, electrodeposition, anodic bonding or fusion bonding). The thin film is then patterned by a masked (optical lithography, stepper) or maskless (electron beam lithography, focused ion beam) lithography technique. Finally, the lithography pattern is transferred to the film or substrate layer by employing a wet chemical etching (KOH, EDP, metal etchants, TMAH) or dry etching (reactive ion etching, XeF_2) technique.

2.2.1 Bulk Machining

Bulk machining typically refers to a machining methodology where the substrate forms the desired mechanical structure, or at least a major part of it. In this case, it is usually necessary to remove vast quantities of substrate material in the etching step to define such a structure. It is common to employ anisotropic etching techniques to remove such quantities of material while protecting the desired machine structure. Anisotropic etching techniques generally fall into the following two categories, wet and dry.

Wet Anisotropic Etching

In wet anisotropic etching a solution of potassium hydroxide (KOH) or tetramethyl hydroxide (TMAH) is employed to etch single crystal silicon. Both KOH and TMAH etch silicon rapidly in the $\langle 100 \rangle$ and $\langle 110 \rangle$ directions but slowly in the $\langle 111 \rangle$ direction. Etch ratios between the $\langle 100 \rangle$ and the $\langle 111 \rangle$ direction can be up to 400:1 (115; 116) given proper temperature and solution preparation. Additionally, these anisotropic wet etchants are highly selective to important structural materials for MEMS like highly doped silicon or silicon nitride, which enables easy integration of an etch stop layer in this fabrication scheme. There are a number of caveats to the application of these wet anisotropic etches; first, their etch rates and selectivities are very strongly dependant on solution temperature and concentration. Secondly, these etches generate hydrogen bubbles in solution that tend to impede flow of etchant to localized areas on the substrate where they build up. For that reason it is common to employ an additive (117) like isopropyl alcohol to help hydrogen bubbles desorb. Lastly, convex corners tend to etch in an accelerated and unstable manner due to the exposure of higher order planes (which etch quickly) to the etchant. For that reason compensation structures should be employed to attain accurate convex corners (118). A sample process flow for a bulk machined cantilever using an implanted etch stop layer is provided in figure 2.1.

Dry Etching

There are a number of methods such as chlorine or fluorine based reactive ion etches or XeF_2 vapour to etch bulk amounts of silicon without using a wet process. XeF_2 etching is a non-plasma isotropic dry etch whereby XeF_2 crystals sublime as they are exposed to a vacuum. When a XeF_2 molecule comes into contact with a silicon surface, the molecule adsorbes and the fluorine dissociates, allowing it to react with the silicon to form SiF_4 gas. This etch is fast and tends to leave the surface in a granular and rough state (115). The main

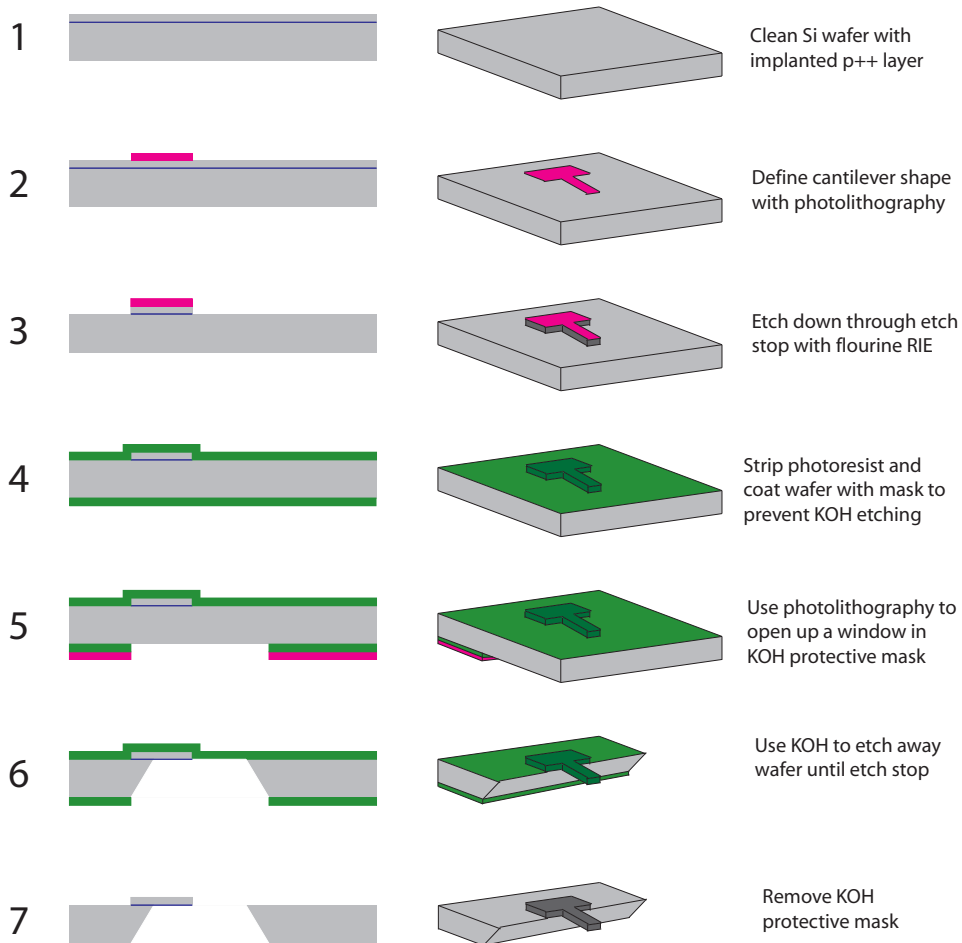


Figure 2.1: Process flow for fabricating a bulk machined cantilever. Step 1: start with a Clean Si wafer with implanted p⁺⁺ layer. Step 2: Use photolithography to define the cantilever shape. Step 3: Etch down through the etch stop layer using a fluorine RIE. Step 4: Protect top and bottom with a mask to prevent KOH etching (Protek, SiO₂, Si₃N₄). Step 5: Use lithography to open up a window on the backside for KOH etch. Step 6: Perform KOH etch. Step 7: Remove protective mask layer.

advantage of XeF_2 is that it is a dry etch that aggressively attacks silicon while leaving aluminium, SiO_2 , Si_3N_4 , and photoresist polymers largely untouched. This is a very advantageous property for integrating MEMS structures into existing CMOS chips or for machining MEMS out of aluminium (99; 100) or alumina (Al_2O_3).

Chlorine and fluorine based reactive ion etches are vast categories of etching methods themselves. Before etching takes place, the substrate to be etched is placed on an RF powered chuck and the etchants are introduced in the form of a gas. The gas is then dissociated by a plasma generated in the chamber by the potential between the powered chuck and the walls of the chamber producing electrons, ions and radicals. Etching of the substrate is accomplished primarily by the radical species diffusing to the substrate and consuming it chemically. Additionally there is some physical etching by ion species being accelerated into the substrate, ejecting atoms by a sputtering method. Etching by the radicals tends towards an isotropic profile, it etches in all directions at the same rate and is thus of limited use for bulk machining methodologies. There are techniques to modify reactive ion etches to achieve high aspect ratios. Bosch etching achieves high aspect ratio etches by alternating short bursts of a standard isotropic fluorine etch with short bursts of a fluorocarbon passivation deposition step. The fluorocarbon passivation layer deposits evenly over the topography but requires ion bombardment to be etched away in the subsequent fluorine etch step. Therefore, passivation material is removed from the bottom of an etched trench before the sides of the trench walls. The combination of these steps results in a quasi-anisotropic etch that makes RIE much more suitable for bulk machining. Bosch etching and etching methods that generate fluorocarbon passivation (like Black Silicon (119) or Cryogenic etching (120)) enable deep etches with high aspect ratios that make RIE techniques more attractive for bulk machining applications.

2.2.2 Surface Machining

Surface machining typically refers to a machining methodology where a thin film is deposited on top of a bulk “handle” substrate and is machined to create the desired structure. Typical materials for surface machined structures include single crystal or polycrystalline silicon, silicon nitride, metals or polymers. Typically single crystal silicon wafers are used as a handle layer for surface machined structures due to their low cost, flat and smooth surface and ubiquity in MEMS and microelectronics industries.

Superficially it seems that surface machining is a very flexible methodology for designing MEMS structures; however, fabricating devices out of thin films does come with its own limitations. Firstly, to obtain movable structures, one must employ a layer of material (called a sacrificial layer) that can be etched without the mechanical layer being degraded. Finding a sacrificial layer that is compatible with the device layer is a first limitation of the surface machining approach. SiO_2 is a common sacrificial layer, since hydrofluoric acid based etchants will attack it over Si and Si_3N_4 with a high degree of selectivity. Secondly, the sacrificial layer must be removed in the process of machining, using wet etchants is the most common way to do this but etchant removal and drying can create the problem of stiction.

Stiction is a portmanteau of the term “static friction” and describes a situation where we have a liquid between a freed structure like a cantilever beam and the substrate below. As the liquid is dried, capillary forces between the liquid and the freed structure pull the structure down until it comes into contact with the substrate. Once in contact with the substrate the structure remains bonded by a force which has been attributed to hydrogen bonding, Van der Waals forces or electrostatic forces (119; 121). The attractive force of drying that allows structures to stick is proportional to the surface tension of the liquid and inversely proportional to the device / substrate gap. To prevent this, one can use a dry etch for sacrificial layer removal or replace the etchant with a solvent with low surface tension like pentane or liquid CO_2 in the case

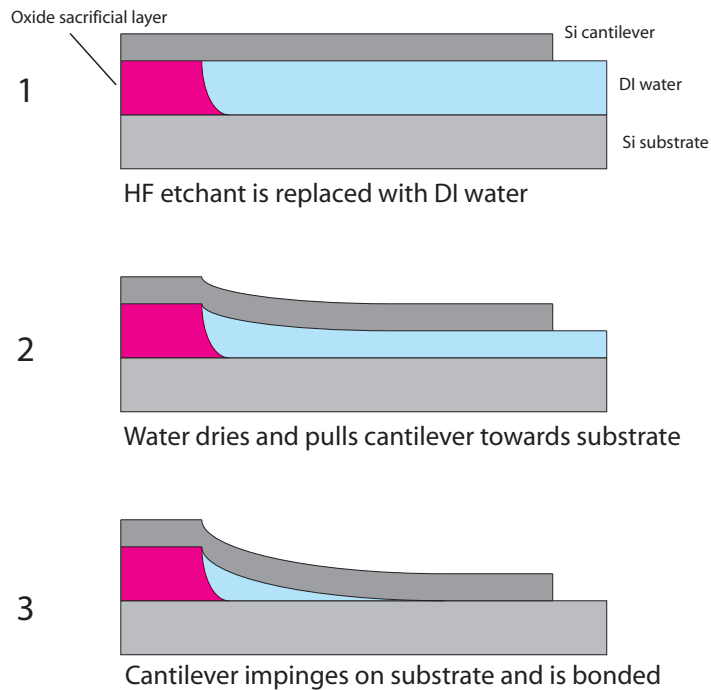


Figure 2.2: The process of a cantilever undergoing stiction. First, the cantilever is immersed in deionized water. Second, the cantilever is being pulled towards the substrate by capillary force. Lastly, the cantilever comes into contact with the substrate and is bonded by Van der Waals forces.

of supercritical drying. Alternatively one can design structures with very high spring constant or with a very thick sacrificial layer so that the capillary force is not enough to pull released structures down to the substrate. A third solution could be to incorporate dimpled structures to minimize the surface area that is in contact with the substrate so that the weak bonding may be overcome by the restoring force of the structure. A diagram of a cantilever beam being pulled down by capillary forces, leading to stiction, is provided in figure 2.2.

Since they involve such short etch times surface machining methodologies are generally more flexible than bulk machining methodologies in terms of materials. There are few materials which may stand up to sustained attack by

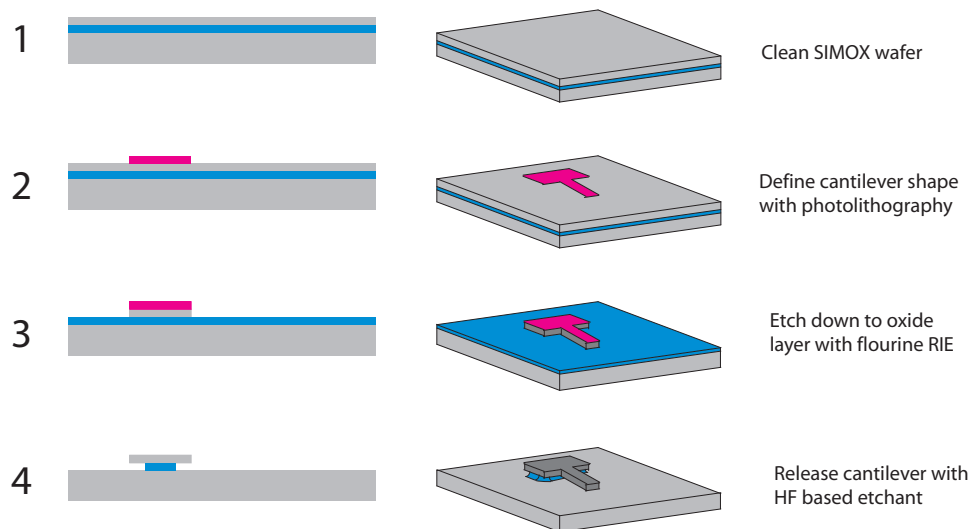


Figure 2.3: Process flow for fabricating a surface machined cantilever. Step 1: Start with a clean SIMOX wafer. Step 2: Define a cantilever shape with photolithography. Step 3: Etch down to buried oxide with a fluorine RIE. Step 4: Release the cantilever by etching away the buried oxide below it with an HF based etchant. (critical process drying may be required depending on device dimensions)

common bulk machining etchants such as KOH or TMAH. A typical surface machining process flow for a cantilever using a silicon on insulator (SOI) wafer is provided in figure 2.3. SOI wafers consist of a top “device” layer of silicon, a buried SiO₂ layer (sometimes called buried oxide or BOx) and a bottom “handle” layer for the wafer’s mechanical integrity.

2.3 Dynamic Versus Static Cantilever Operation

Cantilever sensors are generally categorized by their transduction mode; the two main transduction modes are termed “static” and “dynamic”. In a static mode, stress imparted by adsorption of the analyte of interest on the cantilever

surface causes deflection, which is quantified and translated into the analyte's presence. In the dynamic mode of operation, a cantilever is driven to resonance, when there is a binding event the added mass causes the cantilever's resonance frequency to change, which is correlated to the analyte's presence. The next couple sections will outline the theory, strengths and weaknesses of both cantilever transduction modes.

2.4 Dynamic Mode

As previously stated, when a cantilever sensor is operated in dynamic mode it is driven to resonance. The attachment of an analyte molecule will add a small amount of mass to the cantilever lowering its resonance frequency. Conceptually, this mode of operation is like QCM or SAW sensors in that it is gravimetric. This section will outline some theories describing the vibration of a cantilever beam, sources of noise and dissipation for resonant cantilevers, and the mass sensitivity of dynamic cantilever transducers.

2.4.1 Spring Constant

The simplest model that can be applied to describe a resonating cantilever is that of an undamped spring-mass system. The resonant frequency of a linear simple harmonic oscillator can be described by the following equation:

$$f = \frac{1}{2\pi} \sqrt{\frac{k}{m^*}} \quad (2.1)$$

Where k is the spring constant of the cantilever, and m^* is the effective mass of the cantilever. The cantilever's true mass must be converted to an effective mass because in a spring-mass model, the entire mass of the system oscillates through the same maximum amplitude, while the vast majority of the cantilever's mass does not oscillate through the full amplitude of oscillation. For

a single clamped rectangular cantilever of homogeneous density, the effective mass can be computed to be 0.24 times its true mass(72; 122).

To determine the spring constant of a cantilever, we start with the equation relating the curvature of a singly clamped cantilever beam to the moment induced by a force at its tip (21).

$$\frac{d^2u}{dx^2} = \frac{F(L-x)}{EI} \quad (2.2)$$

Let us assume a solution in the form of

$$u(x) = A + Bx + Cx^2 + Dx^3 \quad (2.3)$$

Since the cantilever is rigidly clamped at its base, we can apply the following boundary conditions stating that displacement and slope of the cantilever are zero at the clamping point.

$$u(0) = 0 \quad (2.4)$$

$$\frac{du(0)}{dx} = 0 \quad (2.5)$$

Applying these boundary conditions to our trial solution requires that the A and B coefficients be zero. Substituting the remaining components of the trial solution into the curvature equation we get.

$$C = \frac{FL}{2EI} \quad (2.6)$$

$$D = \frac{-F}{6EI} \quad (2.7)$$

Evaluating the displacement at the tip of the cantilever we get

$$u(L) = \frac{FL^3}{3EI} \quad (2.8)$$

Dividing the force applied by the displacement of the cantilever at its tip, we get the spring constant.

$$k = \frac{3EI}{L^3} \quad (2.9)$$

Applying this result to the equation for the resonant frequency of an undamped simple harmonic oscillator we get

$$f = \frac{1}{2\pi} \sqrt{\frac{3EI}{m^*L^3}} \quad (2.10)$$

The spring constant is one of the most important characteristics used to describe a cantilever sensor. A cantilever's spring constant is indicative of its sensitivity to a force at its tip, therefore this metric is of great importance to atomic force microscopists. The branching off of microcantilever sensors from AFM means that this metric is still prominently used in describing the physical characteristics of a microcantilever transducer.

2.4.2 Euler-Bernoulli

One of the most widely used analytic models for determining the natural frequency of a cantilever beam is the Euler-Bernoulli beam theory (valid for beams whose length is much greater than thickness or width). As applied to a beam of constant cross section and constant moment of inertia, the natural frequency of a cantilever beam can be determined by solving the following fourth order PDE.(123; 124):

$$\frac{\partial^2 u}{\partial t^2} + c^2 \frac{\partial^4 u}{\partial x^4} = 0 \quad (2.11)$$

where:

$$c^2 = \frac{EI}{\rho A} \quad (2.12)$$

The Euler-Bernoulli PDE is linear and homogeneous, therefore we can solve it using the separation of variables method:

$$u(x, t) = X(x)T(t) \quad (2.13)$$

where the time independent Euler-Bernoulli equation is of the form:

$$X(x) = A\cos(\beta x) + B\sin(\beta x) + C\cosh(\beta x) + D\sinh(\beta x) \quad (2.14)$$

For the case of a single-clamped cantilever we apply the following boundary conditions to the time independent Euler-Bernoulli equation:

$$u(0) = 0 \quad (2.15)$$

$$\frac{du(0)}{dx} = 0 \quad (2.16)$$

$$\frac{d^2u(L)}{dx^2} = 0 \quad (2.17)$$

$$\frac{d^3u(L)}{dx^3} = 0 \quad (2.18)$$

These boundary conditions yield a non-trivial solution to the time independent Euler-Bernoulli equation when:

$$\cosh(\beta L)\cos(\beta L) = -1 \quad (2.19)$$

which can be applied to the following equation to yield the frequencies of the flexural modes of the cantilever beam:

$$\omega = \beta^2 \sqrt{\frac{EI}{\rho A}} \quad (2.20)$$

For the case of a doubly clamped cantilever beam, we apply the following boundary conditions:

$$u(0) = 0 \quad (2.21)$$

$$\frac{du(0)}{dx} = 0 \quad (2.22)$$

$$u(L) = 0 \quad (2.23)$$

$$\frac{du(L)}{dx} = 0 \quad (2.24)$$

These boundary conditions yield a non-trivial solution to the time independent Euler-Bernoulli equation when:

$$\sinh^2(\beta L) + 2\cosh(\beta L)\cos(\beta L) - \cosh^2(\beta L) = 1 \quad (2.25)$$

The first four values of βL that yield nontrivial solutions to the Euler-Bernoulli equation are listed in Table 2.1. When applied to equation 2.20, these values will yield the frequencies of the first four flexural modes of vibration.

2.4.3 Quality Factor and Losses

All of the equations dealing with resonance frequency thus far have assumed that there is no source of mechanical loss, which is never the case in the real world. We can view a cantilever's resonant oscillations as a way to store energy. However, there are a number of processes which take place to dissipate

Table 2.1: Values of βL that satisfy equations 2.19 and 2.25

mode	single clamped	double clamped
1	1.875	4.730
2	4.694	7.854
3	7.855	10.996
4	10.996	14.137

this energy; these phenomena reduce the cantilever's resonance frequency and spectral purity. The sources of mechanical loss are numerous, and quite a few of the mechanisms are poorly understood making their quantification difficult. The cantilever's energy may be lost to environmental sources like viscous damping in liquids or atmosphere. Energy may also be lost to intrinsic sources like clamping losses, motion of defects, grains, dislocations, phonon-phonon or phonon-electron scattering, or surface related phenomena. There are a number of tricks to mitigate the losses caused by these phenomena. Cantilevers can be resonated in vacuum to mitigate viscous damping effects. Torsional beam designs and beams under high tensile stress (125; 110) have been explored to mitigate the effects of nonideal clamping points. Cantilever beams can be cooled (126; 127) to limit phonon related scattering. Surface passivations have also been explored to mitigate dissipation from surface oxidation (128; 129).

Quality factor (also called Q) is a measure of the spectral purity of a resonator, thus a metric that can be used to quantify its mechanical lossiness. Q is a dimensionless parameter and can be defined as:

$$Q = 2\pi \frac{W_0}{\Delta W} \quad (2.26)$$

Where W_0 is the energy of the resonant cantilever and ΔW is the energy lost per oscillation cycle.

A cantilever undergoing damping will have a frequency response in the form of a Lorentzian function (124) and the Q -factor is determined by the ratio of the resonance frequency to the bandwidth of the resonance spectra. The

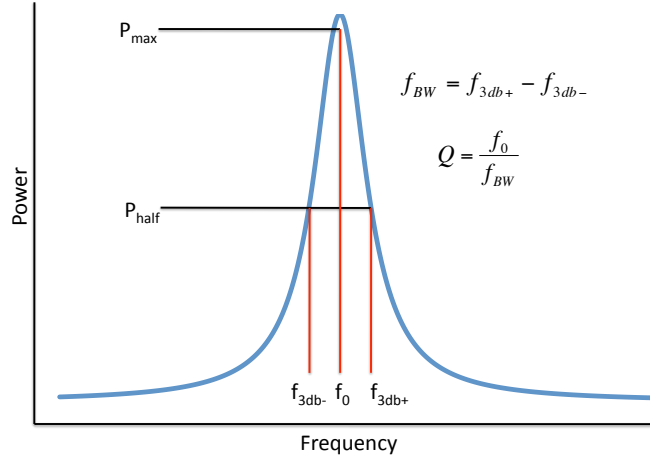


Figure 2.4: Sample cantilever resonance spectra, with half power and frequency bandwidth annotated.

Q-factor is of interest when applying a resonant cantilever as a gravimetric sensor; the higher the Q-factor is, the more accurately small changes in resonance frequency may be resolved (130). A typical way to experimentally assess the Q-factor is to look at its frequency response and apply equation 2.27 to the resonance peak. Q-factor measurements have also been demonstrated through monitoring a cantilever resonator's ringdown time (131; 132). A sample resonance spectra is provided in figure 2.4.

$$Q = \frac{f_0}{f_{BW}} \quad (2.27)$$

Where f_0 is the centre frequency of the resonance peak and f_{BW} is the width of the Lorentz peak at its -3dB point (Half power).

2.4.4 Mass Sensitivity

Resonant cantilever transducers operate by translating changes in resonant frequency into a quantity of adsorbed mass. The simplest and most common model assumes that the adsorbed analyte molecules do not induce any stress (which would also have an effect on the cantilever's resonance frequency) and that the added mass is small compared to that of the cantilever. In this case, we can derive a simple approximation from equation 2.1 and correlate the change in resonance frequency to the added mass with the following equation.

$$\frac{\Delta f}{f} = \frac{-1}{2} \frac{\Delta m}{m} \quad (2.28)$$

One must note that the mass in this equation is the effective cantilever mass and that this is valid only if the added mass is distributed evenly over the surface of the cantilever transducer and the cantilever is excited at its first mode. This equation or minor variations of it have been applied for a wide array of cantilever transducers (133; 79; 33; 130; 32).

From equation 2.28, we can clearly see that the lower a cantilever's mass is the more its frequency will shift with a given adsorbed mass. Indeed it has been shown that the mass sensitivity for a distributed load is dependant on the density and thickness of the cantilever (122; 73; 72):

$$S_m = \frac{1}{\rho t} \quad (2.29)$$

Knowing the minimum detectable frequency (from instrumentation limitations), we use the sensitivity to determine the cantilever transducer's minimum detectable mass using the following equation (122; 73; 72):

$$\Delta m_{min} = \frac{1}{S_m} \frac{\Delta f_{min}}{f} \quad (2.30)$$

Thus, for a resonant cantilever sensor, we desire to use a material that is stiff

for high resonant frequency and has a low density so that the binding of light analyte molecules may be more significant compared to the cantilever's mass.

Ekinci *et al.* (134) performed a more in depth analysis of nanocantilevers, taking into account the real world signal to noise issues that are inherent in any measurement to determine the minimum detectable mass for a nanoresonator.

$$\Delta m_{min} \approx 2m_{eff} \sqrt{\frac{\Delta f}{Q\omega_0}} 10^{\frac{-DR}{20}} \quad (2.31)$$

Where m_{eff} is the effective mass of the resonator, Q is the quality factor and ω_0 is the angular frequency of the resonant oscillation. DR is the dynamic range and can be calculated as the ratio of amplitudes A_{signal} and A_{noise} . Δf is the measurement bandwidth and is defined as $\Delta f = \frac{f_0}{Q}$. This result has been used subsequently in numerous publications on mass sensitivity of resonant cantilevers (12)(135)(136)(137). From this analysis we see that both the resonator's mass and quality factor are important values to optimize in order to optimize mass sensitivity, as well as tailoring the resonator to minimize the noise in assaying.

If the analyte in question induces a significant surface stress on the cantilever, this effect must also be decoupled from the mass signal. Chen *et al.* (79) solved this issue with a position sensitive detector to directly measure cantilever bending while simultaneously measuring the first mode of resonance. Bending information was translated into a virtual spring constant (using a string model for the cantilever), which can be added to the cantilever's real spring constant to account for surface stress effects. More recent investigations (138; 139; 54) into decoupling mass and stress effects have centred more around exploiting the difference in the cantilever's frequency dependence on added mass and stiffness as the mode number is increased.

2.5 Static Mode

A cantilever transducer operating in static mode detects the presence of an analyte of interest due to stress imparted by binding of that analyte to the surface of the cantilever. Static mode cantilever sensors do not operate in a way that is comparable to any of the transducer technologies outlined in chapter 1, and thus require a bit more of an introduction. This section will outline the principles of static mode cantilever operation, the Stoney model and its application, optimization of cantilever design, and the strengths and weaknesses of static cantilever sensors.

It has been demonstrated that static cantilevers can be applied as calorimeters with femto-joule level sensitivity (140; 75; 76). This level of thermal resolution enables the detection of chemical reactions at the surface of the cantilever (77). Apart from deflection due to the thermal signature of a reaction, it is important to note that there is a second source of deflection that must be studied; the change in surface free energy. Consider a solid metal slab, all forces on the atomic nuclei in the metal can be ascribed to Coulomb forces caused by electron distributions around the nuclei. If we bisect the solid, the electron distributions at the new surface must rearrange to account for the absence of neighbouring atoms, thereby creating a mild tensile stress (141). The relation between surface stress and surface free energy is described by the Shuttleworth equation (142). The adsorption of analyte molecules on to the surface of a solid will modify the electronic structure at its surface and thus modify the surface free energy (typically causing a relaxation interpreted as a compressive stress (73)). It is important to note that both these phenomena are important in the application of microcantilevers for static sensing.

Typically, to prepare a cantilever for a stress sensing application, only one side of the beam is modified so that it interacts preferentially with the analyte of interest, while the other side does not. Consequently, adsorption events only occur on the sensitized side of the cantilever, modifying its free energy and inducing a stress which results in cantilever deformation. This model for

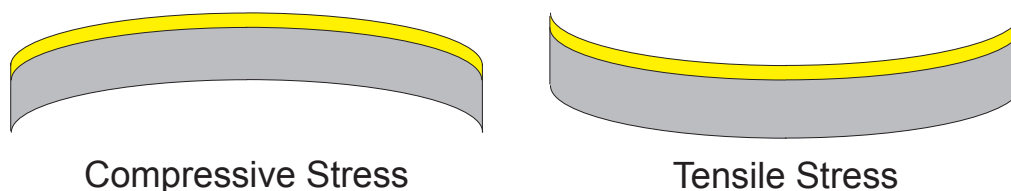


Figure 2.5: Schematic diagram of the bending of a substrate due to stress induced by the deposition of a compressive or tensile thin film.

cantilever bending describes the stress induced by thin coatings on ideal surfaces. If the cantilever is modified with a chemically sensitive layer that is permeable and much thicker than a monolayer (like a polymer), the dominant source of deflection signal may arise from the swelling of the chemically sensitive layer(143; 73). In either case the cantilever bending is typically applied to Stoney's model to quantify the stress imparted by the target analyte.

2.5.1 Stoney's Equation

Stoney's equation continues to be most widespread model for determining the curvature of a plate due to the deposition of a thin film (144; 145). The equation was developed to describe the bending of a steel plate due to the electrodeposition of a nickel film. Stoney's equation has found widespread application in the microelectronics and MEMS industries to determine and control the stress of thin films to ensure that devices will not be damaged by stress induced deformation, buckling or delamination. Stoney's equation is as follows

$$\sigma = \frac{Eh^2}{6R(1 - \nu)} \quad (2.32)$$

where σ is the surface stress induced by the deposited film, E is the Young's modulus of the substrate material, h is the substrate thickness, R is the re-

sultant radius of curvature of the substrate and ν is the Poisson's ratio of the substrate material

The Stoney equation is applied when the deposited thin film is uniform and much thinner than the substrate thickness and the material properties of both substrate and film are isotropic.

Since Stoney's equation was derived for unconstrained substrates, there has been much discussion about its validity with respect to cantilevers which are rigidly constrained at the clamping point. Investigators have specifically worked towards corrections to Stoney's equation for cases where the deposited film is on the same order of thickness as the substrate (146) or where the cantilever length to width ratio is small and results in heightening the effect of the clamping point (147). However, if these design pitfalls can be avoided, Stoney's equation can be used accurately (without need for correction) for cantilevers in general (52; 145) and AFM cantilevers in particular (79; 148).

2.5.2 Stress Sensitivity

The spring constant of a cantilever is often quoted as a measure of its compliance. Technically, the spring constant is a measure of the cantilever's compliance to a point force. Static cantilever sensors however do not measure a point force, they measure the distributed force of a surface stress. Stoney's formula accurately relates the surface stress on a plate to its radius of curvature. However most researchers use PSDs to measure the deflection of the tip of a cantilever and not the radius of curvature. To adapt Stoney's formula to cantilever tip deflection, one can apply the following relations between the radius of curvature and the cantilever tip deflection (82; 148; 149).

Using the construction in figure 2.6 z and y can be defined as:

$$z = R - \Delta z \tag{2.33}$$

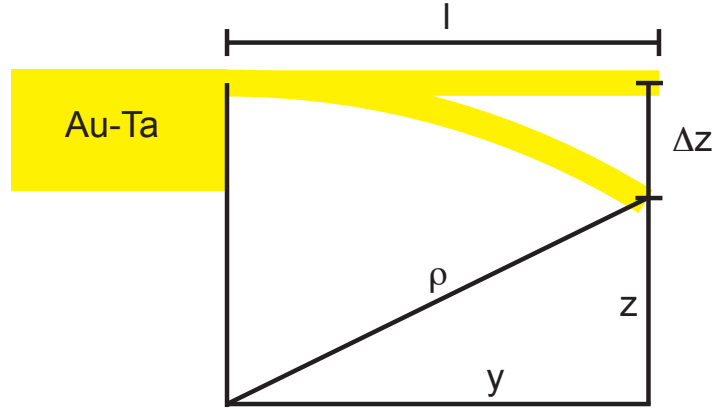


Figure 2.6: Schematic diagram of a cantilever undergoing bending due to surface stress

$$y = l - \Delta y \approx l \quad (2.34)$$

We can then use Pythagorean theorem to relate the radius of curvature of the beam to z and y :

$$R = \sqrt{y^2 + z^2} = \sqrt{l^2 + (R - \Delta z)^2} \quad (2.35)$$

Simplifying for small deflections

$$R = \frac{l^2}{2\Delta z} + \frac{\Delta z}{2} \approx \frac{l^2}{2\Delta z} \quad (2.36)$$

If this is applied to Stoney's formula stress and cantilever deflection are correlated by:

$$\sigma = \frac{Eh^2\Delta z}{3l^2(1-\nu)} \quad (2.37)$$

From equation 2.36 we can see that if we want to design a static cantilever

Table 2.2: Summary of suitable environments, sources of noise and desirable properties for static and dynamic cantilever transducers.

Transduction type	Suitable environments	Sources of noise	Desirable properties
Static	Ambient, Liquid	Temperature, Solution flow (in liquid)	Long and thin dimensions, low intrinsic stress
Dynamic	Vacuum, Ambient	Viscous damping, Surface effects, Stress	High E, Low ρ , Thin dimensions

of high sensitivity we need to focus on materials and processes that enable fabrication of extremely thin and long cantilevers.

2.6 Contrasting Transduction Methods

Static and dynamic transduction methods are two very different strategies for applying cantilevers as bio and chemical transducers. Both methods work well in different environments, making the general field of cantilever sensors quite robust in terms of application flexibility. Both transduction methods also have their own proper design criteria for optimizing sensitivity, and their own distinct sources of noise. A quick summary of the respective strengths and weaknesses as well as the desirable optimization parameters is described in table 2.2.

2.7 Readout Methods

In a sensor, the transducer operates by translating the physical change brought about by the detected target into a signal which we can interpret. In the case of a resonant cantilever sensor, a bound analyte induces a change in resonance frequency and quality factor, while in a static cantilever sensor, a change in the

surface stress caused by adsorbed analyte induces a deflection in the cantilever. The choice of readout method is of critical importance in the application of cantilever sensors. Depending on the application of the cantilever sensor or cantilever design constraints, certain readout methods may not be a good choice. Below is a short summary of a number of readout technologies for static and resonant cantilever sensors with a focus on their strengths and weaknesses.

2.7.1 Optical Methods

Optical Lever

The position sensitive detector method is one of the most popular cantilever sensor readout methods in literature and is described in a number of review articles (149; 73; 150; 122). This is the same method which is used to track deflection or frequency shift in an AFM cantilever as explained briefly in chapter 1. This method is sometimes called the “optical lever” method. A laser spot is reflected off a cantilever beam onto the intersection of a quadrant photodiode. The voltages from the respective quadrants of the photodiode provide information about the deflection of the cantilever, which is fed back to a piezo stack that keeps the reflected laser spot close to the intersection of the split photodiodes so that the deflection signal is not lost. This method can be used for deflection as well as resonant cantilever transducer readout since the piezo stack can be used to excite the cantilever beam at its resonance frequency. The oscillation of voltage between upper and lower PSD quadrants can be correlated to the cantilever’s resonant frequency, while the mean PSD voltages can be correlated to the cantilever deflection. This method was pioneered by Meyer and Amer (151; 152) as an improvement to the AFM and it has since become the standard bearer for AFM tools. The deflection resolution of this method is reported to be 10^{-14} m (73). While the optical lever method may be the most widely used readout method, it does have some drawbacks that have limited its use. Firstly, changes in the optical properties of the medium surrounding

the cantilever can interfere with signal interpretation. Also, the optical lever method can only be used for applications in which the cantilever medium is not opaque. The bandwidth of the PSDs are also a limiting factor that constrain readable frequencies typically to the range of hundreds of kilohertz; of course this is not an issue in static mode operation. One example of a commercially available cantilever readout system based on the optical lever principle is the Cantisens system marketed by Concentris. The Cantisens system uses the optical lever technique with a multiplexed laser to monitor the resonance frequency or deflection of eight microcantilevers (153; 154) in either a liquid or gaseous environment.

Interferometer

Interferometry is another well explored optical method for cantilever frequency or deflection readout. There are a number of methods to implement an interferometer to readout the frequency of a cantilever. A Fabry-Perot type interferometer design is a robust method which was demonstrated by Carr and Craighead (155) to measure the deflection and resonance frequency of silicon cantilever bridges fabricated out of SIMOX. A laser is used to illuminate the silicon beams through a beamsplitter and a microscope objective. The laser spot reflects off of the cantilever beam and the substrate, returns back through the microscope objective and is reflected off the beamsplitter and focused and combined on a photodetector. Part of the optical signal at the photodetector is due to the optical path difference between the top of the cantilever and the reflection off the substrate. Any deflection that the cantilever undergoes will cause a small modulation of the light intensity at the frequency of the cantilever. Naturally, this signal will be greatest when the cantilever is excited at its resonance frequency. A spectrum analyzer can be used to readout the photodetector data and simultaneously provide a drive signal via its tracking output. The cantilever can be excited to resonance by a number of methods including inertial drive with a piezo disc (109), electrostatic actuation (108) and thermal actuation (156). This type of interferometry is employed for the

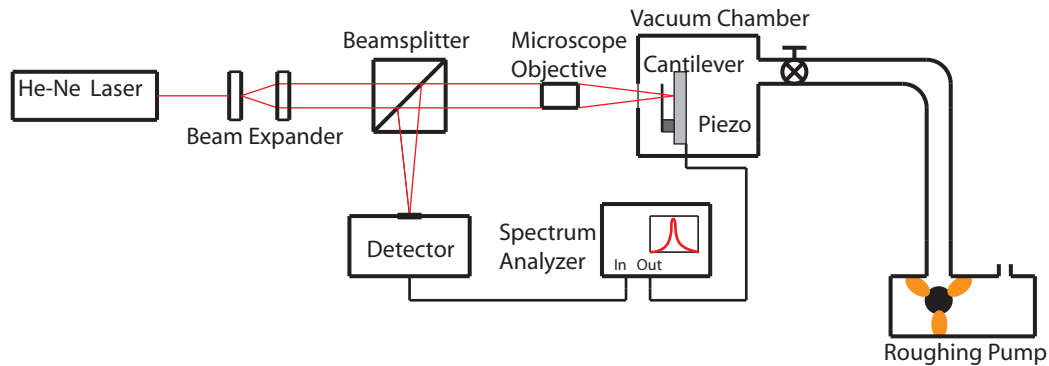


Figure 2.7: Schematic diagram of a resonance assaying interferometer setup.

work conducted in chapters 3 and 4 of this thesis and a schematic representation of this type of interferometer setup using a piezo disc is provided in figure 2.7.

Most interferometry uses lasers or other light sources with a long coherence length because this property facilitates in obtaining an interference pattern. To obtain an interference pattern, the optical path length (OPL) of the different arms of an interferometer must be matched to be within the coherence length of the interferometer's light source. Usually a short coherence length is regarded as bothersome, but it does confer one advantage. We can measure the topology of a sample by treating it as a mirror at the end of one arm of an interferometer. This method is however susceptible to confounding when there is a height discontinuity of greater than $\lambda/4$, since that would constitute a difference of 180° in phase. This confounding is essentially aliasing as described by Nyquist-Shannon sampling theory. By purposefully using a short coherence length source of light, one can limit the interference to a small envelope of height. By limiting the interference to only a small fringe envelope we can precisely determine what part of the sample is exactly matched in OPL with a reference arm, thus allowing accurate mapping of the sample's height. This is the principle behind white light optical profilometers (157). A representation of a white light interferometry fringe envelope (fringe intensity vs difference

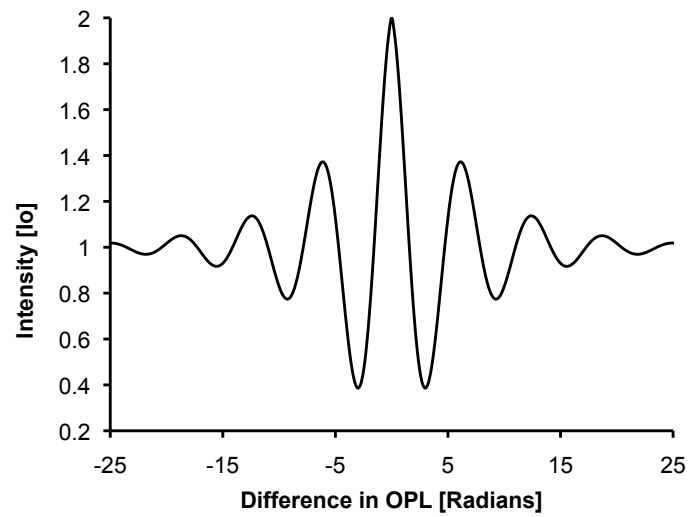


Figure 2.8: Graph of intensity vs difference in optical path length for a white light interferometer. As the optical path lengths of the two arms of the interferometer become further apart the fringe intensity is drastically reduced.

in reference arm optical path length) is provided in figure 2.8. White light interferometers are commonly used to nondestructively measure step heights, surface roughness and critical dimensions in MEMS devices with nanometre level resolution in the z direction. O'Mahony *et al.* (158) used scanning white light interferometry (SWLI) to analyze the profiles of various MEMS devices and summarized its strengths as a fast, non-destructive, non-contact method that usually requires no sample preparation to accurately measure z height. This is of great importance because SWLI provides a quick way to determine whether MEMS devices have undergone destructive buckling due to stress. Fang and Wickert (159) demonstrated SWLI's usefulness by profiling cantilever structures and their clamping points to determine the mean and gradient stress in the cantilever material. SWLI does have some limitations that reduce its usefulness. Firstly it is not capable of accurately measuring the step height of optically transparent materials like SiO_2 . Secondly, using the sample as a mirror means that structures with significant angular deflections may reflect probing light away from the interferometer's detector, giving an incomplete image. White light interferometry has been used in the work outlined in chapter 5 of this thesis and a diagram of a white light interferometer assaying the height profile of a bent cantilever is provided in figure 2.9.

Laser Doppler Vibrometer

A laser Doppler vibrometer is a sensor that uses interferometry and the Doppler effect to extract the velocity and phase information of a resonating structure. A laser light is used as the source for a modified Mach-Zehnder interferometer. The probe beam goes to the MEMS device being queried, device displacement is encoded in the phase information and device velocity is encoded in the frequency of the reflected beam (160). The probe beam is recombined with a frequency shifted reference beam and the mixed signal is decoded to translate the displacement and velocity information. This method can be used for transient as well as periodic motions (161). Polytec is a prominent commercial supplier of a wide variety of laser Doppler vibrometers with both single

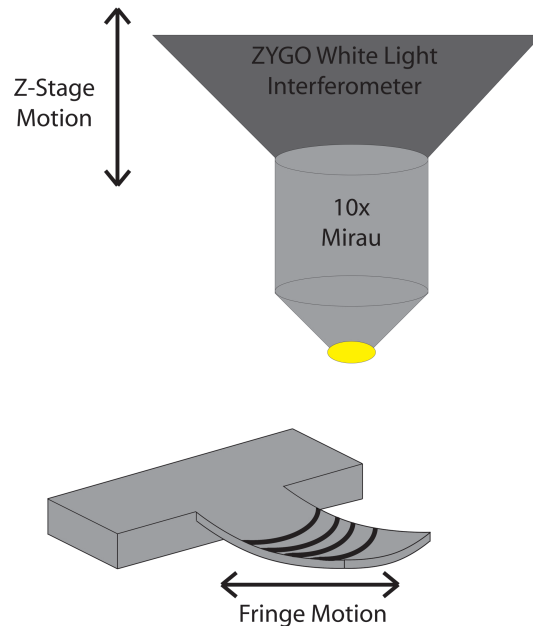


Figure 2.9: Schematic diagram of a white light interferometer setup.

pixel and scanning abilities (162; 163). Scanning laser Doppler vibrometers have been used for the characterization of more complex MEMS structures like paddle oscillators (164; 165) and comb-drives (166). There are some limitations to laser Doppler vibrometry as a tool. Like other optical tools this system takes up a large footprint and demands that the optical medium surrounding the structures be relatively stable and not opaque. The laser Doppler vibrometer is better suited to map the mode shapes of MEMS a cantilever, which can be advantageous for decoupling mass and stress effects on a device's resonance frequency.

2.7.2 Electrical Methods

Tunnelling

Electron tunnelling is an electrical cantilever transduction method that has been explored, although it is more commonly associated with scanning tun-

nelling microscopy (STM). A conductive cantilever beam with a sharp tip (like an AFM cantilever) is brought in near contact with a conductive counter-electrode by an electrostatic force (167). The cantilever's response to an analyte can be determined by the tunnelling current. However, a feedback loop is required to maintain a constant tip-electrode distance since small forces would quickly let the microfabricated cantilever cross the ~ 10 nm gap and impact the counter-electrode. Tunnelling current is highly sensitive to displacement and has been shown to measure cantilever displacements as low as 10^{-4} nm (73). Scheible *et al.* (168; 169) have used this transduction technique to explore improved low-loss resonator geometries with the vision of improved RF filters. Extreme deflection sensitivity is an attractive property of a tunnelling transduction scheme, but it is also very sensitive to the materials between the electrodes, and is relatively infrequently used in literature. Additionally, the requirement of a conductive surface necessitates the incorporation of a metal coating on the cantilever which has been demonstrated to lead to poorer Q-factor in resonant cantilever transducers (109).

Piezoresistive

The piezoresistive approach is a particularly elegant method for the readout of silicon cantilever transducers. Piezoresistivity is the change in resistance due to an applied stress (149; 73) and doped silicon is a material that exhibits a strong piezoresistive effect. Not only can one exploit the property that P-doped silicon is an effective etch stop layer for KOH based etchants when machining silicon cantilevers, the same material exhibits this fortuitous piezoelectric effect. Of course this technique has some geometrical limitations and would require a doped channel or a two-legged cantilever which we could measure the resistance across. The change in resistance associated with the cantilever's strain is typically read out by a dc-biased wheatstone bridge. The typical resistance of a boron doped silicon microcantilever is in the range of a few kilo-ohms ($k\Omega$). The advantages of a piezoresistive readout mechanism are that it is compact and much of the readout circuitry can be integrated on

chip. Additionally piezoresistive transduction is ideal for applications in which the optical properties of the medium will confound optical readout techniques, and it is unaffected by the conductivity of electrolyte buffers that can be necessary for biosensing applications. Unfortunately, piezoresistive transduction does place design limits on cantilever dimensions and materials, and resistive heating from the readout mechanism may cause a bending signal of its own which would need to be deconvolved from the actual analyte signal.

Cantion A/S (153; 170) (since taken over by NanoNord A/S) designed commercially available piezoresistive chips, readout and fluid handling systems which have been used by a number of investigators for chemical sensing applications (89) (85). A notable application of piezoresistive transduction was innovation by Li *et al.* (171) to apply thin metal films as the piezoresistive layer for SiC nanocantilevers. Metals have a low piezoresistive gauge factor, but the deformation a metal film undergoes when the cantilever is stressed will cause a relatively small change in resistance (20x less than doped Si). This much smaller change in resistance was compensated for by much improved impedance matching between the cantilever and the readout electronics so that cantilever signal was not lost (estimated 10^4 fold improvement). Au metal has also been incorporated as a piezoresistor in SU-8 polymer cantilevers for static chemical sensing presented by Johansson *et al.* (172; 173).

Capacitive

Capacitive measurements have been studied as a transduction method for AFM cantilevers (174) and some smaller cantilever devices. In this method changes in capacitance between a metalized cantilever and a reference electrode are related to cantilever displacement and frequency. This transduction method is compatible with standard CMOS technology, which is advantageous for mass production and integration (73). Capacitance between two plates is proportional to plate area and inversely proportional to plate distance. Thus as a cantilever sensor is scaled down, the distance between cantilever and sensing

electrode must be reduced drastically. Capacitive transduction is also susceptible to confounding by changes in dielectric constant between the cantilever and sensing electrode, which has limited its applications in liquid environments. Additionally, as with the tunnelling sensor, the addition of a metal layer is deleterious for resonant applications.

2.8 Summary

In this chapter we provided an overview of principles involved in the fabrication, design, modelling, and readout of static and dynamic cantilever transducers. Bulk and surface machining methodologies were described and their benefits and limitations were explored. Theories to describe the resonant and static behaviour of cantilever structures and their limitations were summarized. These theories were used to illustrate principles behind the design of static and resonant cantilever transducers. Lastly, common methods used to quantify cantilever transducer signal were described and their advantages and drawbacks were summarized.

CHAPTER 3

Single Crystal Silicon Nanocantilevers

3.1 Introduction

This chapter is a record of the development of nanocantilever resonators in silicon¹. Silicon is one of the more common materials for nanocantilever resonators and the wealth of literature available enabled easier troubleshooting of fabrication techniques and characterization of the resonators. Some of the techniques, recipes and expertise developed for this project were directly applied in subsequent chapters. This work was completed in the University of Alberta Nanofab and electron microscope inspection was performed at the National Institute for Nanotechnology (NINT).

3.2 Silicon on Insulator

Silicon is a relatively common material to fabricate surface machined micro and nanocantilevers from (176) due to its ubiquity in the microelectronics field

¹A version of this chapter was published in Ref. (175). All data analyzed and interpreted by N. Nelson-Fitzpatrick. All fabrication was performed by N. Nelson-Fitzpatrick. Resonance measurement was performed by N. Wilding and N. Nelson-Fitzpatrick. DRIE recipe was adapted by N. Nelson-Fitzpatrick with technical guidance from P. Li and S. McColman. Additional guidance was provided by K. Westra.

and a wide array of processes available to machine it. One common technique for fabricating surface machined MEMS and NEMS (including cantilevers) is to exploit silicon on insulator (SOI) wafers. Carr *et al.* (155) were the first to apply SOI to fabricate cantilever nanoresonators and subsequently studied loss mechanisms as the surface to volume ratio of the structures was increased (108). SOI is ideal for many MEMS and NEMS devices that can be surface machined because it comes with a built-in sacrificial layer. Additionally, resonant cantilever devices benefit from the ability to machine devices out of a single crystal material, avoiding polycrystalline sources of dissipation. Celler *et al.* (177) have published a comprehensive review of the many ways to fabricate SOI wafers. For micron scale device layer and sacrificial layer thicknesses, a wafer bonding method like BESOI or Smart Cut (178) is employed. These methods involve growing an SiO_2 layer on a single crystal Si substrate, then fusion bonding this wafer to a “handle” silicon wafer, and removing silicon from the original oxidized wafer until the device layer is ground down to the desired thickness. For nanometre scale applications SOI is generally synthesized by a technique called Separation by IMplantation of OXYgen or SIMOX which was first described by Izumi *et al.* (179). SIMOX wafers are formed by high dose ion implantation of O^+ into a single crystal Si wafer. Annealing is required during implantation to prevent crystal damage and afterwards to promote the formation of a uniform SiO_2 layer. SIMOX SOI wafers (device layers of 200 nm and 50 nm, with BOx layer of 370 nm) from IBIS technology were used in this work.

3.3 Cantilever Fabrication

The fabrication of silicon nanocantilevers was conducted using a surface machining methodology very similar to that described in Figure 2.3. The substrates were cleaved into approximately 1 cm x 1 cm dies, then cleaned with a sequence of hot Piranha (3 H_2SO_4 : 1 H_2O_2) to remove organics and buffered hydrofluoric acid (1 HF: 10 NH_4F) to remove the native oxide. The samples

were then dehydrated on a hot plate at 200°C for 5 min in the ambient atmosphere of a class 10 environment. A 60 nm thick polymethylmethacrylate (PMMA) 495K electron beam resist was spun and then baked at 180°C for 30 min. This step was then repeated with a 60 nm thick PMMA 950K resist, creating a bilayer for lift-off. The substrates were patterned with a Raith150 Electron Beam Lithography (EBL) system and developed in a methylisobutylketone based developer (1 MIBK: 3 IPA). The patterned resist is then subjected to a light O₂ “descum” plasma to smooth any roughness in the resist template resulting from nonideal developing. The patterned resist was then used to generate a 30 nm thick chrome masking layer by electron beam evaporation and lift-off of the unexposed areas. In preparation for the cryogenic etching technique, the silicon substrates were once again cleaned, this time with a hot piranha solution (2 H₂SO₄: 1 H₂O₂) and buffered hydrofluoric acid. The samples were then bonded to a handle Si wafer by using HPR 504 photoresist as an adhesive and baking on a vacuum hotplate for 5 min. The handle wafer and die were exposed to the cryogenic DRIE process, removing all unmasked silicon on the device layer of the SOI chip. The Cr mask is then removed with a 5 min bath of chrome etchant (care must be taken as the quoted etch rate is not very accurate for such thin layers). The cantilevers are now released by etching away the SiO₂ in a buffered hydrofluoric acid bath (timing dependant on cantilever critical dimensions) which is rinsed successively with deionized water (DI) and isopropyl alcohol (IPA). The die is then kept submerged in a beaker of IPA and transferred to a Tousimis critical process dryer, where the IPA is slowly replaced by liquid CO₂ under pressure then heated beyond the critical point. Beyond this critical point the CO₂ exerts no surface tension as it is removed (180), allowing the release of freestanding cantilevers without destructive stiction effects. Details of the electron beam lithography and cryogenic etch steps are provided below.

3.3.1 Electron Beam Lithography

Electron beam lithography (EBL) is a high resolution maskless lithography technique that is often used to define nanostructures. Typical lithography techniques use a source of optical radiation to expose a photosensitive polymer “photoresist” through a mask which can then be developed and used as a mask for further etching or deposition steps. The ultimate resolution achievable by these optical techniques is limited by the wavelength of the lamps used. Alternatively, electron beam lithography uses a scanning electron microscope column to focus electrons down to a small spot on the order of 20 nm. Typical accelerating voltages for electron beam lithography vary from 1 kV to 100 kV. This spot is typically rastered across a sample coated with an electron beam sensitive polymer like PMMA (Poly-methyl methacrylate) or HSQ (Hydrogen silesquioxane), which is then developed and the pattern is transferred to the device material. The drawback to this lithography technique is the serial nature of exposure yielding a slow throughput, as the beam must be slowly moved across the sample exposing each part of the desired pattern in steps smaller than the beam spot size.

The Raith150 is a low voltage EBL system with a range of 0.2 kV to 30 kV accelerating voltage. The accelerating voltage used determines the interaction volume, that is the volume of material (resist, substrate) that the electron beam will impinge. A lower accelerating voltage constrains the interaction volume near the surface of the material (in the e-beam resist), effectively decreasing resolution but also decreasing the number and range of backscattered electrons which may cause unintentional exposure (181; 182). Alternatively, a high accelerating voltage increases the interaction volume and the range and number of backscattered electrons, but keeps the beam spot well focused through the resist layer which can improve resolution. However, with good process optimization low accelerating voltages can still achieve excellent resolution. Mohammad *et al.* recently demonstrated 11 nm released beams patterned with a 3 kV e-beam lithography process (111). Figure 3.1 is a comparison of the simulated paths of 200 electrons computed using CASINO (183), a Monte

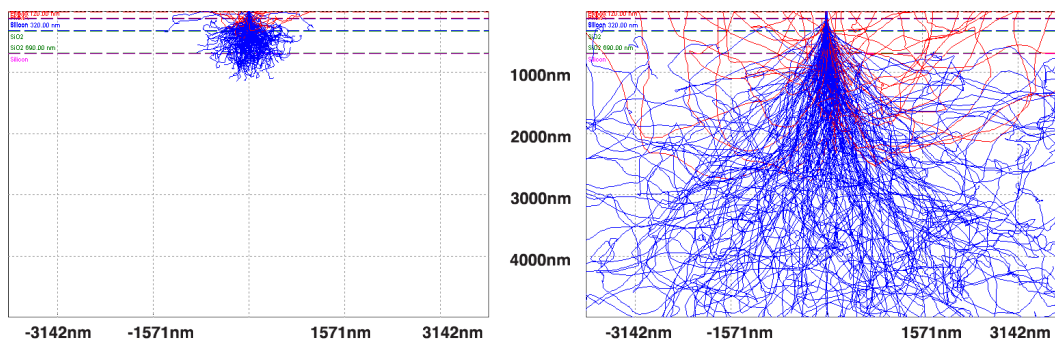


Figure 3.1: Output from CASINO simulation displaying electron trajectories for 10kV and 30kV electron beam lithography spot.

Carlo based electron simulator for solid materials.

Figure 3.1 shows that the interaction volume is much more constrained and the backscattered electrons are fewer in the 10 kV simulation than in the 30 kV simulation. A 10 kV accelerating voltage was subsequently used since the drop in achievable resolution is rather small, and the relief of proximity effects greatly simplifies e-beam pattern design. PMMA was chosen as the E-beam resist since its properties are well understood and it is a positive resist, where the portions of the resist exposed to the electron beam become soluble in the developer. This is important if we wish to apply a lift-off process for transferring our pattern into a thin film, (a Cr mask in this chapter).

3.3.2 Cryogenic Reactive Ion Etch

Once the cantilever pattern has been transferred into the Cr mask layer, we need to transfer this pattern into the silicon below. There are many ways to etch silicon, but if we wish to pattern very fine features with reliable control over the resulting width of the silicon beam, we need to employ an anisotropic etch technique. Isotropic etches like a plain SF_6 RIE will etch uniformly in all directions causing line features to be smaller than designed and trenches to be larger. Figure 3.2 is an illustration of the etch profiles of an anisotropic and an

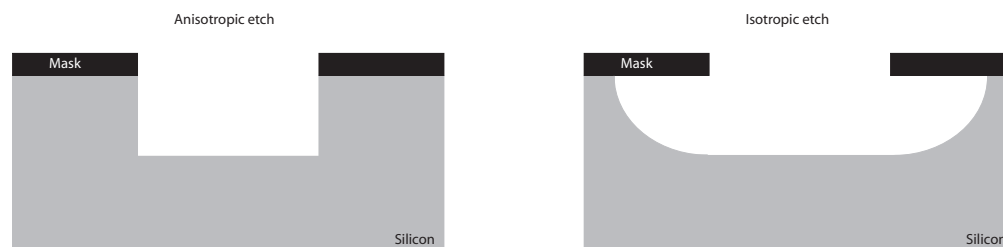


Figure 3.2: Illustration of anisotropic and isotropic etch profiles on a trench feature.

isotropic etch. For devices with critical dimensions in the micron range, and etch depths in the nanometre range, this may be an acceptable compromise. However, this nonideality would wipe out the fine features of nanodevices. One must therefore employ an anisotropic etch technique. One of the most common anisotropic RIE techniques is the Bosch process. This process alternatively applies etch and passivation (eg. SF_6 and C_4F_8) plasmas over a prescribed number of cycles resulting in the machining of microstructures with aspect ratios exceeding 20:1. Bosch etch technology is however prone to producing submicron scalloping defects on the sidewalls of the etch channel, which could be disabling for devices with critical dimensions in the 100 nm range. Alternate RIE chemistries have been explored for high aspect ratio etching in silicon, but these methods are often highly sensitive to environmental issues in the process chamber like wall conditions, temperature or gas flow which may vary from run to run and chamber to chamber. A more robust highly anisotropic etch technique would be ideal.

The recent years have seen the development of anisotropic silicon etch techniques operating at low temperatures (120; 184). In these techniques, the silicon substrate is cooled to cryogenic temperatures while being exposed to halogen-containing plasmas mixtures such as SF_6/O_2 . Cooling is leveraged to control the deposition of a SiO_xF_y passivation layer on sidewalls, which

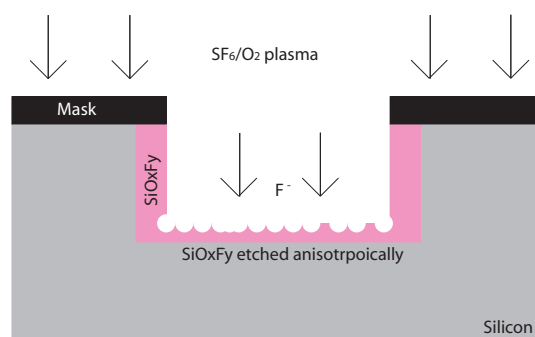


Figure 3.3: Schematic diagram of the cryogenic reactive ion etch process. Silicon oxyfluoride passivation is deposited all over the trench structure. The passivation layer is etched physically by ion bombardment exposing the trench bottom to chemical attack from radical species.

blocks fluorine ions from chemically etching them. The etch profile is controlled by a balance between the deposition of passivating silicon oxyfluorides on the sidewalls and the etching of the trench bottom (which is dependant on ion bombardment from the plasma). Figure 3.3 is a schematic showing the two mechanisms of the cryogenic etch process acting on a trench structure. This ability to both passivate and etch at the same time has been successfully employed for the development of waveguide structures in silicon (185).

We chose to develop a cryogenic anisotropic silicon etch recipe similar to those published before (120; 184), optimizing the recipe for nanocantilever structures. This cryogenic etching process consists of four steps. First the wafer is loaded into the plasma reactor and rests on the cooled chuck for 5 min in order to achieve the desired temperature (-120°C). We have used 1 cm^2 dies of SOI bonded to bare Si wafers to avoid waste of material while ensuring control and reproducibility of the etch rate. Second, an O_2 plasma is run for 10 s, to clean the silicon substrate and prepare it for etching. Third, the SF_6/O_2 etching plasma is lit to etch the substrate. The duration of this step depends on the depth of the desired etch. A 22 s etch was used for 200 nm thick silicon

Table 3.1: Process steps for cryogenic etching.

Process step	Time	Temp (°C)	Pressure (mTorr)	ICP power (W)	RF power (W)	He press. (Torr)	SF ₆ flow (sccm)	O ₂ flow (sccm)
Pump / cool	5:00	-120	N/A	0	0	N/A	0	0
Oxygen plasma	0:10	-120	4	150	20	10.0	0	20
Etch	0:10	-120	10	500	3	15.0	40	9
He re-release	5:00	-120	N/A	0	0	N/A	0	0

devices while a 10 s etch was used for 50 nm thick samples. Lastly, a helium release step is used to ensure that the process wafer is not stuck to the cooled chuck. The parameters employed are detailed in Table 3.1.

After etching the devices, the Cr mask is removed and the structures are released with a buffered HF etch of the SiO₂ and a critical point dry step. A scanning electron micrograph of our resulting cantilever beams is provided in figure 3.4.

3.4 Resonance Data

Our released cantilevers were mounted in an interferometric resonance measurement setup as described in section 2.7. We evacuated the chamber (roughing or turbomolecular pump) to below 10 mTorr to mitigate viscous and squeeze damping effects. The chip was driven by a piezo disc attached to the tracking output of the spectrum analyzer. Resonance frequencies of 400 nm and 800 nm wide single clamped cantilever beams of varying length (4 μm to 14 μm) were measured for first and second flexural modes. Figure 3.5 is a sample resonance spectra from a 400 nm wide single clamped cantilever beam. We measured the quality factor for individual cantilevers by fitting a Lorentz probability distribution function to the recorded resonance spectra.

The quality factors of the assayed cantilever resonators varied from 744 to

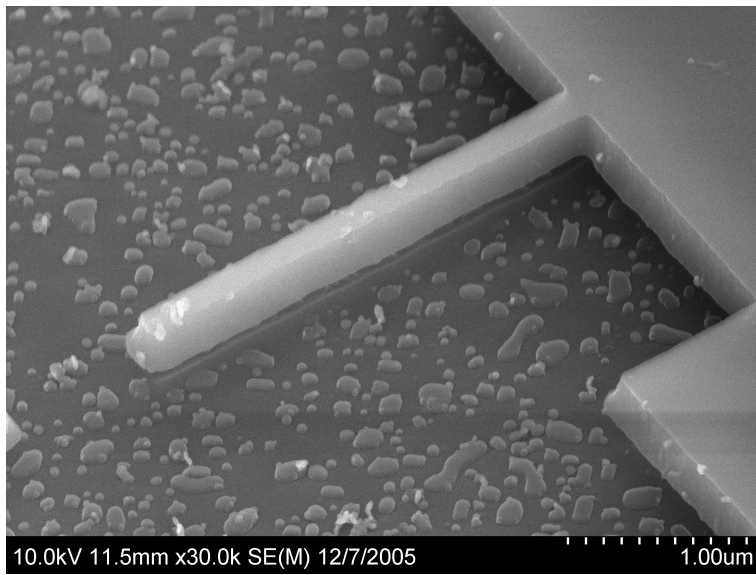


Figure 3.4: 150 nm wide silicon cantilever beam etched by cryogenic process and released with buffered HF and CPD. Artifacts below the cantilever are believed to be an artifact of the SOI synthesis and unrelated to our processing.

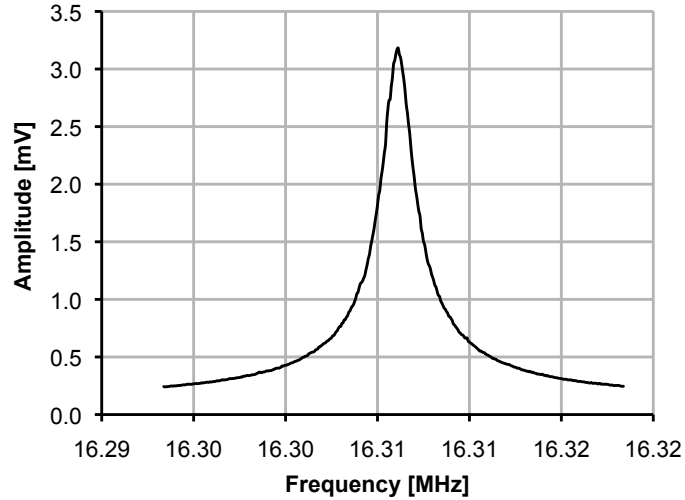


Figure 3.5: Resonance spectra of the first mode of a 400 nm wide, 4 μm long, 200 nm thick silicon cantilever etched using the cryogenic RIE process.

13100. Correctly interpreting the Q-factor can be difficult since it may be influenced by many mechanical and electrical phenomena resulting from both intrinsic material limitations or extrinsic processing factors. The resonance frequency of cantilever beams however tells us a lot about their mechanical characteristics. Using the Euler-Bernoulli equation (2.20), the frequency of the first mode ($\beta L = 1.875$) of these rectangular silicon cantilevers (moment of inertia: $I_{rect} = \frac{wt^3}{12}$) can be predicted by the following equation.

$$f = \frac{3.516t}{2\pi L^2} \sqrt{\frac{E}{12\rho}} \quad (3.1)$$

By using a least squares fit of the cantilever's frequency to its length we may extract the speed of sound $\sqrt{\frac{E}{\rho}}$ in the device material. Figure 3.6 is a plot of the fundamental resonance frequency (to the power -0.5) versus cantilever length of a series of 400 nm wide SOI cantilever beams.

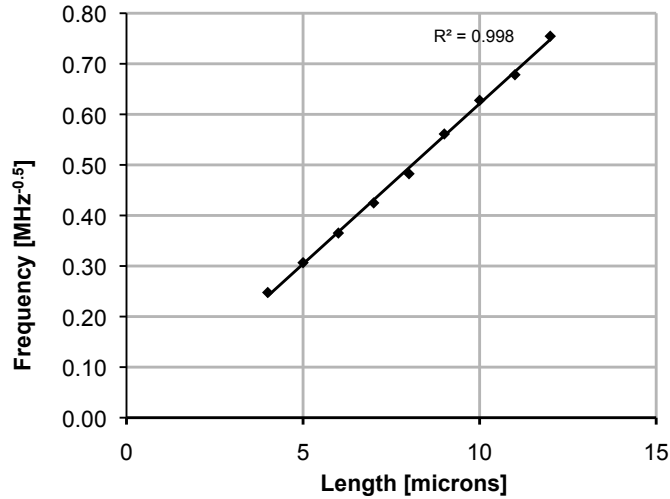


Figure 3.6: Frequency vs cantilever length plot for 400nm wide SOI cantilever beams. Note that error bars corresponding to frequency measurement are vastly smaller than the data point icons.

From the slope of the trendline in figure 3.6 we can determine that the speed of sound in these silicon cantilevers was $7680 \frac{m}{s}$. Given the density of single crystal silicon is well defined ($\rho_{Si} = 2.329 \frac{g}{cm^3}$), the speed of sound can be used to infer the Young's modulus. Table 3.2 is a summary of the mechanical characteristics of the cantilever material inferred from the resonance data.

3.5 Summary

In this chapter, we outlined the development and testing of cantilever beams fabricated out of silicon on insulator wafers. We applied and refined electron beam lithography techniques for the patterning of silicon nanocantilevers. This pattern was then transferred into the device layer of an SOI die using a cryogenic anisotropic reactive ion etch. This is an etch that uses simultaneous passivation and etching mechanisms rather than a gas chopping methodology

Table 3.2: Summary of physical values of SOI material as measured by the resonating cantilever beam method.

Cantilever width	mode	$\sqrt{\frac{E}{\rho}}$	E
nm	unitless	m/s	GPa
400	1	7680	150
400	2	8040	137
800	1	8950	191
800	2	9050	186

(like the Bosch process), enabling the reliable patterning of nanoscale features without significant scalloping. We released single clamped cantilever structures from the sacrificial layer by a buffered HF wet etch and critical point dry. We assayed the resonance frequencies of the cantilever resonators under vacuum in an interferometric resonance testing setup (as described in section 2.7). The correlation between resonance frequency and cantilever length was predicted by the Euler-Bernoulli model with all R^2 values greater than 0.99.

The lithography and release processes demonstrated here were applied in the next chapter to fabricate test structures of Au-Ta alloy for mechanical testing. The sensitivity of a static cantilever sensor is dependent on the stiffness of its constituent material, thus it is imperative to quantify this for our Au-Ta alloys. The resonating beam method will be particularly useful since other methods to test mechanical characteristics such as nanoindentation become increasingly impractical as the film thicknesses are scaled down in the nanometre regime.

CHAPTER 4

Gold Tantalum Material Development

4.1 Introduction

To develop static cantilevers sensors out of an Au-Ta alloy, it is imperative to assay the physical and mechanical properties and determine how to optimize the material properties to suit the sensing goal. This chapter is a record of the synthesis and testing of Au-Ta films and cantilever structures to design a material with superior properties for application as a static cantilever sensor. X-ray diffraction, atomic force microscopy, scanning electron microscopy, nanoindentation and four-point probe contact measurements were performed to characterize the bulk and surface characteristics of the films. The films exhibited an increased elastic modulus and hardness as well as a significant grain size reduction while retaining the face-centered cubic (FCC) structure of pure gold with a very strong $\langle 111 \rangle$ orientation. Additionally, the mechanical characterization of a number of 800 nm wide, 50 nm thick Au-5 at.% (atomic percent) Ta cantilevers was performed using optical interferometry. These devices exhibited resonant frequencies ranging from 371 kHz to 10.9 MHz, with resonant qualities as high as $Q = 640$ at room temperature and over 10000 at 77K. Finite element simulations of these devices were performed and showed good agreement with the experimental observations. A past version of the

work outlined in this chapter has been published in Ref.¹. This work was completed at the University of Alberta Nanofab and electron microscope imaging was performed at the National Institute for Nanotechnology (NINT).

4.2 Metals as a Structural Material for Cantilever Transducers

Silicon based materials (Si, poly-Si, Si₃N₄, SiC) have typically been utilized for the fabrication of MEMS and NEMS cantilevers. These materials are all very light, elastically stiff, and more or less easily synthesized and machined with typical top-down micro and nanofabrication technologies. However, to apply a MEMS or NEMS cantilever as a transducer in a bio or chemical sensor requires the ability to create a selective layer on the cantilever to bind to the target analyte. A popular approach for the functionalization of many types of biosensors is to exploit the affinity of thiolized molecules to gold for the creation of a self-assembled monolayer (SAM). Unfortunately, there is a drawback in coating a resonant cantilever transducer with a metal film. It has been shown that the deposition of metal onto a dynamic NEMS device significantly lowers its resonance quality, thus lowering the sensitivity of the device (109). This can be overcome by localizing the gold functional layer at the tip of the cantilever, but it reduces the functional area for analyte binding (34).

As stated in section 2.5.2 the two greatest factors in maximizing the stress sensitivity of a static cantilever sensor have to do with its dimensions (we wish to minimize thickness and maximize length). Static cantilevers do not undergo a significant loss of sensitivity with small metal coatings, in fact metals have been used to detect chemical reactions through calorimetry by exploiting the

¹A version of this chapter was published in Ref. (186). All fabrication, resonance assaying, simulations, and film stress measurements were conducted by N. Nelson-Fitzpatrick. Electron microscopy was conducted by C. Ophus and N Nelson-Fitzpatrick. X-ray diffraction was conducted by E. Luber and C. Ophus. Nanoindentation was conducted by Z. Lee. Film conductivity measurements conducted by E. Luber. AFM was conducted by L. Gervais and C. Ophus. Additional supervision provided by D. Mitlin.

bimetallic strip effect. Unfortunately, in applications where calorimetry is not the detection method metal layers will be a source of noise in static cantilever sensors made of silicon materials, since they have vastly different coefficients of expansion. In both instances metal coatings on silicon cantilevers are not beneficial to the transduction function of the cantilevers. Since we desire the chemical properties of metals on the surface of our cantilever, why not make the entire cantilever out of a metal film?

Metals have largely been overlooked as a structural material for cantilever sensors for a number of reasons. Sputtered and evaporated metal films tend to suffer from differential stresses which can lead to undesirable device deformation. Metal thin films are also typically polycrystalline and large crystal grains may hinder the machining of the device and the uniformity of its mechanical properties. Despite these downsides there have been a few examples of metal micro and nano cantilever devices with limited stress induced deformation. Chand *et al.* (187) fabricated gold AFM cantilevers with silicon tips and demonstrated their use in imaging. While there was no comment on the impact of polycrystallinity there were significant differential stresses observed in the released cantilevers, which was relieved through the application of rapid thermal annealing. Annealing can however be an undesirable process if one wishes to integrate readout electronics into the cantilever chip.

Ideally, for the fabrication of gold static cantilever structures, we wish to tailor the gold film such that it is uniform (grain size much smaller than device dimension) and exhibits a low deposited stress. A new approach to achieve these two goals has been demonstrated by Lee *et al.* (99) who used magnetron co-sputtering to introduce Mo into Al films, demonstrating control over the film's microstructure and stress state. Lee *et al.* were able to demonstrate the fabrication and release of an 8 μm long 50 nm thick single clamped cantilever without destructive deformation due to stress. The choice of Mo was made by inspection of its binary phase diagram with Al. The presence of large numbers of intermetallic species with no low temperature solubility implied a high negative heat of formation. Considering that film synthesis from vapour

deposition involves extremely high cooling rates, these complex intermetallic phases were not thermodynamically accessible (188). Instead supersaturation of elemental phases and the formation of an amorphous phase was observed at various Mo concentrations. A similar methodology has subsequently been applied to Ni-Mo (101) and Cu-Hf (102) material systems.

A similar approach was pursued for the synthesis Au alloy films with mechanical characteristics suitable for static microcantilever transducers. Tantalum was chosen to complement Au based on the large number of intermetallic compounds in its binary phase diagram (189), which implies a large negative heat of mixing. Indeed, supersaturated FCC Au and amorphous alloy phases have previously been achieved (190) through the ion mixing of alternatively deposited Au and Ta layers, indicating that this co-sputtering approach should be able to achieve similar film microstructures. There are several other alloying additions that form intermetallics with Au, including Ca, Cd, Ce, Dy, Er, Ga, Gd, Hf, Ho, In, La and Nd. Tantalum was specifically chosen as the alloying addition due to its ease of integration with standard micro- and nanofabrication processes. Tantalum is routinely used in clean rooms, is inexpensive, non-toxic and serves as an excellent film adhesion layer, reducing the need of additional processing steps.

4.3 Physical Vapour Deposition and Sputtering

Methods for the deposition of thin films can generally be broken down into two categories, chemical vapour deposition (CVD) and physical vapour deposition (PVD). To ensure the purity of the deposited films, all of these processes take place in reaction chambers that have been evacuated. Chemical vapour deposition synthesizes a thin film on a substrate by means of a chemical reaction of precursor gases directly at the substrate's surface. Physical vapour deposition uses physical excitation to eject material from a source which is allowed

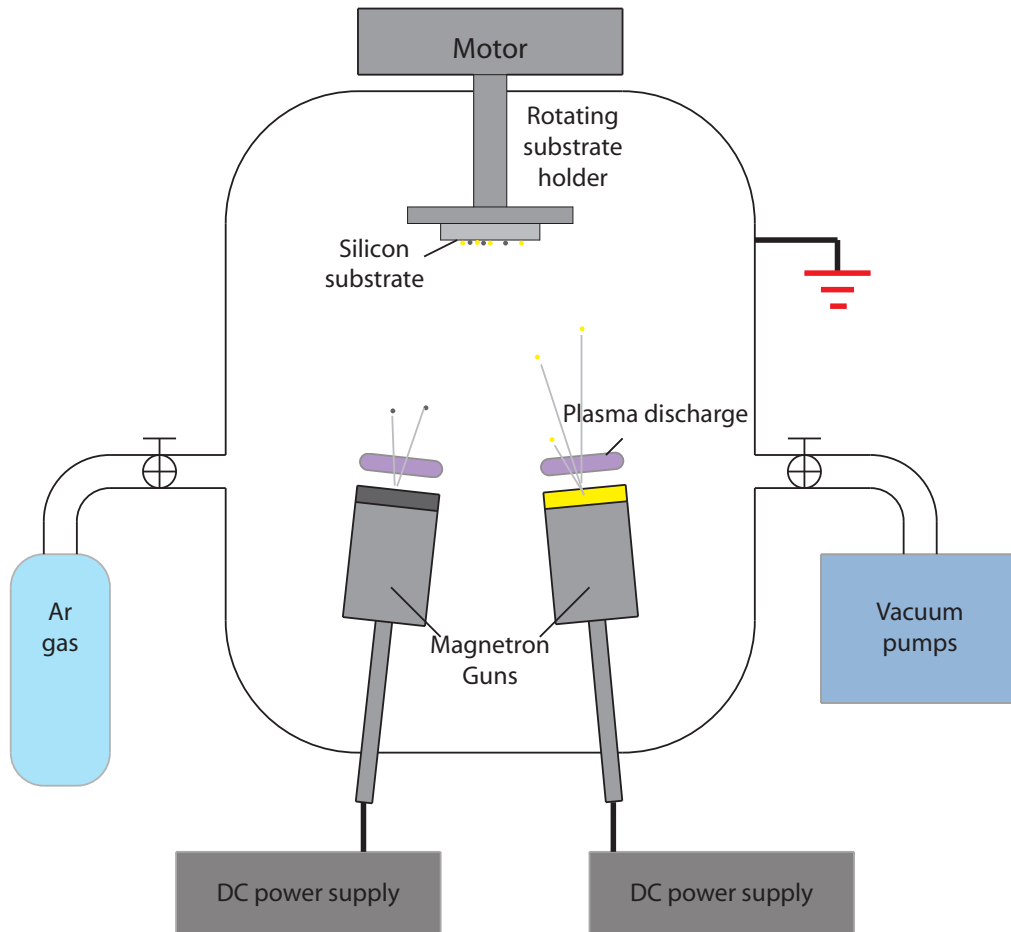


Figure 4.1: Schematic diagram of a magnetron co-sputter system used to deposit Au-Ta alloy films.

to condense on a substrate. The two primary technologies used in physical vapour deposition are evaporation and sputtering.

In evaporation a crucible of material (sometimes called the charge) and the substrate are placed in a high-vacuum chamber (typically evacuated by a diffusion or cryopump). The charge is heated up until it is molten by either a resistance heater or an electron beam increasing its vapour pressure. The increased vapour pressure results in a significant number of charge atoms leaving the crucible. Due to the low pressure in the chamber, these ejected atoms travel in a straight line path until they condense either on the chamber walls or the substrate. This directionality of the evaporant flux can be deleterious as the coating of step heights on the substrate surface can be poor. However, this flux directionality has also been advantageously leveraged for the formation of structured thin films by exploiting self shadowing effects in thin film growth at oblique angles (191). However, for the synthesis of stoichiometrically controlled thin films, evaporation is not typically employed since the deposition rate of evaporant is an extremely sensitive function of the charge temperature.

Sputtering is the primary alternative to evaporation for PVD thin film synthesis, and this is the film synthesis technique applied in chapters 4 and 5. Compared to evaporation, sputtering has much better step coverage and deposition rates are much more controllable. This ability to more accurately control the deposition rate in sputtering makes it a more attractive technology for the formation of thin alloy films. The process of sputtering starts similarly to evaporation, a material source (called the sputter target) and a substrate are placed in a high-vacuum chamber. Once the chamber has been evacuated to the desired base pressure, a noble gas (typically Ar) is introduced into the chamber, typically bringing the pressure into the mTorr range. The target material is located on a powered chuck (called a sputter gun) and an electric field is generated between this chuck (potential in the negative hundreds of volts) and the chamber walls (ground), which causes a plasma discharge to form near the target. Positively charged ions from the plasma are driven towards the target material and collide with it causing a cascade of atomic

collisions in the target, ejecting electrons (which help sustain the plasma) and atoms of the target material. The higher operating pressures of sputtering lead to more conformal coverage of topology on the substrate, since at these higher pressures the ejected atoms will undergo multiple collisions with gases in the chamber before adsorbing on the substrate. The ability to control the number of ion collisions (and thus sputter flux) by modulating the potential of the target makes sputtering much more amenable to alloy deposition than evaporation.

DC sputtering is typically employed for the deposition of metals while insulating materials may require RF or pulsed DC power supplies. For the deposition of thin metal films (like Au and Ta) magnetron DC co-sputtering is typically employed. Magnetrons are commonly incorporated into sputtering systems to confine the electrons in the vicinity of the target, increasing the density of the plasma and thus improving the sputter yield. For the deposition of Au-Ta alloy two magnetron sputter guns were employed simultaneously so that the rates of Au and Ta deposition could be controlled independently to tailor the stoichiometry of the alloy. A schematic of the co-sputtering system is provided in figure 4.1.

4.4 Generalized Method for Sputtering Metal Alloys with Stoichiometric Control

This section outlines a general method for depositing metal alloy thin films with stoichiometric control and it has been applied successfully for other binary alloys like Al-Mo (99) and Ni-Mo (101). In all these cases, the power of one sputter gun was held constant (for a constant deposition rate) while the power of the second gun was varied to control the stoichiometry of the film. Using this method, one can determine the relationship between the power of the varied gun and the stoichiometry of the film.

The first step in depositing an alloy film with stoichiometric control is to

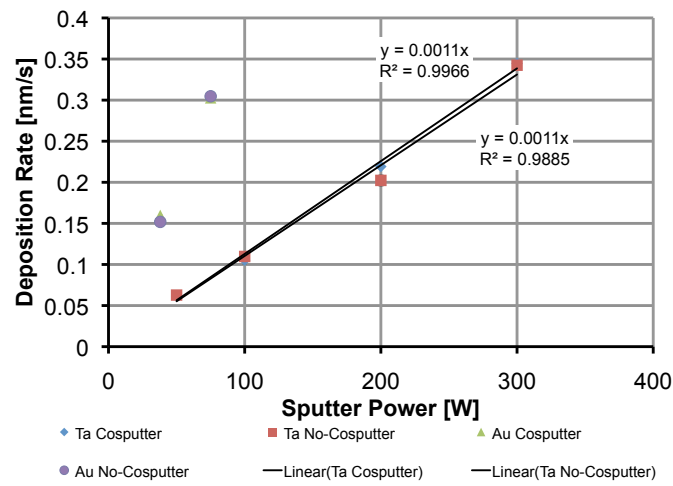


Figure 4.2: Calibration plot of deposition rate versus sputter gun power for Au and Ta used to control for stoichiometry of the film. Note that the introduction of extra electrons in the plasma by co-sputtering causes a minor $\sim 2\%$ variation in Ta deposition rate versus applied power.

characterize the sputter rates of its component films. We describe the film by the atomic percent of one of its constituents, we will call this “element A”. The composition of a co-sputtered film of elements A and B can be approximated by the following equation:

$$\%at.A = \frac{D_A R_A}{D_A R_A + D_B R_B} \quad (4.1)$$

where D_X is the molar density of the element X and R_X is the deposition rate of element X. It is assumed that the deposition rate is proportional to the applied sputter power

$$R_X = M_X P_X \quad (4.2)$$

where P_X is the sputter power of element X and M_X is the constant of proportionality. If the deposition rate of element B is held constant (ie. deposition under the same conditions and power) the required power to achieve the desired stoichiometry of the film can be evaluated by the following equation:

$$P_A = \frac{D_B R_B (\%at.A)}{D_A M_A (1 - \%at.A)} \quad (4.3)$$

To determine the appropriate powers for a desired stoichiometry, the deposition rates of elements A and B must be measured. This is done by marking a clean microscope slide with a felt pen and then depositing our films of varied power on them. The height of the film can then be determined by a stylus profilometer and knowing the deposition time we can relate this height to the deposition rate.

In this work the deposition rate of the Au is held constant and the deposition rate of Ta was varied to achieve the desired stoichiometry. Figure 4.2 is a typical calibration plot of deposition rate versus sputter gun power. It is important to note that running multiple sputter guns simultaneously will increase the number of free electrons in the sputter chamber and that sputter

rate is highly dependant on electron density in the plasma. For this reason, sputter rates were measured for Au and Ta independently, and while both guns were running. In practice very little difference was observed in the sputter rates in these two cases ($\sim 2\%$ difference in Ta deposition rate per watt), this was attributed to the placement of a grounded cross contamination shield between the Au and Ta sputter guns. The cross contamination shield would intercept the vast majority of electrons from one gun, preventing them from affecting the plasma discharge of the complimentary sputter gun.

4.5 Film Characterization

A series of Au-Ta alloy films with compositions ranging from pure Au to pure Ta were synthesized using the DC magnetron co-sputtering of pure Au and pure Ta metal targets. The argon sputtering pressure was kept constant at 7.0 mTorr and the base pressure was 1.0×10^{-6} Torr or lower in all sputtering runs. The films were deposited onto single side polished, 4 inch silicon $\langle 100 \rangle$ wafers that were cleaned in a piranha solution (3:1 mixture of 51% H_2SO_4 and 30% H_2O_2) for 15 min. Sputtering was performed in a sputter-up configuration, with substrate rotation implemented to increase film uniformity. For Au-Ta films containing up to 50 atomic percent (at.%) Ta, the Au sputtering power was kept constant at 75 W, corresponding to a deposition rate of $0.34 \frac{\text{nm}}{\text{s}}$. To achieve the desired stoichiometry, the Ta sputtering power was varied from 0 to 298 W, corresponding to deposition rates of up to $0.36 \frac{\text{nm}}{\text{s}}$. In addition, Au-Ta films with 65 at.% Ta were also synthesized using a 38 W sputtering power for Au, and 277 W for Ta. All films first used a 50 nm thick Ta adhesion layer to insure bonding of the Au-Ta film to the substrate.

4.5.1 X-Ray Diffraction

Figure 4.3 shows a series of XRD curves of Au-Ta alloys with increasing Ta concentrations of up to 65 at.% Ta. All X-ray scans up to 50 at.% Ta display

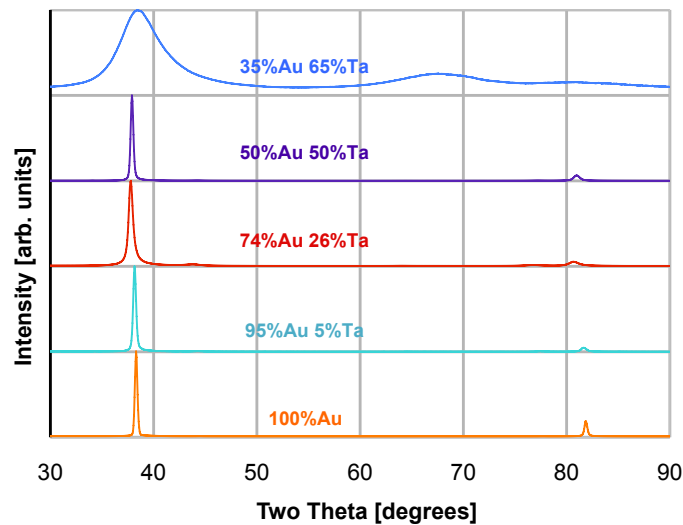


Figure 4.3: X-ray diffraction scans of Au-Ta films of different compositions

an face centred cubic (FCC) diffraction pattern, highly oriented in the $\langle 111 \rangle$ direction. From the lack of any other peaks, we conclude that all of the Ta is in solid solution with the Au for compositions up to 50 at.% Ta. This solubility of at least 50% of Ta in gold is considerably higher than the reported room-temperature equilibrium solubility of $\sim 5\text{-}10$ at.% (189). The enhanced solubility of Ta in Au is a result of the physical vapour deposition process. The sputtered adatoms cool extremely rapidly after impinging upon the surface, and therefore not much energy is available for diffusive processes on the film surface such as nucleation. Since the nucleation barrier to forming the intermetallic compounds Au_2Ta_3 and AuTa_5 is much greater than the barrier to forming a disordered solid solution of Ta in Au, the solid solution phase is expected to dominate. Further discussion on solubility enhancement of sputtered or evaporated thin films can be found in the following book (192). The Au microstructure hence remains supersaturated with Ta. It is also worth noting that this enhanced solubility agrees with the amorphous transition noted by Liu *et al.* at ~ 55 at.% Ta (193). This transition occurs when the free energy

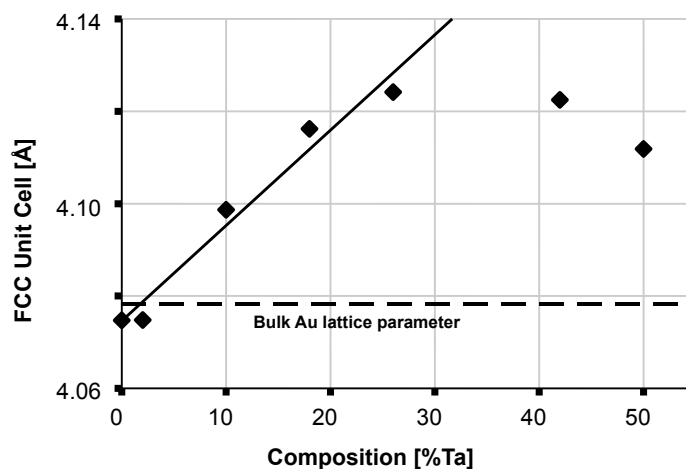


Figure 4.4: Au-Ta lattice parameters calculated from the $\langle 222 \rangle$ XRD peaks, with Vegard's law plotted for the first five points.

of the amorphous phase reaches a value lower than that of the FCC phase (with Ta in solid solution). The 65 at.% Ta diffraction pattern shown in figure 4.3, however, has a much different microstructure. The signal under the diffraction peaks is considerably higher than that of the crystalline samples and the overall scan strongly resembles previously reported amorphous film diffraction patterns like the Zr-30 at.% Pd alloy studied by Murty *et al.* (194). Previous work on the Al-Mo system (99) suggests that the structure of Au-65 at.% Ta is not completely amorphous, but rather a true composite consisting of nanocrystallites embedded in an amorphous matrix.

The peaks of the Au-Ta crystalline diffraction patterns shift as the Ta concentration is increased. From this shift, we calculate the changing lattice parameter of the FCC gold matrix (figure 4.4). Intrinsic film stress could cause such a change in lattice parameter. However, as discussed later, the measured film stresses were all below values of 400 MPa, corresponding to approximately 0.2% shift in lattice parameter in the worst case. Stress as a source of lat-

tice strain is therefore neglected in this study. For compositions of up to 26 at.% Ta, the lattice distortion appears to follow Vegard's law, meaning a linear relationship between lattice spacing and concentration of solute atoms in solid solution. Interestingly, the higher Ta compositions substantially deviate from this linear relationship, with the lattice parameter falling down to near that of pure Au. Vegard's law is indeed an empirical relation nominally observed in mutually soluble FCC systems (195). Completely soluble systems, such as Ni-Cu and Cu-Pd, generally follow this trend, though with some non-linear deviation at high alloy contents. The fact that Au-Ta, an FCC-BCC (body-centered cubic) system, deviates from Vegard's law at high Ta contents is therefore not unusual. Vegard's law is essentially an assumption that the lattice parameter of the alloy system is a rule-of-mixtures sum of the parent atomic radii. The deviation from linearity comes from the fact that the atomic radius of a Ta atom in Au solid solution is not the same as in the parent elemental Ta phase. This should be especially true since Au and Ta have highly negative heats of interaction, as evident by the presence of the intermetallic phases.

4.5.2 Microscopy

We characterized film surfaces using a Digital Instruments Dimension 3100 atomic force microscope (AFM) with Nanosensors BS-Tap300 aluminum coated tapping-mode AFM probes. The scan size was kept constant at $1\ \mu\text{m} \times 1\ \mu\text{m}$. The AFM data were processed using Scanning Probe Image Processor version 4.0.6.0 SPIPTM commercial software to ascertain the root mean square (RMS) roughness of the films. Scanning electron microscope (SEM) imaging was also performed using a Hitachi S-4800 field emission system in order to supplement the AFM imaging results.

From the scanning electron and atomic force micrographs we can see that in the regime below 50% at. Ta, grain size of the Au-Ta films is reduced with the introduction of increased concentrations of Ta. Figure 4.7 is a plot

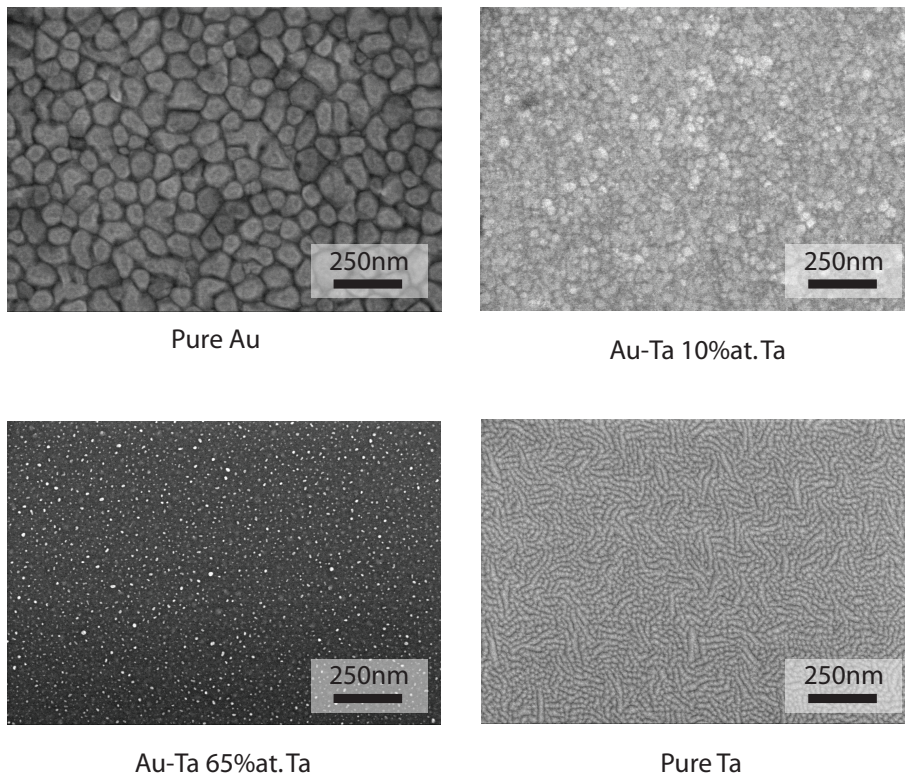
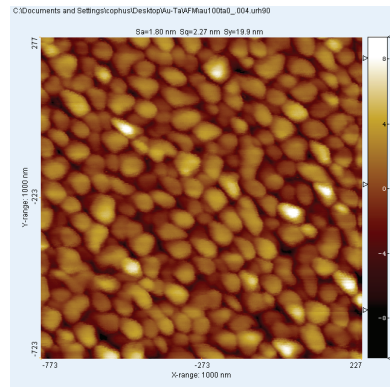
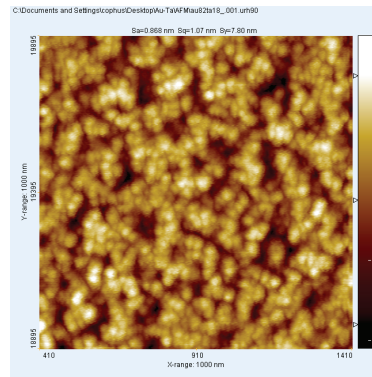


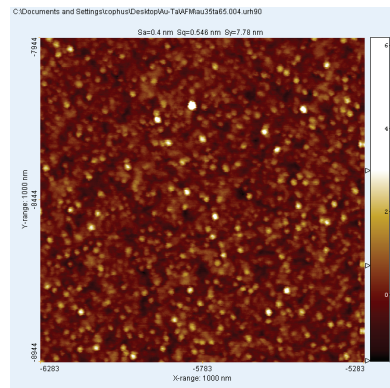
Figure 4.5: Scanning electron micrographs of various Au-Ta concentrations



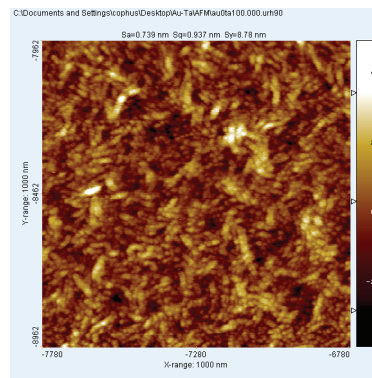
Pure Au



Au-Ta 18%at.Ta



Au-Ta 65%at.Ta



Pure Ta

Figure 4.6: Atomic force micrographs of various Au-Ta concentrations

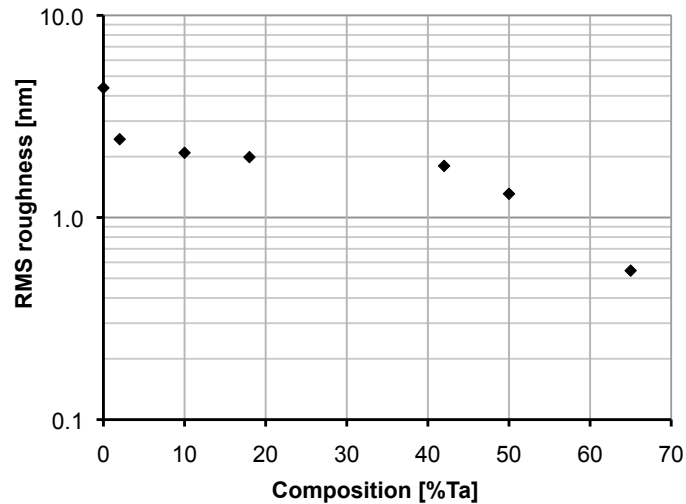


Figure 4.7: Film roughness versus Au-Ta composition

of the corresponding RMS surface roughnesses, as measured in the AFM. A significant decrease in surface roughness is observed, as we would expect for a PVD deposited film given the grain size reduction observed in the SEM and AFM images. The reduction of thin film grain size by alloying is a well-known effect (196). As noted above, surface diffusion is already reduced due to the rapid cooling of sputtered adatoms. In addition, Au and Ta have a strong negative heat of mixing (189). Therefore Au-Ta bonds are stronger than either Au-Au or Ta-Ta bonds. As a consequence, Ta lowers the surface diffusivity of Au and vice versa, leading to reduced grain sizes. For a similar reason, Ta would also reduce the size of the Au islands found during the initial stages of film growth. Given a constant impinging atomic flux, this would lead to a higher surviving island number density, and in turn refine the grain size throughout the film thickness.

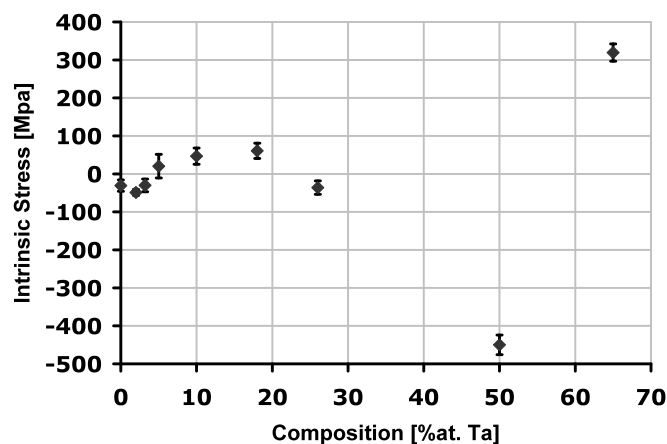


Figure 4.8: Au-Ta film stress vs. Ta content for a 400nm film. Error bars correspond to the standard deviation of six separate wafer bowing measurements 30° apart.

4.5.3 Film Stress

Stress observed in PVD and CVD thin films can be caused by a plethora of sources (thermal mismatch, doping, lattice mismatch.etc...). When making nanomechanical cantilevers, we wish to use a material with low stress (for making single clamped cantilevers) or a material undergoing tensile stress (for making doubly clamped beams), to ensure that our released devices do not undergo any significant deformation. A Flexus 2320 thin film stress measurement system was employed to determine the stress state of our deposited films. This system uses a laser interferometer to map the curvature of a silicon substrate before and after a film is deposited. The difference in curvature can then be related to the stress of the film using Stoney's equation (section 2.5.1), if we know the thickness of our film and Si substrate. Alternative methods to measure stress include the cantilever method, whereby the deflection of a cantilever due to stress is monitored and related back to the film stress (section

2.5.2). A plot of Au-Ta film stress for a 400 nm thick film is provided in Figure 4.8. The residual stress undergoes several passages from compressive to tensile as the Ta concentration is increased from 0 to 65 at. %. With these results it was concluded that the region around the 5% at. Ta concentration would be suitable for a single clamped cantilever due to the near-zero residual stress observed at this concentration.

4.5.4 Film Resistivity

Four-point probe measurements were also conducted on the films to determine the changes in conductivity resulting from additional Ta (figure 4.9). As expected, the conductivity decreased considerably as the Ta concentration increased. This result is again similar to the results obtained in previous work on aluminum-molybdenum nanocomposite films (99). The overall observed reduction in conductivity can be attributed to a number of microstructural changes, such as increasing grain boundary density and microstrains in the lattice induced by increasing Ta in solid solution. We also noted that the conductivity data is highly nonlinear. As shown by Bhatia and Thornton (197), the resistivity of a binary alloy that exhibits ideal mixing can actually be expressed using Nordheim's rule:

$$\rho = Kc(1 - c) \quad (4.4)$$

where c is the mole fraction of tantalum, and K is a proportionality constant. A best fit curve of Nordheim's rule is superimposed in figure 4.9. Nordheim's rule is observed in the range Au-0 at.% Ta to Au-20 at.% Ta. Since the equilibrium phase diagram of Au-Ta (189) shows several intermetallics, we expect that at sufficiently high concentration of tantalum, Au-Ta will exhibit non-ideal mixing. Beyond the addition of 20 at.% Ta, we observe slight deviations from Nordheim's rule, as the mixing is no longer ideal and the description of electron scattering in the material becomes more complex.

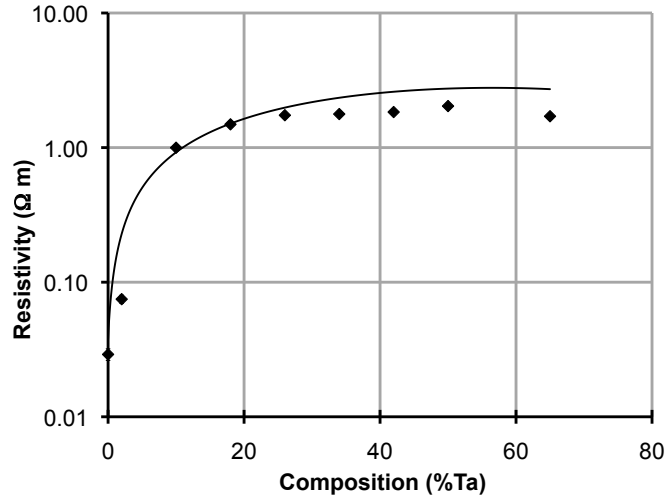


Figure 4.9: A semi-logarithmic plot of Au-Ta electrical resistivity as a function of Ta content. A best fit to Nordheim's rule is superimposed onto the datapoints.

4.5.5 Nanoindentation

Nanoindentation was performed on the unprocessed films prior to nanomachining in order to assess the reduced modulus and hardness over the range of Au-Ta alloys we synthesized. These measurements were performed with a Hysitron triboindenter using a Berkovich indenter tip at an applied load of $500 \mu\text{N}$. Each graphed measurement is composed of 25 averaged measurements with individual indentations separated from each other by approximately $25 \mu\text{m}$. The hardness and reduced modulus were determined from the unloading portion of the load-depth curve using the method outlined by Oliver and Pharr (198). The reduced modulus was then converted to the elastic modulus of the alloy by compensating for tip deformation through the following equation.

$$\frac{1}{E_r} = \frac{1 - \nu^2}{E} + \frac{1 - \nu_i^2}{E_i} \quad (4.5)$$

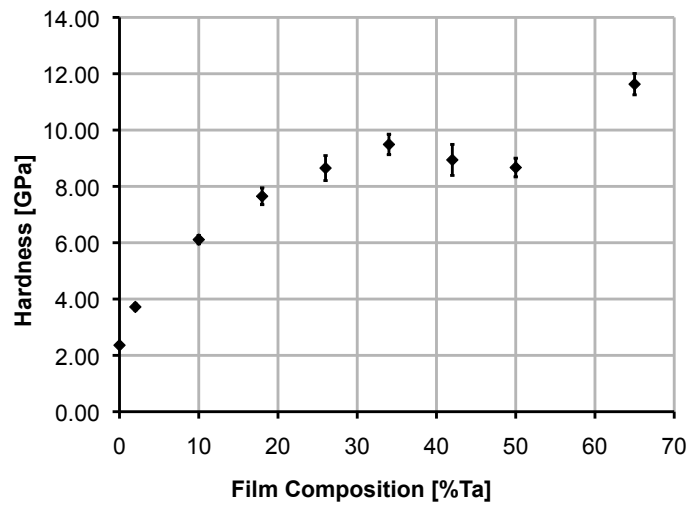


Figure 4.10: Graph of nanoindentation hardness versus Ta concentration for a series of Au-Ta films, as measured by nanoindentation. The error bars in this graph were obtained by the standard deviation of 25 separate indentation tests performed on each composition film.

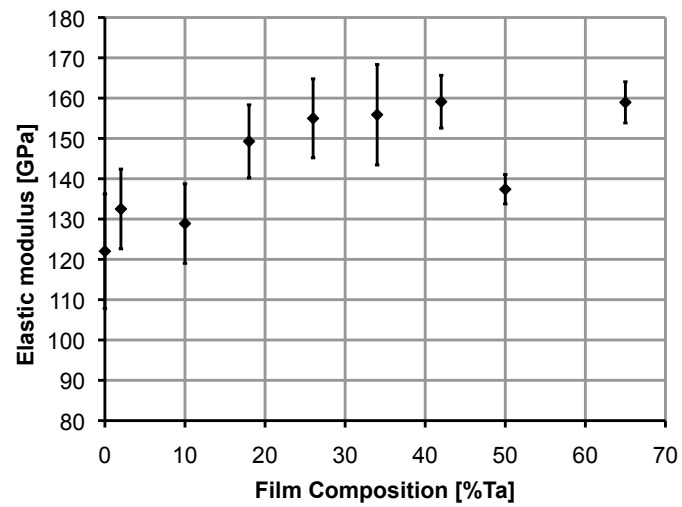


Figure 4.11: Graph of elastic modulus versus Ta concentration for a series of Au-Ta films, as measured by nanoindentation. The error bars in this graph were obtained by the standard deviation of 25 separate indentation tests performed on each composition film.

where E_r is the reduced modulus, E is the Young's modulus and ν is the Poisson's ratio of the film material, and E_i and ν_i are the Young's modulus and Poisson's ratio for the indenter material.

Figure 4.10 shows a dramatic increase of hardness with increasing Ta concentration. More specifically, the hardness of the Au-65 at.% Ta film was five times greater than that of the pure Au film. This hardness increase could be attributed to several effects, including grain size reduction (199; 200), solid solution hardening (201), the higher intrinsic hardness of tantalum (200), and the previously mentioned phase change at tantalum concentrations higher than 50 at.%. Since figure 4.7 shows very little change in the roughness (implying little change in grain size) of Au-Ta beyond 2 at.% Ta, the increase in hardness is attributed primarily to solid solution strengthening. Solutes in gold have been shown to greatly increase hardness (201), and in our sputtered films we have higher solute concentrations than can exist in equilibrium Au-Ta. Because the Au-65 at.% Ta film is amorphous, it should exhibit a significantly higher hardness than the crystalline film compositions since no plasticity via dislocation motion would be possible. Figure 4.11 shows the increase of the elastic modulus with the composition of the films. We can see that there is a modest increase in the Young's modulus of the films in the low and mid Ta concentrations. This increasing stiffness is rather small and should have little impact on the application of Au-Ta films as static cantilever sensors.

4.6 Fabrication of Cantilevers

With all of our surface and bulk material testing completed, the 5 at.% Ta concentration was chosen as the most promising alloy for cantilever fabrication, due to its near-zero intrinsic stress and refined grain structure. Cantilever resonators were therefore fabricated out of Au-Ta nanocomposite (5 at.% Ta). A process flow of the fabrication procedure is provided in figure 4.12. The devices had widths of 400 or 800 nm, and lengths ranging from 1 to 8 μm . Fabrication was conducted using silicon $\langle 100 \rangle$ wafers onto which 400 nm

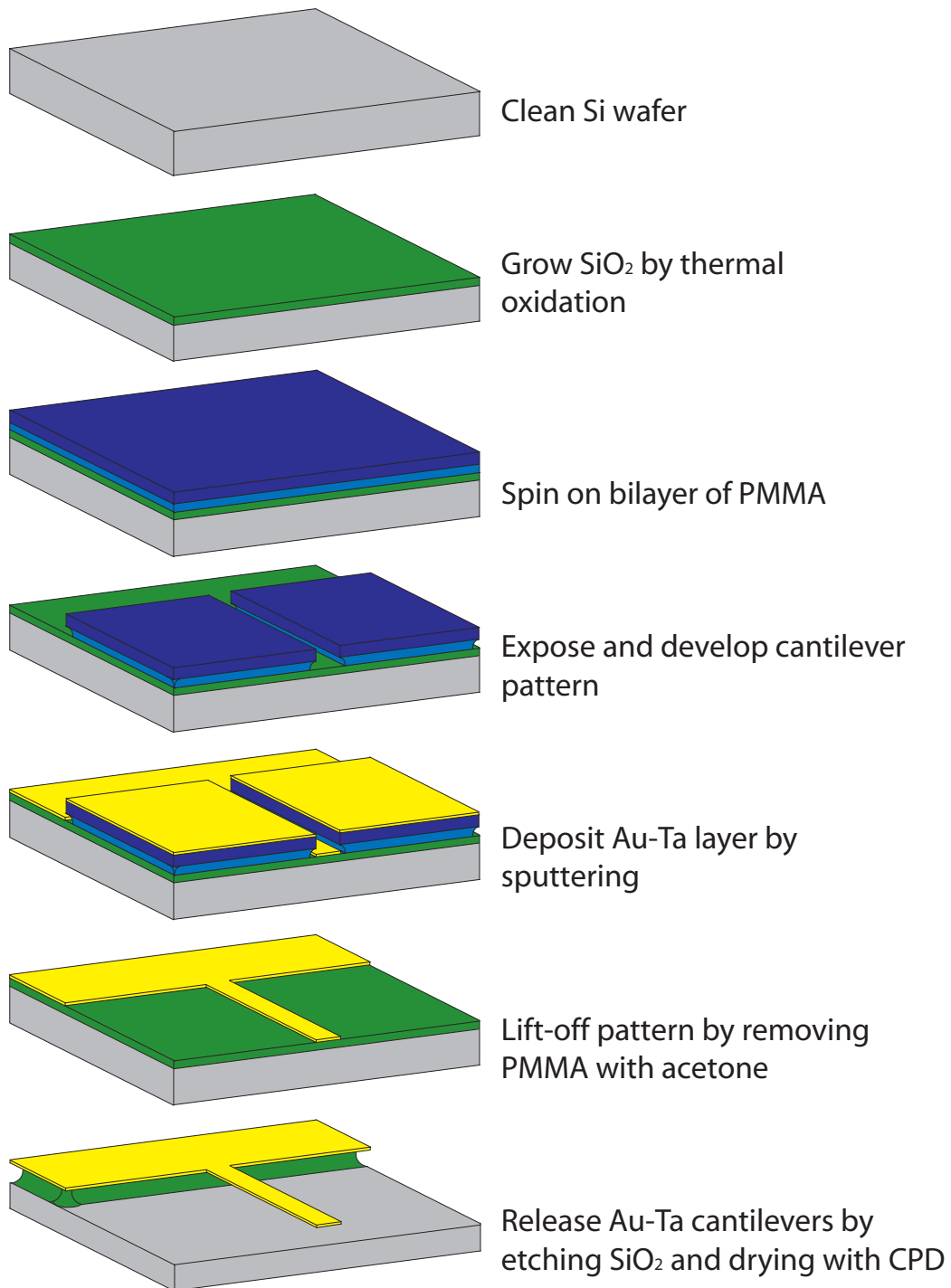


Figure 4.12: Process flow illustration for the fabrication of resonant Au-Ta nanocantilevers.

of thermal oxide was grown. A resist bilayer consisting of 60 nm of 495K polymethylmethacrylate (PMMA), followed by 60 nm of 950K PMMA was first coated onto the thermal oxide, and patterned in a Raith150 electron beam lithography system using a 10 kV accelerating voltage and a 10 μm aperture. The exposed resist was developed in a methylisobutylketone solution (1 methylisobutylketone:3 isopropyl alcohol). The die was then mounted into the sputter system for deposition of a 1 nm Ta adhesion layer and a 50 nm thick Au-Ta device layer. After deposition, the die was immersed in a bath of acetone to lift off the unexposed PMMA, thus leaving a pattern of Au-Ta where the resist was exposed. Usage of a resist bilayer enabled the formation of an undercut in the developed resist profile, allowing a discontinuity of the deposited metal layer at the sidewalls of the resist, and resulting in a relatively clean lift-off of the metal. This being said, the devices still did exhibit some roughness at their edges due to the finite deposition of metal onto the resist sidewalls. The underlying thermal oxide was then etched away using a solution of buffered hydrofluoric acid (1 HF:10NH₄F), and the die was immediately placed in a critical point dryer to prevent stiction. Figure 4.12 shows an SEM micrograph of a typical resulting cantilever.

4.7 Resonance Data

Resonance testing of the cantilevers was performed using an interferometric method (as outlined in section 2.7.1) initially developed for the characterization of Si NEMS resonators (108). The die is mounted on a piezoelectric element that is contained within a small vacuum chamber pumped down to the 10^{-3} Torr range. The piezoelement is actuated by the tracking output of a spectrum analyzer (Agilent model 4401B). A He-Ne gas laser (JDS Uniphase model 1144, $\lambda = 633$ nm) beam is directed through a beamsplitter and focused onto the cantilever beam using a 0.35 NA microscope objective. When excited at the resonant frequency, motion of the cantilever relative to the substrate creates a moving fringe pattern that is reflected back through the microscope

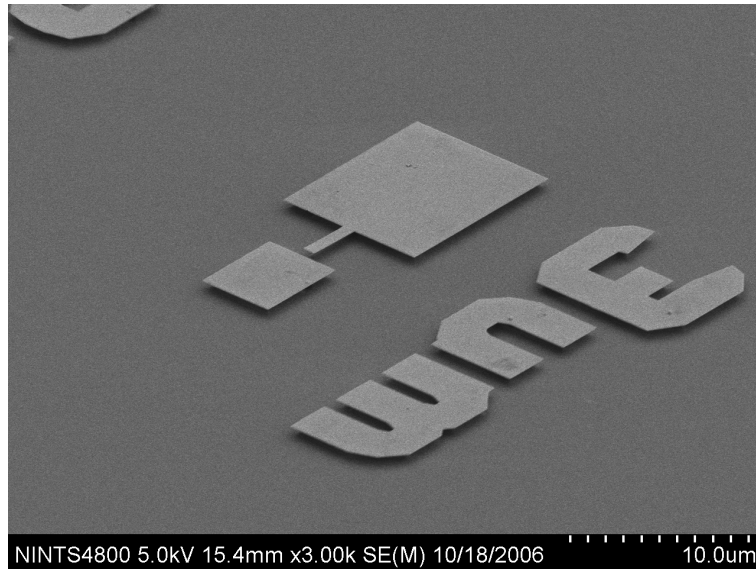


Figure 4.13: Scanning electron micrograph of an Au-Ta nanocantilever with dimensions $w = 800$ nm, $t = 51$ nm, $l = 3$ μm .

objective and reflected off the beamsplitter, impinging on an AC coupled photodetector (New Focus model 1601). The photodetector output is connected to the input of the spectrum analyzer.

4.7.1 Room Temperature

Figure 4.14 shows the typical resonant response of a Au-5 at.% Ta cantilever with a length $L = 5$ μm , width $w = 800$ nm and thickness $t = 51$ nm. The resonant frequency of that device is $f = 708$ kHz, and it possesses a resonant quality of $Q = 640$. Resonance qualities of the other devices from this series varied from $Q = 304$ to 640 (table 4.1). No distinct trend of resonant quality is observed as a function of device dimension. The absence of a Q -length relationship suggests that clamping losses are not the dominant loss mechanism in our devices (136). Our observed Q factors overlap with the range of Q observed by Sekaric *et al.* (109) in metallized SiN cantilevers. The resonant quality of a $L = 5$ μm cantilever (from table 4.1) was also studied as a function

Table 4.1: Resonant frequencies and quality factors of a series of Au-Ta 5% at. Ta cantilevers with width $w = 800$ nm and thickness $t = 51$ nm.

Cantilever length μm	Frequency MHz	Q unitless
1	10.9	327
2	3.67	474
3	1.82	383
4	1.06	304
5	0.708	640
7	0.371	424
8	0.285	540

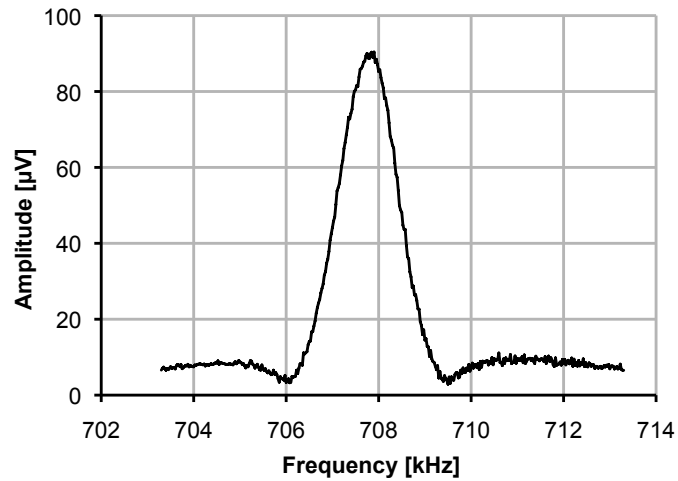


Figure 4.14: Resonant response of an Au-Ta 5 at. % Ta cantilever with a length $L = 5$ μm , width $w = 800$ nm and thickness $t = 51$ nm.

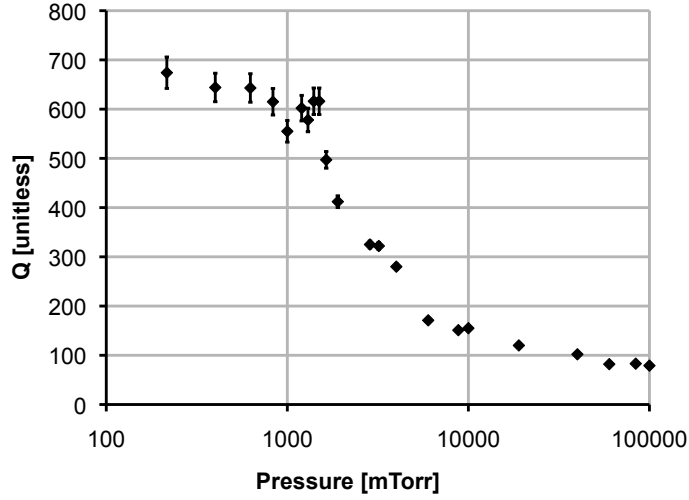


Figure 4.15: Resonance quality Q as a function of pressure for a Au-Ta 5% at. Ta cantilever with dimensions $L = 5\mu\text{m}$, $w = 800\text{ nm}$, $t = 51\text{ nm}$, and a resonant frequency of 708 kHz.

of ambient pressure (figure 4.15). The value of Q of the cantilever did not change significantly as the pressure was varied over the range of 200 mTorr to 1 Torr. However, squeezed film damping became more significant at higher pressures, resulting in a distinct drop of the quality factor.

By using a least squares fit of the cantilever's frequency to its length we may extract the speed of sound $\sqrt{\frac{E}{\rho}}$ in the cantilever material. Figure 4.16 is a plot of the fundamental resonance frequency (to the power -0.5) versus cantilever length of a series of 800 nm wide Au-Ta 5% cantilever beams. Note please that error bars are omitted on this graph since they would be dwarfed by the actual datapoint icons. A detailed determination of $\sqrt{\frac{E}{\rho}}$ from this data is provided in appendix D.

From the slope of the trendline in figure 4.16, we applied equation 3.1 and determined that the speed of sound in these Au-Ta 5% cantilevers was $2493.64 \pm 132.19 \frac{\text{m}}{\text{s}}$. This compares favourably to the speed of sound in gold of $\sqrt{\frac{E}{\rho}} =$

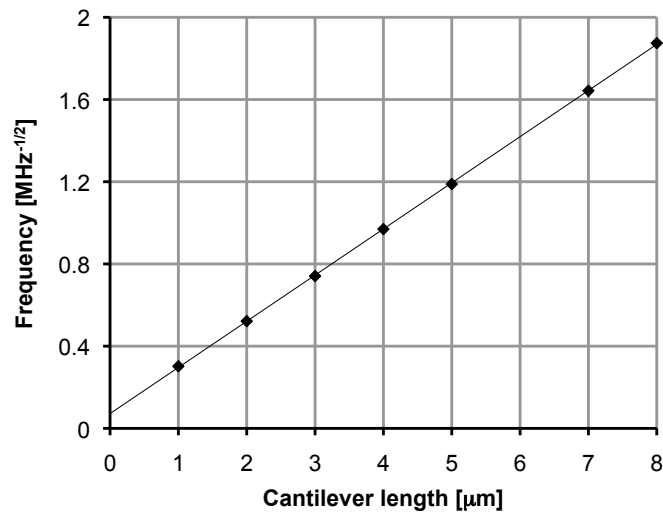


Figure 4.16: Linearized graph of resonance frequency versus length for a series of cantilevers Au-Ta 5% at. Ta with dimensions $w = 800$ nm and $t = 51$ nm. The fit of data to equation 3.1 provides a speed of sound ($\sqrt{\frac{E}{\rho}}$) of $2493.64 \pm 132.19 \frac{m}{s}$

2010 $\frac{m}{s}$ (given a density of $\rho = 19.3 \frac{g}{cm^3}$ and Young's modulus of $E = 78$ GPa for gold). A linear interpolation (rule of mixtures) derived speed of sound for Au-Ta 5% would be 2086 $\frac{m}{s}$ (given a density of $\rho = 16.69 \frac{g}{cm^3}$ and Young's modulus of $E = 186$ GPa for tantalum). Both these values for speed of sound are lower than the speed of sound measured for our Au-Ta 5% cantilevers, but this result should be expected given that the density of a sputtered film is expected to be significantly lower than the bulk density of the material.

4.7.2 Cryogenic

It is well known that resonant loss mechanisms such as phonon-phonon scattering, phonon-electron scattering and thermoelastic damping can be subdued by the cooling of a cantilever resonator. To probe these intrinsic damping mechanisms an Au-Ta cantilever die was mounted on the cold finger of a vacuum cryostat and cooled with LN₂ to 77 K. The resonance peak of a 3 μ m long, 800 nm wide 51 nm thick Au-Ta cantilever was tracked and correlated to cold finger temperature. Figure 4.17 is a plot of cantilever Q versus substrate temperature. Since we are measuring the change in Q for single clamped cantilevers, we can be confident that changes in Q will not be affected by increased tension in the cantilever beam induced by different coefficients of expansion between substrate / sacrificial material and cantilever material.

We can see that there is no internal friction peak as observed in temperature dependance of silicon nanocantilevers (126), rather the Q factor decreases consistently with temperature. A Q factor of over 10^5 was achieved by cooling the cantilever beams to 77 K, which is higher than any value known in literature for single clamped metal nanocantilevers. As ultimate sensitivity in resonant cantilever transducers was not the goal of this work, investigation of temperature effects on quality factor was therefore limited to this single measurement.

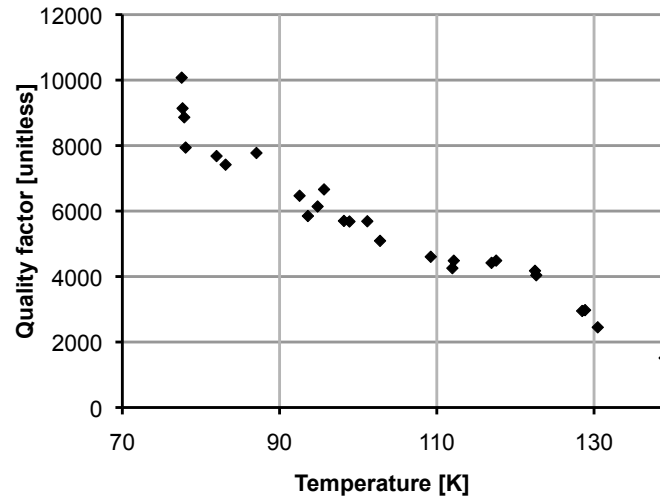


Figure 4.17: Measured quality factor versus substrate holder temperature for a $3\mu\text{m}$ long, 800 nm wide, 51 nm thick Au-Ta cantilever.

4.8 Finite Element Modelling

Lastly, finite element modelling was performed to corroborate the measured eigenfrequencies and the speed of sound extracted from this data and equation 3.1. Two cantilever models for each cantilever geometry ($1 - 8\ \mu\text{m}$ length, 800 nm width, 51 nm device / adhesion layer) were built in COMSOL Multiphysics 3.5a. The models were defined in three dimensions using the MEMS module, structural mechanics, solid stress-strain analysis toolkit. The cantilever models included a $10\ \mu\text{m}$ wide, 400 nm deep “clamping point” that is rigidly fixed at one end and connected to the cantilever at the other to simulate the undercut from the BOE release of the Au-Ta cantilevers. The boundary conditions for all faces of the structure were free, except for the fixed condition imposed on face at the “clamping point”. An illustration of the cantilever geometries constructed in COMSOL is provided in figure 4.18. The two cantilever models were designed as unimorphs, that is there was no material property distinction

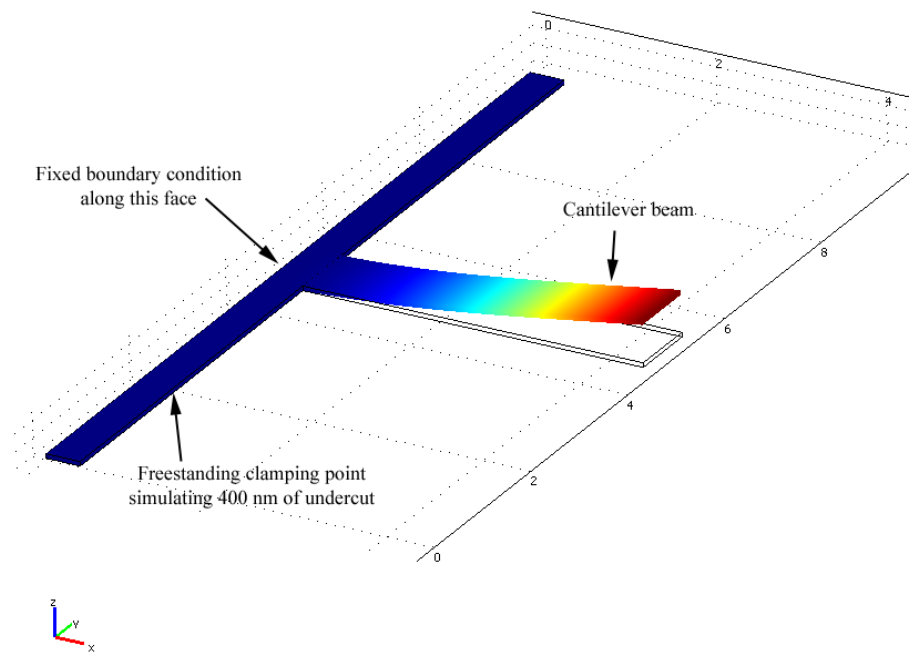


Figure 4.18: Illustration of the cantilever geometry constructed in COMSOL 3.5a for finite element simulations of resonance frequency.

between the adhesion layer and the mechanical layer. The decision to build a unimorph model was undertaken due to machine limitations in meshing and solving for the eigenfrequencies of structures with extremely thin adhesion layers in COMSOL.

The mechanical properties for the two unimorph cantilever structures differed in terms of Young's modulus. One model was termed the "nanoindentation model", deriving its Young's modulus from volumetric interpolation of nanoindentation derived Young's moduli of Au-Ta 5% and pure Ta. The second model was termed the "bulk model" deriving its Young's modulus from a volumetric interpolation of reference values for the Young's moduli of Au-Ta 5% (itself

Table 4.2: Summary of the mechanical properties used in COMSOL finite element modelling of eigenfrequencies of Au-Ta 5% cantilever resonators.

Cantilever model label	Young's modulus GPa	density $\frac{Kg}{m^3}$	Poisson's ratio unitless
nanoindent model	132.1	19121	0.433
bulk model	85.4	19121	0.433

interpolated from interpolation from pure Au and pure Ta) and pure Ta. Poisson's ratios and densities were similarly derived from reference values for both models. A summary of the physical values input into the COMSOL models is provided in table 4.2.

A test was performed to determine the mesh sensitivity of the cantilever structures to confirm that simulations were performed with a mesh density sufficient for accurate computation. COMSOL's adaptive meshing tool (tetragonal meshing elements) was used at eight different mesh density levels to determine the first eigenfrequency of a 1 μm and 8 μm cantilever. As the meshing density was increased from coarse to fine we see the eigenfrequency result converge to a value at which increased mesh density has little impact on the computed result. A plot of fundamental resonance frequency versus number of mesh elements is provided in figure 4.19, confirming mesh insensitivity at higher meshing densities. All subsequent simulations were run with mesh settings at the "extremely fine" setting (the highest setting available), ensuring mesh insensitivity.

With mechanical properties, geometry, model-type, and meshing density appropriately chosen the simulations were run for all cantilever geometries, generating the fundamental resonance frequency for each cantilever model. These resonance frequencies are plotted in figure 4.20. The values generated in COMSOL were then used to extract the speed of sound of the material as was done for the measured cantilever data. The results are summarized in table 4.3.

The results of COMSOL modelling show that a simple rule of mixtures assump-

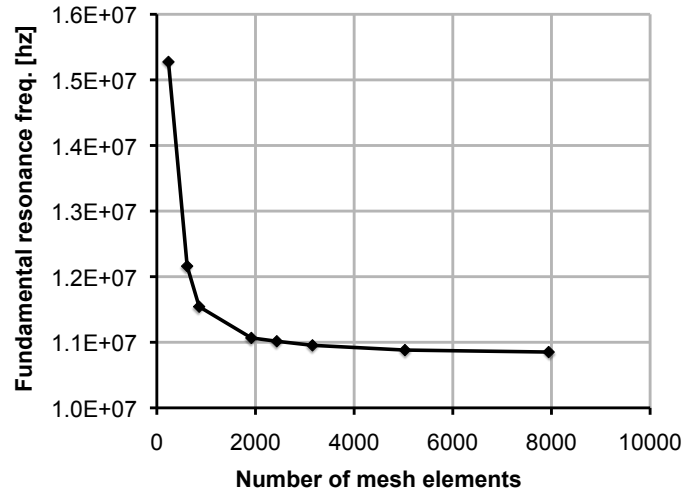


Figure 4.19: Fundamental resonance frequency vs number of mesh elements for a $1\mu\text{m}$ long 800 nm wide Au-Ta cantilever.

Table 4.3: Summary of the speed of sound of COMSOL cantilever models and comparison to measured values

Cantilever model label	Speed of sound $\frac{m}{s}$	difference %
nanoindent model	2646	6%
bulk model	2127	-15%
measured values	2493	N/A

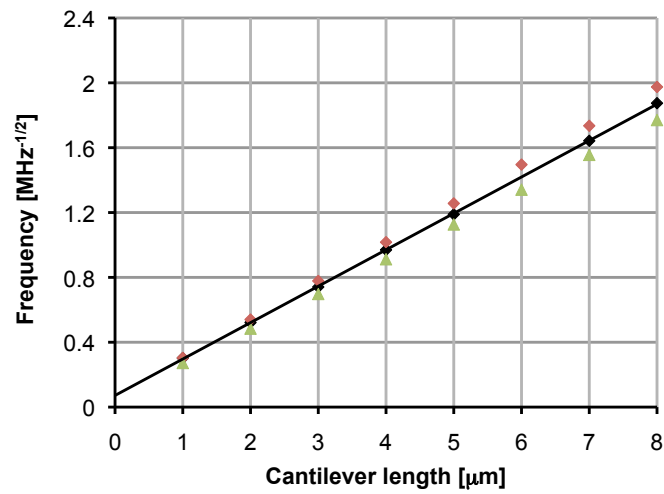


Figure 4.20: Fundamental resonance frequency vs cantilever length for measured cantilevers (black lozenges) and COMSOL modeled cantilevers using a reference value for Young's modulus (red squares) and a nanoindentation derived for Young's modulus (green triangles).

tion of mechanical properties of Au-Ta underestimates the speed of sound in the material, while the nanoindentation derived mechanical properties lead to an overestimation. The fact that we are not compensating for the reduced density of a sputtered film should lead these models to underestimate the speed of sound as compared to the cantilever measurements. This leads us to conclude that the nanoindentation measurements are overstating the Young's modulus, but without a measurement of sputtered film density we can not quantify this value. Overall, the COMSOL models do provide resonance frequencies and speeds of sound that are reasonably close to the experimentally measured frequencies and the speed of sound.

4.9 Summary

We synthesized a novel gold-tantalum nanocomposite alloy material for static microcantilever applications using a co-sputtering approach. We envision the possibility of simplified static cantilever based biological and chemical sensors, given the affinity of gold films for thiolized SAMs. Nanoindentation, XRD, AFM, SEM, and a four-point probe were used to measure the bulk and surface characteristics of the films. The XRD data indicated that below 50 at.% Ta the FCC structure of gold is retained with a very strong $\langle 111 \rangle$ orientation, indicating that these films should still have an affinity for thiolized molecules. The films exhibited an increased elastic modulus and hardness as well as a significant grain size reduction with the introduction of tantalum. All these improvements make this material more suitable than pure gold as a structural material for micro and nanocantilever applications. Indeed, the application of tantalum as an adhesion layer during sputter deposition will enable the cantilever's underside to be intrinsically inert to thiolized molecules, greatly simplifying the application of Au-Ta as a static cantilever material. Mechanical characterization of a number of Au-5 at.% Ta cantilevers was performed with an interferometric resonance measurement setup. The measurements indicated a speed of sound for the Au-5 at.% Ta of $2493.64 \pm 132.19 \frac{m}{s}$. The observed Q

factors of the resonators ranged from 304 to 640 at room temperature, and up to 10000 when cooled to 77 K. Finite element analysis was also performed and corroborated the resonance frequencies measured and speed of sound extracted through application of the Euler-Bernoulli PDE.

CHAPTER 5

Gold Tantalum Static Cantilevers: Proof of Concept and Surface Chemistry

5.1 Introduction

In this chapter¹ we describe the chemical affinity of Au-Ta alloys to alkanethiol molecules and the fabrication of static cantilevers out of Au-Ta 5% alloy. Previous X-ray diffraction analysis showed that from 0-50% at. Ta, the films retain golds FCC structure and $\langle 111 \rangle$ orientation necessary for the formation of an alkanethiol self-assembled monolayer. First the chemical affinity of a series of Au-Ta compositions to alkanethiols was explored. Attachment of dodecanethiol molecules from vapor phase onto the surface of our Au-Ta films was quantified using contact angle measurements and X-ray photoelectron spectroscopy. The presence of alkanethiols was also confirmed by FTIR. As suggested by the X-ray diffraction results, the incorporation of small amounts of tantalum (5% and 10% at. Ta films) had little adverse effect on the attachment of dodecanethiol. However, this ceased to be the case at 20% at. Ta

¹All work in this chapter was performed by N. Nelson-Fitzpatrick except for XPS and FTIR measurements. XPS data was taken by Alberta Centre for Surface Engineering and Sciences (ACSES) technicians and analyzed by N. Nelson-Fitzpatrick. FTIR measurements were taken by D. Rider and N. Nelson-Fitzpatrick, subsequent analysis was performed solely by N. Nelson-Fitzpatrick

and above. Commercially available static microcantilevers were then coated with Au-Ta films and the stress induced by the attachment of dodecanethiol was measured by monitoring cantilever bending with white light interferometry before and after adsorption. A compressive stress of $\sim 1 \frac{N}{m}$ was induced on the silicon cantilever coated with pure Au, as expected from previous reports (82; 83; 85). Induced stress was progressively reduced as Ta content was increased in the Au-Ta films, until no significant deflection was recorded in the case of 20% at. Ta and above compositions, confirming the contact angle and XPS results. Static microcantilevers were then fabricated directly out of a 5% Au-Ta alloy by patterning the sputtered Au-Ta layer onto a silicon wafer with contact photolithography and releasing the cantilever with an SF₆ reactive ion etch. Cantilever dimensions were 140 μm long, 20 μm wide, and 369 nm thick with a theoretical spring constant of 10.5 $\frac{mN}{m}$. The detection of chemisorbed dodecanethiol molecules was successfully demonstrated with these structures through the monitoring of static deflections.

5.2 Background

Static microcantilever devices have been the focus of considerable interest as biological and chemical sensors (82; 43; 97; 96; 202; 203; 83; 204; 89; 205; 172; 85; 98; 206). These devices operate by integrating physically or chemically dissimilar surfaces at their top and bottom. Selective attachment of the target onto one of the surfaces leads to a stress difference between the two sides, resulting in a static deflection of the device. This deflection can in turn be detected by numerous approaches such as piezoresistive sensors (207; 85; 208), split photodiode (82; 83) or interferometry, all outlined in section 2.7.1.

Materials with relatively low Young's modulus that can be machined into structures with high length-to-thickness ratios are desirable in order to optimize their deflection response. Other important considerations also include inherent response to the target analyte, process compatibility, residual stress issues, as well as amenability to effective detection of these deflections. While

silicon has been traditionally used for such machining, this material is not particularly soft compared to other materials such as polymers and metals. To that end, Calleja *et al.* (203) first reported on the fabrication of polymeric microcantilevers optimized for chemical sensing. Polymers indeed offer the advantages of being relatively inexpensive and having an extremely low Young's modulus compared to silicon. This seminal work demonstrated the production of cantilever of lengths ranging from 100 μm to 200 μm and thicknesses ranging 1.5 μm to 1.7 μm , corresponding to spring constant of 15 $\frac{\text{mN}}{\text{m}}$, which compares favorably to current commercially available silicon cantilevers (30 $\frac{\text{mN}}{\text{m}}$ for Concentris CLA-500-010-08). Recent advances in SU-8 process control lead to improved cantilevers with dimensions of 500 μm in length, 100 μm in width, and 2 μm in thickness, corresponding to a spring constant of 4.8 $\frac{\text{mN}}{\text{m}}$ (209). Chand *et al.* (187) explored the fabrication of cantilevers out of sputtered Au. These cantilevers were 160 nm thick and 17 μm long, corresponding to a spring constant of 0.2 $\frac{\text{N}}{\text{m}}$. Unfortunately, these metal cantilevers suffered from significant residual stress and required high temperature annealing to achieve a usable device.

This thesis proposes the use of co-sputtered metal nanocomposite alloys for the fabrication of ultra-thin and thus highly compliant metal cantilevers. As outlined in chapter 4, these nanocomposites offer grain size as low as a few nanometers as well as a low residual stress (186). These alloys offer the possibility of an extremely stress sensitive device due to the relatively low Young's modulus of Au and the thinness of the Au nanocomposite alloy layer that can be successfully released. The stoichiometry of the Au-Ta film was controlled by independently varying the power of the DC magnetron guns to control the deposition rate of Au and Ta. Using this technique, we were able to deposit layers of Au-Ta that retained $\langle 111 \rangle$ FCC structure of gold, necessary for retaining the ability to form alkanethiol self-assembled monolayers (7; 210; 211; 212), while exhibiting a negligible residual stress. As will now be shown in this chapter, such materials also offer intrinsic tunability of their affinity to the target chemisorbed species through control of their atomic composition. This would allow the design and fabrication of ultra-thin structures whose backside

would intrinsically be inert to the target species without need of a blocking layer. Recently, Lubber *et al.* (102) explored the fabrication of AFM cantilevers using co-sputtered Cu-Hf that exhibited near zero stress gradient. This alloy is however prone to oxidation and is not particularly conducive to the detection of chemisorbed species. Thus, it does not offer such tunability over its chemical response, which precludes its use in practical sensing applications.

This chapter is a report on the fabrication of static microcantilevers fabricated out of Au-Ta composites and a demonstration of their use for the detection of a chemisorbed analyte. The impact of Ta concentration on the binding of 1-dodecanethiol is first determined using three different techniques. First, contact angle measurements are used to determine the hydrophobicity change attributable to exposure to dodecanethiol. Second, X-ray photoelectron spectroscopy is employed to look for the presence of sulfur bound to the surface of Au-Ta films. Third, Au-Ta coated Si cantilevers are fabricated and the deflection due to surface stress imparted by the assembly of dodecanethiol molecules is measured. All three techniques suggest that incorporation of small amounts of tantalum (5% and 10% at. Ta films) had little adverse effect on the attachment of dodecanethiol. This however ceased to be the case at 20% at. Ta and above, opening the possibility of designing cantilevers whose backside would be intrinsically inert to thiol chemistry.

Cantilevers as thin as 370 nm and with a spring constant as low as $10.5 \frac{mN}{m}$ were then realized out of a Au-Ta 5% alloy. The bottom surface of these all-metal cantilevers was however made of pure Ta, and thus intrinsically inert to the chemisorption of thiols. These devices were successfully employed to detect the attachment of dodecanethiol molecules through monitoring of static deflection induced by their binding onto their top surfaces.

5.3 Self-Assembled Monolayers

Self-assembled monolayers (SAMs) (7) are ordered molecular assemblies formed by the adsorption of an active surfactant on a solid surface. The two dimen-

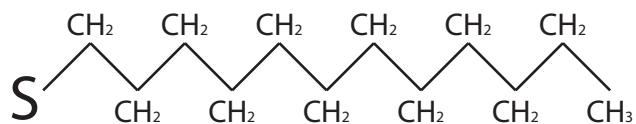


Figure 5.1: Diagram of the chemical structure of dodecanethiol

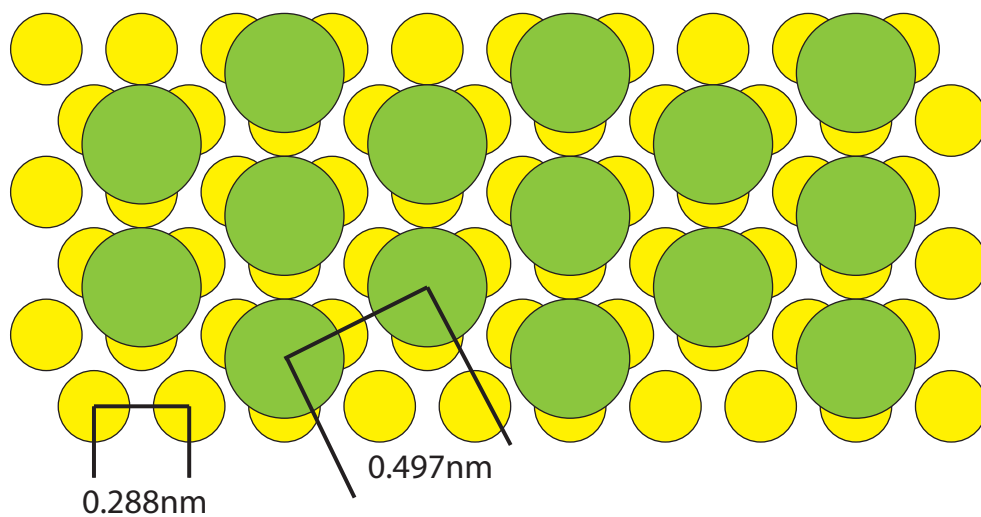


Figure 5.2: Diagram highlighting the organization of S atoms (large green circles) from Alkanethiols on the <111> surface of Au (smaller yellow circles).

sional order of these monolayers is generated spontaneously as adsorption of SAM molecules reaches equilibrium. There exists a large volume of review literature and books on the subject of SAMs (7; 213; 211; 214; 215). The two most common classes of SAMs are organosulfur compounds (like alkanethiols generally referred to as “thiols”) and organosilicon compounds (like alkyltrichlorosilane derivatives generally referred to as “silanes”). Silanes require the presence of hydroxyl groups on a surface to form a bond while thiols will bind to noble metals such as Au, Ag and Pd, (Au is most studied) (214). SAMs are important in the context of bio/chemical sensors because they are frequently used as building blocks of supermolecular structures that enable chemical or biological binding. As a proof of concept to demonstrate possible applications as a cantilever chemical or biosensor, we explore the attachment of dodecanethiol onto Au-Ta surfaces in this chapter. Dodecanethiol (Figure 5.1) is a simple alkane chain molecule with a sulfur atom at one end attached to a 12 carbon alkane (single bond) chain and is a liquid at room temperature. As mentioned in chapter 4, alkanethiol molecules in general have an affinity for the $\langle 111 \rangle$ face of PVD deposited Au. A top-view diagram of the arrangement of S atoms from an alkanethiol on the $\langle 111 \rangle$ surface of Au is provided in figure 5.2.

It has been observed however that depending on material surface and thiol deposition conditions, alkanethiol SAM formation takes place through the formation of several lower order “striped” phases of coverage before finally reaching the equilibrium “standing up” phase. Figure 5.3 is a diagram of three proposed phases of coverage as described by Godin *et al.* (83) this is in general agreement with other literature describing SAM phase evolution (216; 213; 214).

5.4 Contact Angle Measurements

One of the results of exposing a gold surface to alkanethiols is that the gold surface will be obscured from the environment by a organic layer with a hydrogen group at the end. This surface modification will change the interfacial properties of our thin film (217), specifically it will increase the hydrophobicity

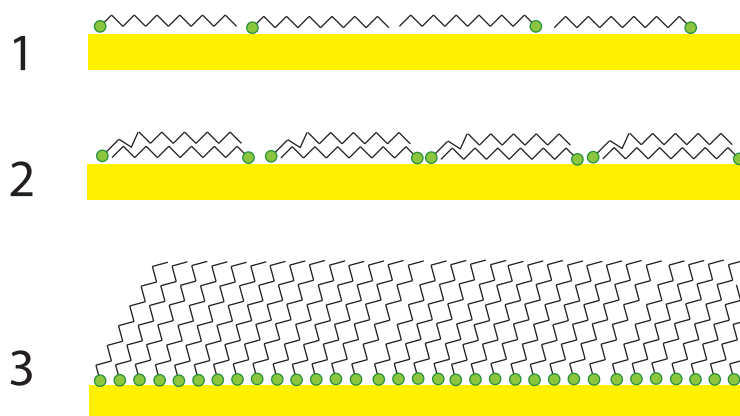


Figure 5.3: Diagram of three phases of SAM formation. Firstly, alkanethiols bind to the Au surface with alkane chain lying down on the Au surface. Second, as SAM formation evolves thiol molecules transition into a denser stacked lying down phase. Finally SAM reaches its fully formed “standing up” phase.

of the gold film. We can exploit this change of hydrophobicity to determine the presence of SAMs by evaluating the contact angle of water on our thin film surfaces.

To evaluate the contact angle we employ the static sessile drop method whereby a droplet of purified water is gently placed on the thiolized surface while monitored under a high resolution camera goniometer apparatus that is attached to a PC. The contact angle is ascertained using image analysis algorithms, or by manual tracing on the image where these algorithms fail. Typically for alkanethiols on pure gold surfaces, we observe contact angles of approximately 110° , while clean gold will exhibit a contact angle of approximately 20° (218; 219; 220; 80). Figure 5.4 is a side by side comparison of contact angle images for clean gold and thiolized Au showing the dramatic difference in wetting between these samples.

A series of silicon dies (Ultrasil) were cleaned with a piranha solution ($3\text{H}_2\text{SO}_4$: $1\text{H}_2\text{O}_2$) and sputter coated with a series of 20 nm thick Au-Ta films of varying

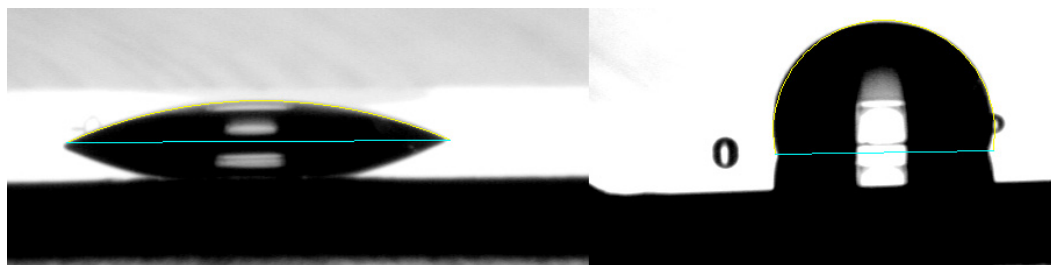


Figure 5.4: Images from contact angle goniometer. Left: Deionized water droplet on clean Au. Right: Deionized water on Au exposed to dodecanethiol vapour for 2 hours.

Ta contents (0, 5, 10, 20, 40% at. Ta). All films employed a 3 nm thick Ta adhesion layer. Each die was cleaned prior to film deposition by an Ar/O₂ plasma for 3 min while mounted in the sputter system (50 sccm Ar, 4 sccm O₂, 100 W). Prior to dodecanethiol exposure, the Au-Ta films were cleaned in a UV-Ozone cleaner for one hour at 70°C to minimize the presence of organic contamination before dodecanethiol deposition. One set of films was left out in the laboratory environment while an identical set was exposed to dodecanethiol vapor in a vacuum dessicator. After two hours, both sets of films were taken to a First Ten Angstroms contact angle goniometer, where the contact angle of deionized water was evaluated for each film using the static sessile drop method.

Figure 5.5 is a graph of the contact angle of deionized water droplets on the series of Au-Ta films, both clean and dodecanethiol exposed. The pure Au films behave as expected inasmuch as hydrophobicity was increased dramatically with dodecanethiol exposure. This contact angle however drops off dramatically as Ta content is increased, up to a point where there is no significant difference between the dodecanethiol exposed film and the control at 40 at.% Ta. Bain *et al.* (220) observed that in the case of on 1mM solution of octadecanethiol in ethanol, the water contact angle on gold reached ~90% of its final value within the first minute of SAM growth. These authors suggested that the bulk of change in contact angle was related to the initial “striped-phase” of SAM growth (216) rather than to the final, highly ordered arrangement

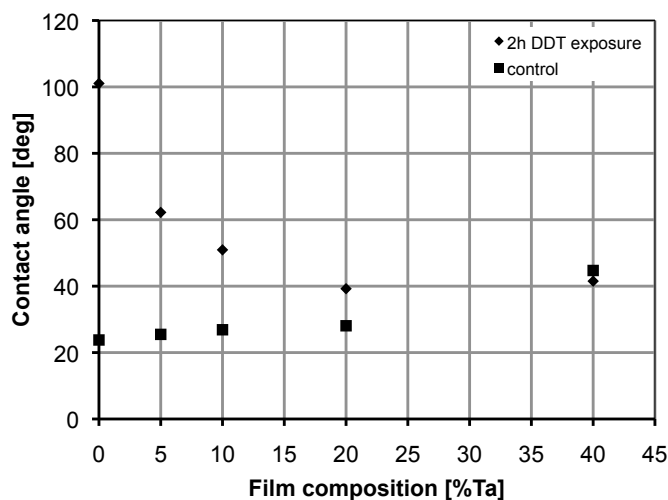


Figure 5.5: Contact angle of deionized water versus Ta content in Au-Ta film for clean and dodecanethiol exposed films.

of the layer. The dramatic reduction in the contact angle change as Ta content is increased thus here suggests a decrease in the efficiency of this initial “striped-phase” binding. We indeed previously observed that with increased Ta concentration, the Au-Ta films undergo both grain refinement and an increase in the lattice parameter (186). Both these changes could be contributing factors to the drop-off in dodecanethiol binding efficiency.

5.5 X-Ray Photoelectron Spectroscopy

X-ray photoelectron spectroscopy (XPS) is a characterization tool used to determine the elemental composition of a surface (28). A sample is irradiated with X-rays from a known source (typically the Al $K\alpha$ emission line) which causes the emission of photoelectrons from the outer shells of the atoms on the material surface. The energy and rate of photoelectron emission are measured by a detector and a spectra of photoelectron energy is generated, which can

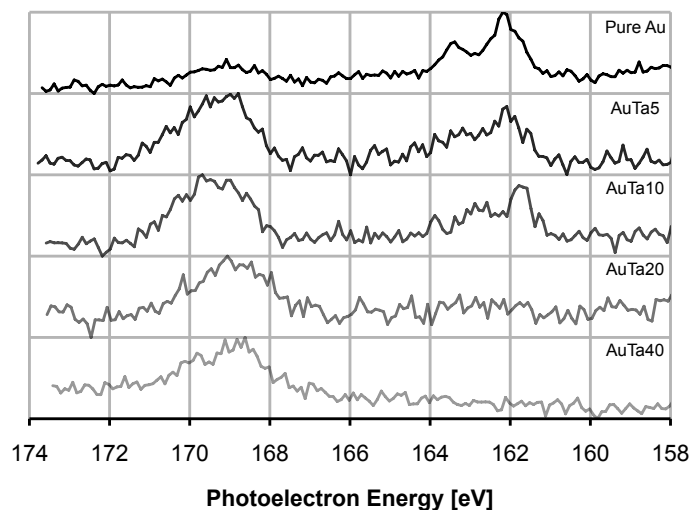


Figure 5.6: X-ray photoelectron spectroscopy curves for dodecanethiol exposed Au-Ta films. Two peaks are visible, one at 168 eV corresponding to nonspecific, unbound SO_x and one at 162 eV corresponding to elemental S from bound dodecanethiol molecules. Control samples showed only peaks at 169 eV.

be used to determine atomic composition of the surface. Bonds and oxidation states of the sample can also be determined in some cases. Prior to analysis, photoelectron energy spectra must be calibrated, which is typically done by ascertaining the location of the C1s peak and defining it at 285 eV.

Au-Ta films (0, 5, 10, 20, 40% at. Ta) were sputtered onto Si cantilever array chips (Concentris CLA-500-010-08) which had been cleaned prior to deposition by a 3 min Ar/ O_2 plasma (50 sccm Ar, 4 sccm O_2 , 100 W) in the sputter chamber. The dies were then UV-Ozone cleaned and exposed to dodecanethiol using the same protocol employed for the contact angle samples. The dies were then assayed by X-ray photoelectron spectroscopy. Dodecanethiol exposed and control samples were taken and mounted in an AXIS 165 X-ray photoelectron spectrometer where a high-resolution plot of photoelectron counts was recorded.

Figure 5.6 shows high resolution X-ray photoelectron spectrum of the S2p orbital binding energy acquired on Au-Ta films similarly exposed to the dodecanethiol. Two peaks are visible one centred around 162 eV attributed to elemental sulfur or to a sulfide (221) and the other centred around 169 eV attributed to a sulfate (SO_4^{2-}). Spectra acquired from samples with 0, 5, 10, 20, 40 % at. Ta suggests dominance of the sulfate peak (at 169 eV) over the sulfur peak (at 162 eV) as Ta concentration is increased. Buck *et al.* (222) observed similar behavior following the XPS analysis of hexadecanethiol SAM assembled onto gold. They specifically observed a peak initially present around 168 eV. The peak was however progressively replaced by a peak around 162 eV as the thiol was further allowed to interact with the gold. The explanation offered was that the initial 168 eV peak was due to SO_x from thiol molecules interacting with oxygen present on the gold surface due to the presence of organic contaminants. The oxidized sulfur peak was observed to markedly decrease, and became dominated by an elemental sulfur signal at 162 eV. This change in the energy of the S2p peak was also closely correlated with a decrease in the oxygen peak around 532 eV, as would be expected from an gradual substitution of organic contaminants with the assembled thiol layers. This process was termed “cleaning” of the gold and was also observed by Bain *et al.* (220). This being said, Ishida *et al.* (223) observed this SO_x peak on gold that was merely left in the laboratory environment for 24 hours without exposure to alkanethiols. This sulfur presence from environmental contamination is consistent with our XPS observations of the SO_x peak being present to some degree on all control and dodecanethiol exposed samples.

Figure 5.6 shows that only the pure Au, 5% Ta and 10% Ta films exhibit the sulfur S2p peak located around 162 eV. In turn, Figure 5.7 shows a plot of the relative weight (by area) of the 162 eV peak in the overall S2p spectrum. Figure 5.7 quite clearly shows that as the Ta concentration is increased in the Au-Ta films, the relative contribution of the 162 eV peak associated with elemental sulfur species decreases. This again confirms that there is a decrease in the “cleaning” of the gold at higher Ta concentrations. The lack of the 162 eV at higher Ta concentrations indicates that the dodecanethiol is no

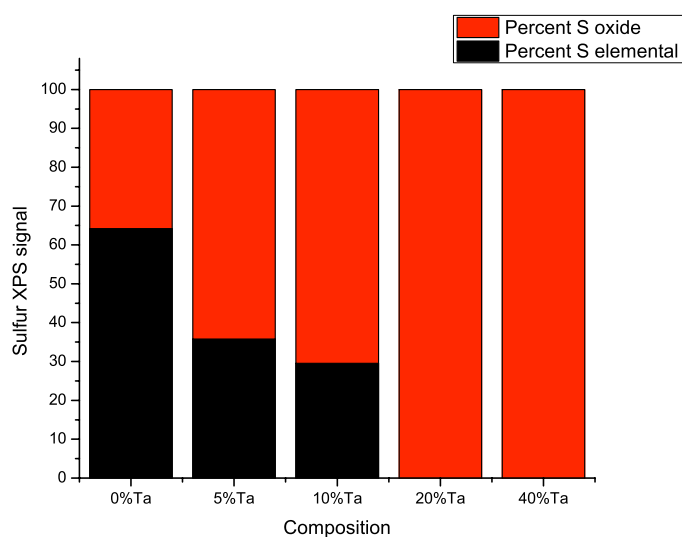


Figure 5.7: Bargraph of proportion of X-ray photoelectron spectroscopy counts attributed to SO_x and elemental S. As Ta is introduced to the Au-Ta films the proportion of elemental S decreases, corresponding to decreased dodecanethiol formation efficiency.

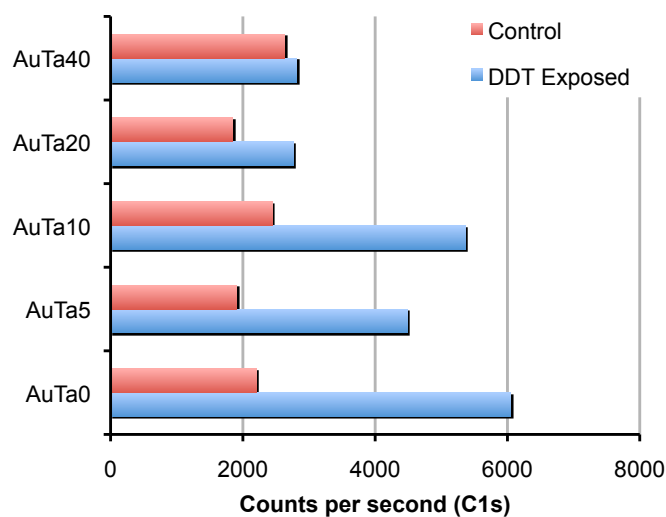


Figure 5.8: Bargraph of carbon signal for a series of clean (control) and dodecanethiol exposed Au-Ta films.

longer displacing the oxygen-containing contamination at those compositions. This would in turn further suggest that the initial dodecanethiol binding step is greatly inhibited by the incorporation of Ta at concentrations of 20% at. and above. These observations are in good agreement with the contact angle measurements.

The biggest constituent of the dodecanethiol molecule is carbon (12C : 1S) (H cannot be detected by XPS), therefore it was also of interest to monitor for the presence of carbon on all samples. This isn't the best way to quantify the presence of the dodecanethiol SAM, since all samples should exhibit some C signal from adventitious carbon contamination and thiol SAMs are known to displace contaminant molecules on the surface of Au, but it may provide some corroborating evidence of SAM presence. Figure 5.8 is a bargraph of counts per second at the C1s energy location showing that in the control samples there is a baseline C signal of ~ 2000 - 2500 CPS. In dodecanethiol exposed samples we can see that the Au-Ta 0, 5, and 10 % at. Ta samples have drastically higher

carbon counts than their control sample counterparts ~ 4500 - 6000 CPS which is attributable to the presence of bound dodecanethiol. The 20 and 40 % at. samples do not exhibit any significant increase in carbon presence over their control samples, likely due to very poor dodecanethiol binding. This result is in good agreement with the sulfur XPS analysis and contact angle analysis.

5.6 Fourier Transform Infrared Spectroscopy

Fourier transform infrared spectroscopy (FTIR) is a tool that can be used to detect the presence of molecules by monitoring for the absorption of infrared radiation at frequencies that correspond to the vibration of the specific chemical bonds in the molecule (224). FTIR is rather complimentary to XPS in that it can easily distinguish between different molecules that contain the same elements because it derives its signal from bond vibrations rather than energy levels of electrons in the molecule. Unfortunately, FTIR is a qualitative tool and cannot quantify the presence of molecules on a surface.

FTIR was performed on samples that were prepared identically and in parallel with those used in the contact angle measurements. A series of silicon dies (Ultrasil) were cleaned with a piranha solution ($3\text{H}_2\text{SO}_4 : 1\text{H}_2\text{O}_2$) and sputter coated with a series of 20 nm thick Au-Ta films of varying Ta contents (0, 5, 10, 20, 40% at. Ta). All films employed a 3 nm thick Ta adhesion layer. Each die was cleaned prior to film deposition by an Ar/O₂ plasma for 3 min while mounted in the sputter system (50 sccm Ar, 4 sccm O₂, 100 W). Prior to dodecanethiol exposure, the Au-Ta films were cleaned in a UV-Ozone cleaner for one hour at 70°C to minimize the presence of organic contamination before dodecanethiol deposition. One set of films was left out in the laboratory environment while an identical set was exposed to dodecanethiol vapor in a vacuum dessicator. After two hours, FTIR spectra were gathered for both sets of films using a Nicolet Nexus 760 FTIR spectrometer with a DTGS detector and a nitrogen-purged sample chamber. All acquisitions were obtained using 32 scans with a 4 cm^{-1} resolution. The FTIR spectra of the control films were

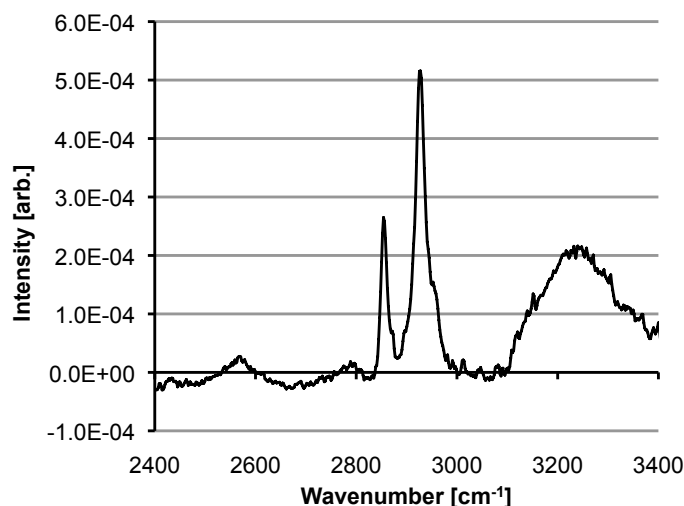


Figure 5.9: FTIR absorption spectra peaks of dodecanethiol on Au-Ta 5% film. Peaks between 2850 cm^{-1} and 3000 cm^{-1} correspond to absorption by CH_3 and CH_2 bonds of alkane chain.

subtracted from their corresponding dodecanethiol film counterparts and the background machine FTIR signature was removed to reveal the absorption peaks.

In FTIR studies of thiol molecules, it has been noted that the C-S and C-S-H bonds give rise to rather weak absorption in the infrared spectrum, but are highly polarized making Raman spectroscopy a better candidate to monitor for the presence of these bonds. We are therefore left to determine alkanethiol presence by monitoring the presence of CH_2 and CH_3 groups which are known to absorb IR radiation in the $2800\text{-}3000\text{ cm}^{-1}$ window (210; 211; 213; 224). Figure 5.9 is a plot of the $2800\text{-}3000\text{ cm}^{-1}$ window of the IR absorbance spectra of an Au-Ta 5% at. Ta sample exposed to dodecanethiol. We can see two clear peaks around 2850 cm^{-1} and 2950 cm^{-1} corresponding to the stretching of C-H bonds in the CH_3 and CH_2 groups of the alkane chain of dodecanethiol. These peaks were observed for all five Au-Ta compositions tested, but were observed to grow progressively weaker (until spectrometer levelling artifacts

were more pronounced than the peaks) as more Ta was incorporated into the alloy. This result confirms that dodecanethiol indeed binds to Au-Ta films and is consistent with contact angle and XPS results.

5.7 Au-Ta Coated Silicon Cantilevers

To assess the effect of changing alloy concentration on the stress imparted by dodecanethiol SAM assembly we prepared a series of commercially available single crystal Si cantilever array chips (Concentris CLA-500-010-08) coated with the same series Au-Ta nanocomposite alloy films (0, 5, 10, 20, 40% at. Ta). The cantilever chips consisted of eight identical cantilever beams 500 μm in length, 100 μm in width and 1 μm in thickness. Cantilever chips were prepared as before with films of 20 nm of sputtered Au-Ta alloy. Each cantilever chip was cleaned by an Ar/O₂ plasma for 3 min prior to film deposition while mounted in the sputter system (50 sccm Ar, 4 sccm O₂, 100 W).

The Au-Ta coated cantilever dies were then placed in a UV-O₃ system at 70°C and cleaned for one hour, removed and allowed to cool for approximately 10 min. Initial deflection data is taken for each cantilever on each chip using a Zygo NewView 5000 imaging white light interferometer.

With the initial deflection data recorded, one set of cantilever chips was left out in the laboratory environment while an identical set was exposed to dodecanethiol vapor in a vacuum dessicator. After two hours, the deflection of the cantilever chips was once again measured with imaging white light interferometry. The change in cantilever deflection was calculated for each cantilever beam on each chip and averaged to produce a deflection change for each composition of Au-Ta. The deflections from the control samples were then subtracted from the dodecanethiol exposed samples to account for noise due to effects such as unstable oxide formation by UV-O₃ (219; 225) cleaning or fluctuations in ambient temperature in the lab environment.

5.7.1 White Light Interferometry

Imaging white light interferometry was preferable to other methods of deflection measurement for a couple reasons. Firstly, this technique allows measurement of the deflection of the cantilever with a high resolution (sub $\mu\text{m}^2/\text{pixel}$) as opposed to being limited to measuring the displacement of one single large spot using an AFM style split photodiode readout. Secondly, in an AFM style split photodiode readout, it is imperative that the location of the laser spot on the cantilever be well quantified in order to accurately translate the measurement into a stress value. Imaging the cantilevers deflection profile bypasses this possible source of error.

Recalling equation 2.35, we can use Stoney's equation to correlate cantilever tip deflection to the surface stress with the following equation.

$$\Delta\sigma = \frac{Eh^2\Delta z}{3l^2(1-\nu)} \quad (5.1)$$

where σ is the stress at the top surface of the cantilever, E is the Young's modulus of the cantilever, t is the cantilever thickness, l is the length of the cantilever, Δz is the change in cantilever end height caused by the induced stress, and ν is the Poisson's ratio of the cantilever.

It is notable that equation 5.1 has an l^2 dependence. When using a split photodiode setup, the placement of the laser spot along the length of the cantilever dictates the length in this l^2 term. To have run to run consistency it is imperative that we are able to place the laser beam at the same place on the cantilever every time a cantilever chip is mounted in the setup. Initial explorations of the effect of Ta content on dodecanethiol binding to Au-Ta coated cantilevers were performed in the Concentris Cantisens CSR-801 system. The Cantisens system has a CCD camera that can be used to help maneuver the cantilever substrate into position so that the cantilevers impinge the laser path. The problem with this is that the laser spot appears quite large in the CCD image with a diameter approximately that of the width of the cantilevers themselves

(100 μm). Assuming that we can align the laser beam on the cantilever arrays to within 50 μm of where the beam was placed on a previous run, we conclude that we could have a deflection error of as high as 19% between runs. In addition to this, the cantilevers cannot be positioned independently since they are mounted on the same substrate, so any tilt in the mounting of the substrate will manifest itself as a progressively lower deflection signal as we go down the cantilever array, further confounding signal comparison between runs. Given the limitations of the Cantisens system we opted to measure cantilever deflection using the Zygo NewView 5000 imaging white light interferometer for the sake of run to run consistency. Having a cantilever length associated with every deflection datapoint would ensure this consistency.

5.7.2 Temperature Sensitivity

Analytic Solution

It is understood that a cantilever can form the basis of an extremely sensitive calorimeter through leveraging the “bimetallic effect” (77; 140). This is beneficial if we desire to apply calorimetry as a means to sense an analyte, otherwise this effect must be regarded as a source of noise. The deflection of a bimorph cantilever due to a change in temperature can be described by the following equations (75; 76).

$$\Delta z = \frac{3}{t_b^2 K} (\alpha_c - \alpha_b) (t_c + t_b) l^2 \Delta T \quad (5.2)$$

$$K = 4 + 6\left(\frac{t_b}{t_c}\right) + 4\left(\frac{t_b}{t_c}\right)^2 + \frac{E_b}{E_c}\left(\frac{t_b}{t_c}\right)^2 + \frac{E_c}{E_b}\left(\frac{t_c}{t_b}\right) \quad (5.3)$$

Where Δz is the cantilever deflection, t_b and t_c are the thicknesses of the beam and the coating film, E_b and E_c are the Young’s modulus for beam and coating, α_b and α_c are the coefficients of expansion for the beam and the coating film, l

Table 5.1: Theoretical temperature-induced tip deflection and stress noise in Ti/Au coated Si cantilevers, Ti/Au coated SU-8 cantilevers, the most stress sensitive Au-Ta “metal-only” cantilever fabricated (with 10 nm Ta adhesion layer), and the same Au-Ta cantilever scaled up to 500 μ m long (a common length for commercial static cantilever sensors). Values are calculated from equations 5.2 and 5.3

Cantilever label	E_{beam} GPa	E_{film} GPa	α_{beam} $\frac{10^{-6}}{^{\circ}C}$	α_{film} $\frac{10^{-6}}{^{\circ}C}$	Tip defl. $\frac{nm}{^{\circ}C}$	Str. noise $\frac{N}{m^{\circ}C}$
Si + Ti/Au	150	83	2.6	13.5	101	0.028
SU-8 + Ti/Au	3.0	83	54	13.5	-203	0.044
Au-Ta 5% l=140 μ m	115	186	13.8	6.3	47.9	0.023
Au-Ta 5% l=500 μ m	115	186	13.8	6.3	611	0.023

is the effective cantilever length (or where the beam spot is actually located), and ΔT is the induced change in temperature.

Equation 5.2 shows that the cantilever tip displacement due to thermal mismatch is a linear function. Applying this equation to Silicon and SU-8 cantilevers coated with 3 nm Ti adhesion layer and 20 nm Au we can compare the theoretical tip deflection and stress noise attributable to temperature. We employ the Concentris CLA-500-010-08 (226) as the basis for the model silicon cantilevers and cantilevers described by Keller *et al.*

citeKeller:2010p1273 as the basis for the model SU-8 cantilevers. For these calculations, the metal film’s E and α were determined from a volumetric interpolation of reference values for the E and α of Au and Ti. α_{AuTa} is determined by molar interpolation of α_{Au} and α_{Ta} reference values and E_{AuTa} is determined from the resonating cantilever method used in chapter 4.

We can see from table 5.1 that even when coated with extremely thin gold layers (to enable thiol binding) the SU-8 and Si cantilevers undergo deflection corresponding to significantly higher values of surface stress than the Au-Ta cantilevers.

Finite Element Analysis

A series of two dimensional finite element models were constructed in COMSOL 3.5a using the MEMS package thermal-structural interaction “SMPS” to corroborate the theoretical temperature noise calculations. All models were constructed using the same E and α values as table 5.1. Unfortunately, Au-Ta coated silicon cantilever models could only be run at the most coarse (“extremely coarse”) adaptive mesh settings possible due to the extreme aspect ratio of the cantilever devices. The Au-Ta 5% “metal only” cantilevers could be run at higher mesh densities, but the model still demonstrated some mesh sensitivity before machine limitations generated solution errors. Thus we were unable to perform the simulations at an adequate mesh density and the results should be taken with a grain of salt. Nonetheless, the simulated structures indeed displayed a tip deflection that increased linearly with temperature (as the analytic model suggests) and differed from the analytically predicted values by <15% in the worst case. It was determined that surface stress noise due to temperature fluctuations shouldn’t be a significant issue given the controlled environment of the Nanofab and our precautions taken by measuring control and dodecanethiol cantilever deflection.

5.7.3 Stress Induced by Dodecanethiol Attachment

The derivation of stress as a function of deflection from Stoney’s formula is appropriate for use when the Young’s modulus of the cantilever material is well defined. In the case of cantilevers where compliance is provided by a measured spring constant (such as AFM cantilevers or other micro-cantilevers), it may be more appropriate to use a stress sensitivity formulation based on this property, since material properties of common cantilever materials like LPCVD Si_3N_4 vary greatly depending on process recipe. Godin *et al.* (227) published a method to determine stress sensitivity of a microcantilever from its spring constant using an energy method. The resulting stress sensitivity of a cantilever of rectangular cross-section is:

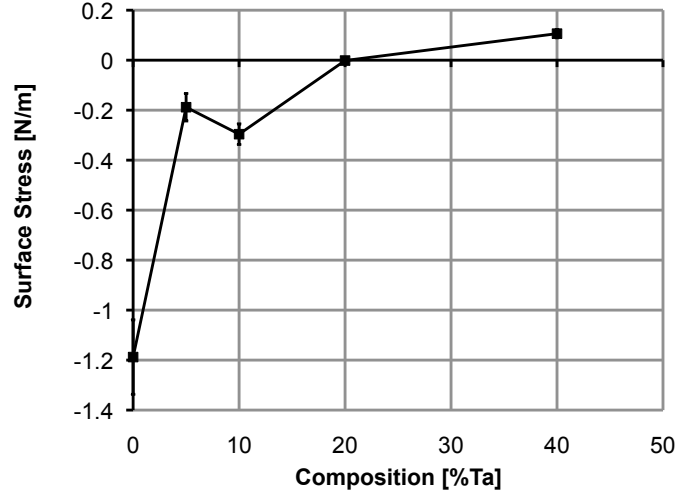


Figure 5.10: Stress induced by the attachment of dodecanethiol on silicon cantilevers coated with a series of Au-Ta compositions. As Ta content is increased induced stress decreases, corresponding to poorer dodecanethiol binding.

$$\Delta\sigma = \frac{4lk\Delta z}{3(1-\nu)wt} \quad (5.4)$$

where $\Delta\sigma$ is the change in surface stress, l is the cantilever length, w is the cantilever width, t is the cantilever thickness, ν is the Poisson's ratio of the material and Δz is the change in deflection of the cantilever. This stress-deflection relationship was applied to the Au-Ta coated silicon cantilever deflection data taken by white light interferometry.

Figure 5.10 shows a plot of the surface stress induced by the chemisorption of the dodecanethiol onto a series of Au-Ta coated Si microcantilevers. Cantilevers coated with low-Ta composition Au-Ta films (pure Au, 5% at. Ta and 10% at. Ta) exhibited a compressive surface stress and thus a downwards bending. The surface stress observed for pure Au ($1.2 \frac{N}{m}$) was similar to those observed by Godin *et al.* (83), Desikan *et al.* (85), and Berger *et al.* (82) (ie

0.51 $\frac{N}{m}$, $\sim 1.0 \frac{N}{m}$, and 0.19 $\frac{N}{m}$, respectively). As expected, the surface stress decreases as Ta content is increased and becomes nearly negligible in cantilevers coated with films with 20% and 40% at. Ta composition.

It is notable that this decrease in the compressive stress as Ta content is increased is correlated with a decrease in the elemental sulfur XPS signal and a decrease in the water contact angle. Godin *et al.* (83) observed a sharp decrease in the stress imparted on his Au surfaces as the grain size of the Au was reduced. This was attributed to the relative ability of the dodecanethiol SAM to achieve its final highly-ordered “standing up” state. Our previous work with Au-Ta nanocomposites (186) showed that the introduction of Ta leads similarly reduced the Au grain sizes. A decrease in surface stress with increased Ta content is therefore expected.

5.8 Gold-Tantalum Cantilevers

5.8.1 Fabrication

A series of cantilevers were fabricated directly out of Au-Ta 5% to synthesize a cantilever of superior sensitivity to stresses. In our preliminary study of these Au-Ta nanocomposite alloys (186), we noted that the 5% at. Ta concentration could be sputter deposited on a silicon substrate without inducing any meaningful bending due to stress. From these observations, we know that the stress gradient of the Au-Ta 5% material should be small enough that we could completely release a cantilever made entirely of this material.

Figure 5.11 contains a schematic of the process flow for fabricating Au-Ta 5% cantilever sensors. First a Si <100> wafer (Ultrasil) is cleaned in a piranha solution ($3\text{H}_2\text{SO}_4 : 1\text{H}_2\text{O}_2$) and a bilayer of LOR 5B (Microchem) and HPR 504 (FujiFilm) photoresists is spun. The photoresists were patterned with contact photolithography and developed such that there was an approximately 5 μm overhang in the top layer of HPR 504 photoresist. A 10 nm Ta adhesion layer

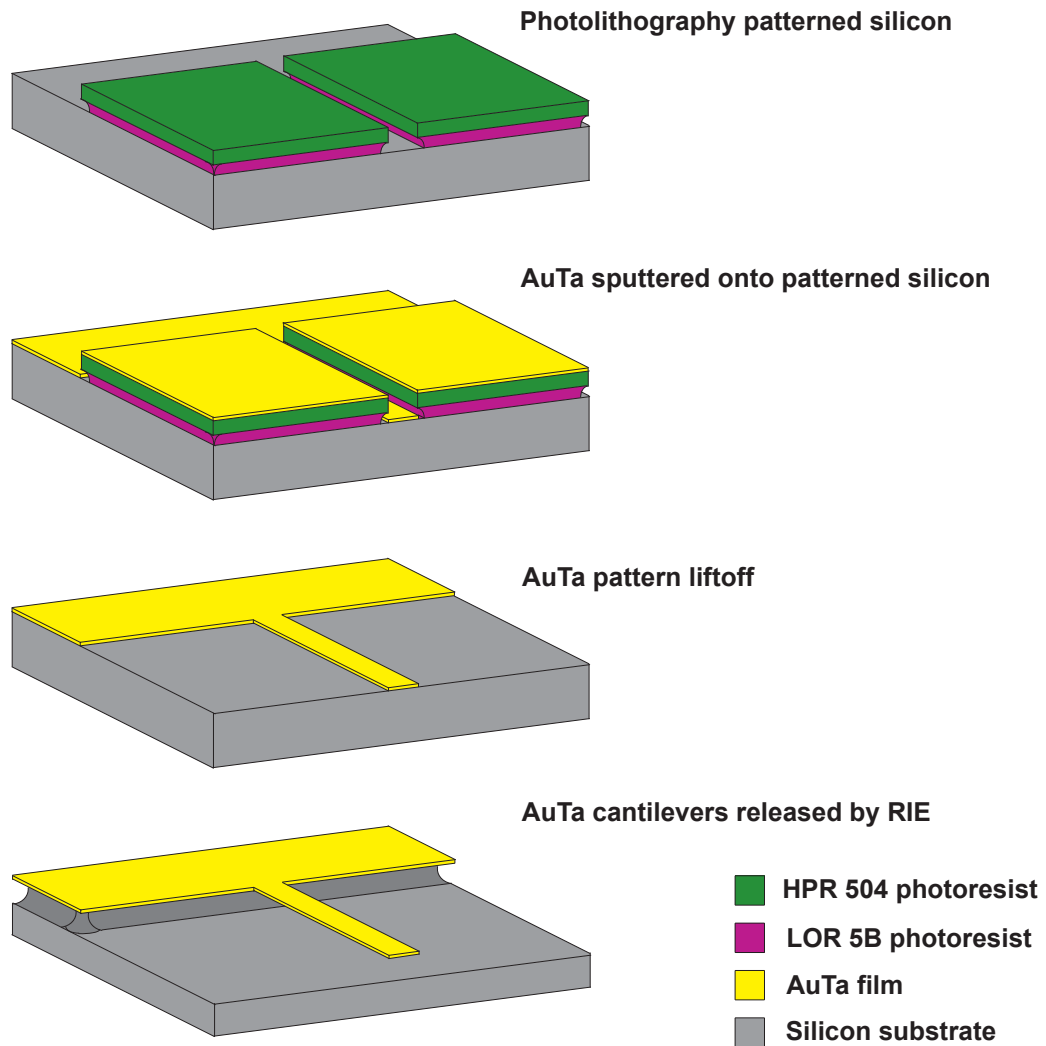


Figure 5.11: Process flow for the fabrication of Au-Ta 5% static micro-cantilever transducers.

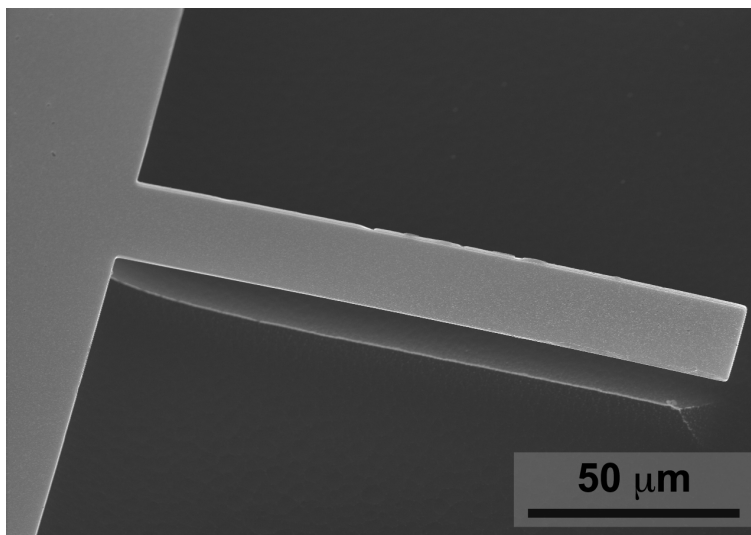


Figure 5.12: Scanning electron micrograph of a static Au-Ta 5% microcantilever with dimensions $l = 140 \mu\text{m}$, $w = 20\mu\text{m}$ and $t = 370 \text{ nm}$.

and 400 nm thick Au-Ta 5% layer were then sputtered onto the patterned wafer. The Ta adhesion layer would later serve as a blocking layer, preventing alkanethiol molecules from binding to the bottom surface of the cantilever. Excess photoresist was removed from the silicon wafer with an ultrasonic acetone bath followed by a 2 min rinse in Remover PG (Microchem), leaving behind only the cantilever pattern in Au-Ta alloy. The patterned Au-Ta mechanical layer was then released from the silicon wafer by exposure to an isotropic SF_6 reactive ion etch (50 sccm SF_6 , 50 mTorr, 50 W, 60 min etch time). The plasma etch conditions were optimized to release the $20 \mu\text{m}$ wide and narrower cantilever beams. Figure 5.12 shows a scanning electron micrograph of a released Au-Ta 5% cantilever ($140 \mu\text{m}$ long by $20 \mu\text{m}$ wide) fabricated by this method. Using cross sectional scanning electron microscopy (SEM), we determined that the SF_6 plasma etch step had thinned the 410 nm cantilevers down to approximately 370 nm.

5.8.2 Alternate Release Methods

Initially a traditional wet etch bulk micromachining approach was taken to release the Au-Ta 5% static cantilever structures, as outlined in chapter 2. Cantilever patterns were deposited on the front side of doubly polished silicon $\langle 100 \rangle$ wafers. The wafers were then coated (device side and bottom) with a PECVD synthesized SiO_2 layer. Photolithography was employed to open up a window to allow for anisotropic TMAH etching from the wafer's backside which would completely release the Au-Ta cantilevers. TMAH was employed over KOH since it is known to be selective to Au (115) and metals in general. Unfortunately, TMAH is roughly half as fast as KOH for etching through Si, necessitating ~ 16 h to etch through a standard $500 \mu\text{m}$ wafer. Ultimately, poor adhesion and porosity of the SiO_2 mask to the Au-Ta metal caused mask delamination exposing the Au-Ta cantilevers to the TMAH solution after a couple hours. Thus, to preserve the Au-Ta cantilever integrity it was necessary to remove wafers from the TMAH etching solution before the wafer was entirely etched through. The wafers were dried using critical point drying, though they were so compliant that turbulence in the CPD chamber was enough to cause deformation. XeF_2 vapour was also explored as an alternate method of release since it also etches Si over Au with an extremely high selectivity. Unfortunately the cantilever structures were deformed due to the turbulent pulsed nature of the XeF_2 vapour chamber controller. Ultimately, the SF_6 plasma etch was chosen since it did not cause the cantilever devices to plastically deform during release and still exhibited a very high selectivity of Si to Au.

5.8.3 Initial Conditions

For most static cantilever transduction methods (such as PSD and white light interferometry), it is important to ensure that the cantilever beam is not experiencing excessive initial out of plane bending, so that its deflection may be read out accurately. Cantilever bending can be attributed to both residual

mean stress and residual stress gradients (159). Keller *et al.* (209) found initial bending to be a significant issue when fabricating SU-8 static cantilever sensors and used a camera to generate a cantilever bending profile. Fang and Wickert's model (159) could then be applied to these profiles to determine mean stress and stress gradient in their cantilevers. This stress information was then used to modify the SU-8 baking steps to reduce both stress gradients and mean stresses, reducing initial bending.

In Fang and Wickert's model, cantilever bending is separated into a bending term with a constant radius of curvature "R" and a rotational deformation about the clamping point with an angle θ .

$$z_{tot} \approx z_b + z_r = \frac{x^2}{2R} + \theta x \quad (5.5)$$

where the angular rotation θ is composed of θ_m due to mean stress and θ_g due to the stress gradient.

$$\theta_m \approx \frac{\sigma_m}{E}(1.33 + 0.45\nu)(-1.4 \cdot 10^{-4}t + 1.022) \quad (5.6)$$

$$\theta_g \approx \frac{\sigma_g}{E}(6.6 \cdot 10^9 t^2 - 4.7 \cdot 10^{-4}t + 0.81) \quad (5.7)$$

Using white light interferometry, we were able to extract a cantilever profile for a series of lengths of released Au-Ta 5% cantilevers to ascertain the effect of SF₆ etch release time and UV-O₃ cleaning on the cantilever stress profile. Extraction of the cantilever's mean stress was highly dependant on accurately locating the clamping point, which was impractical given the undercut resulting from the isotropic SF₆ etch release. Analysis was therefore constrained to stress gradient calculations since these were relatively invariant with small errors in clamping point location. A second order polynomial fit was applied to the cantilever profile in order to extract the radius of curvature so the stress gradient could be computed. Figure 5.13 is a graph of cantilever stress gradient versus release time for just released and UV-O₃ cleaned Au-Ta 5% cantilevers.

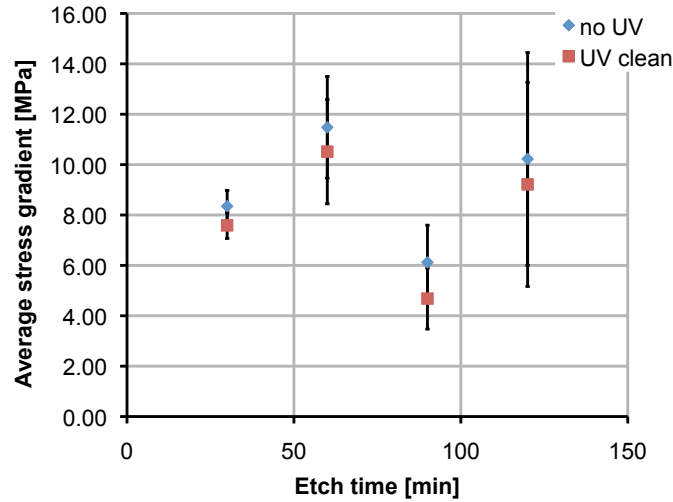


Figure 5.13: Stress gradient of identically deposited Au-Ta 5% cantilevers with varied release times. Stress gradient was also obtained for the same cantilever samples after UV-O₃ cleaning.

From figure 5.13, we do not see a relationship between SF₆ etch release and the resultant curling of the cantilever. The cantilevers do however undergo a small downward deflection upon UV-O₃ cleaning, reducing the measured stress gradient. We can now be confident that the effects of SF₆ etch time have minimal effect on the cantilever's initial deflection, enabling more aggressive cantilever designs in the future.

5.8.4 Sensitivity Comparison

The sensitivity of a static cantilever sensor is typically quantified by the cantilever's spring constant. Recalling equation 2.9, we know that the spring constant of a cantilever can be calculated from the following equation.

$$k = \frac{3EI}{L^3} \quad (5.8)$$

Table 5.2: Comparison of spring constants of recently published and commercially available highly compliant microcantilevers and the Au-Ta cantilevers fabricated in this study.

Cantilever label label	Length μm	Width μm	Thickness nm	Spring const $\frac{N}{m}$
Au-Ta 1	35	5	369	1.68×10^{-1}
Au-Ta 2	45	10	369	1.59×10^{-1}
Au-Ta 3	65	20	369	1.05×10^{-1}
Au-Ta 4	70	10	369	4.21×10^{-2}
Au-Ta 5	90	20	369	3.96×10^{-2}
Au-Ta 7	140	20	369	1.05×10^{-2}
Cantisens CLA-500-010-08	500	100	1000	3.00×10^{-2}
Calleja <i>et al.</i> citeCalleja:2003p1270	200	20	1500	1.50×10^{-2}
Keller <i>et al.</i> citeKeller:2010p1273	500	100	2000	4.80×10^{-3}
Mikromasch 17 series	460	50	2000	1.50×10^{-1}
Au-Ta scaled up	500	20	369	2.31×10^{-4}

Where E is the Young's modulus, I is the cantilever's moment of inertia ($I = \frac{wt^3}{12}$) and L is the cantilever's length.

Spring constant is a measure of the cantilever's sensitivity to a point force and not a surface stress distributed over the cantilever. However, since it is measurable with an AFM and it is correlated to stress sensitivity, spring constant is the prevalent way to quantify a static cantilever's sensitivity. Table 5.2 is a summary of cantilever dimensions and spring constants for the Au-Ta 5% static cantilevers outlined in this chapter, commercially available Si cantilevers, and published SU-8 cantilevers.

Table 5.2 shows that the spring constant of the most compliant Au-Ta 5% cantilevers is comparable to the most sensitive SU-8 and commercially available silicon cantilever structures. If the length of our most sensitive Au-Ta cantilever is scaled up to a typical commercial static cantilever length (500 μm) we see that the spring constant is lower than the most sensitive SU-8

cantilevers by more than an order of magnitude. This coupled with the lower thermal noise (Table 5.1) of our Au-Ta cantilevers would enable far greater real world sensitivity to thiolized molecules.

5.8.5 Stress Induced by Dodecanethiol Attachment

A set of all-metal Au-Ta 5% cantilevers were used to measure the stress as a result of dodecanethiol chemisorption in order to determine their applicability as chemical sensors. Two identical chips (fabricated as described in section 5.8.1) with varied cantilever geometries were cleaned in a UV-O₃ cleaner for one hour at 70°C and allowed to cool for 10 min. Initial cantilever deflections were measured by white light interferometry. One chip was then placed in a vacuum dessicator and exposed to dodecanethiol vapor for 2 h, while the other chip was left exposed to the laboratory environment. The deflection of the two cantilevers was measured again and the difference in deflections translated into an assessment of the surface stress imparted by the chemisorption of the dodecanethiol.

Figure 5.14 shows a graph of deflection of each cantilever as a function of device sensitivity. A fit of this data to equation 5.1 ascribes a stress of $1.07 \pm 0.09 \frac{N}{m}$ to the dodecanethiol exposure. This stress is significantly different from the $0.2 \frac{N}{m}$ value observed in the silicon cantilevers coated with Au-Ta films of similar Ta content. This difference could be related to some variation in of the alloy's mechanical properties or the Au-Ta grain size changing with device thickness. Finally, in spite of their relative shortness, the theoretical spring constant of these cantilevers ranged from $168 \frac{mN}{m}$ to $10.5 \frac{mN}{m}$ which is already comparable to the most compliant cantilevers reported in literature. Fabrication of longer and thinner cantilevers showing spring constants below the $1 \frac{mN}{m}$ mark is currently underway.

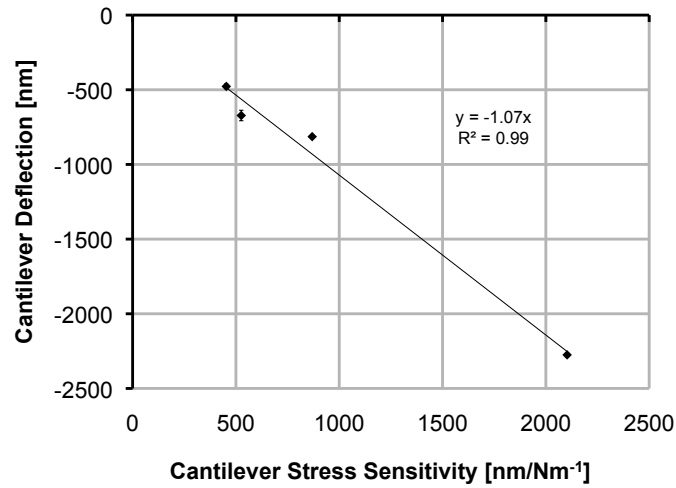


Figure 5.14: Deflection versus stress sensitivity for a suite of Au-Ta 5% cantilevers exposed to dedecanethiol. Cantilever deflections correspond to an induced stress of $\sim 1.07 \frac{N}{m}$ after two hours dodecanethiol exposure.

5.9 Summary

Static microcantilever sensors were fabricated directly out of a Au-Ta nanocomposite synthesized by a co-sputtering process. The attachment of dodecanethiol molecules onto the surface of such films was first assessed using contact angle measurements, X-ray photoelectron spectroscopy, fourier transform infrared spectroscopy and stress measurements using silicon microcantilevers coated with the alloy. It was observed that as tantalum was added to alloy films, the water contact angle for dodecanethiol exposed films decreased dramatically, from over 100° for pure Au to $\sim 40^\circ$ for the 20% and 40% at. Ta films. XPS measurements also showed that as Ta is incorporated in the alloy, the ratio of elemental S to SO_x decreases until no elemental S can be observed for the 20% and 40% at. Ta films. FTIR scans showed the presence of absorbance peaks corresponding to the stretching in CH_2 and CH_3 groups of the alkane chain of dodecanethiol in all samples, though qualitatively the peak was very weak as Ta content was increased to 20% and above. The stress associated with dodecanethiol assembly on Au-Ta coated silicon cantilevers was observed to decrease as the concentration of Ta was increased. Silicon cantilevers coated with pure Au exhibited stress similar to previously published values and as Ta was increased in the films stresses associated with SAM assembly decreased until the 20% and 40% at. Ta films showed negligible deflection due to stress. It was concluded that while the Au-Ta films retained the FCC structure and $\langle 111 \rangle$ texture of Au the inclusion of Ta in solid solution inhibits the initial binding step of alkanethiol molecules as Ta is increased. The 5% and 10% at. Ta films still showed significant dodecanethiol binding but 20% and 40% at. Ta showed no evidence of significant binding. This tunability of the chemical affinity of the alloy therefore allows the design of ultra-thin all-metal cantilevers whose backside is intrinsically inert to the target analyte. This feature foregoes the need of a passivation step and would greatly simplify the analysis and handling of sensors based on such structures.

To that end, all-metal Au-Ta nanocomposite alloy metal-only cantilevers were

successfully employed to detect the attachment of dodecanethiol. Spring constant of the Au-Ta cantilevers fabricated and employed in this study were as low as $10.5 \frac{mN}{m}$, which is already comparable to the most compliant commercially available silicon microcantilevers. These Au-Ta cantilevers were however substantially shorter than typical silicon devices, thus limiting the ultimate stress sensitivity of the cantilever device. Initial bending was minimal and was determined to be relatively invariant with changing SF₆ release etch times. Design revisions currently underway to scale up the length of the Au-Ta cantilevers closer to the commercially available Si cantilevers promise to increase the stress sensitivity tenfold.

CHAPTER 6

The Application of Atomic Layer Deposition Materials for Resonant Cantilever Applications

6.1 Introduction

We applied our nanofabrication expertise to the fabrication of NEMS resonators out of atomic layer deposition (112; 228) material. This work is a logical extension to the work in chapter 3, as many ALD materials have a high Young's modulus and low density, making them ideal for NEMS resonator applications. Initial NEMS resonator studies were conducted using single crystal Si as the resonator material. To employ a NEMS resonator as a gravimetric transducer we desire a material that is light and stiff, Si has both of these properties. The frequency response of a cantilever to an added mass is inversely proportional to the cantilever's mass (equation 2.28) thus to achieve a cantilever of unprecedented sensitivity we wish to reduce its dimensions as well. Single crystal silicon materials are prone to brittle failure when machining devices with dimensions below approximately 50 - 60 nm (106; 107). The cause of these yield problems has been attributed to lattice damage from the reactive ion etching step. The brittle nature of RIE damaged Si necessitated the move towards nanocantilevers made from glassy materials like Si_3N_4 (109) and SiCN (110).

The lateral dimensions of a NEMS resonator are determined by the patterning and etching steps in fabrication. Low voltage electron beam lithography and reactive ion etching already been applied for the fabrication of sub 10 nm resonator beams in glassy SiCN (111). In the case of these SiCN resonators, the beam thickness was 50 nm, as this was the thinnest layer that could be reliably deposited in the PECVD process. In order for reductions in device thickness to catch up to reductions in lateral dimensions one needs to use a film synthesis technique that is inherently slower than most CVD technologies. Atomic layer deposition is a CVD technology, capable of synthesizing glassy or nanocrystalline materials. ALD is inherently limited in deposition rate making it a viable candidate for the production of NEMS resonators into the sub 10 nm scale regime. In this chapter¹, we describe the deposition, characterization and machining of TiN from ALD. We fabricated cantilever beams out of lightly tensile stressed ALD TiN films, though we were unable to assay the device's resonance frequency.

6.2 ALD Background

Atomic layer deposition employs chemical vapours in vacuo to make thin films in this way it is similar to the chemical vapour deposition technologies which were briefly discussed in chapter 4. The difference between ALD and CVD technologies lies in the self-limiting nature of the ALD reaction. Generally in CVD reactions, one or more gasses are flowed over the substrate in a temperature and vacuum controlled environment such that the gas(es) react at the surface of the substrate to form the desired thin film. CVD methodolo-

¹Work in this chapter was conceived by N. Nelson-Fitzpatrick and K. Harris. ALD films were deposited by N. Nelson-Fitzpatrick and K. Harris. Reactively sputtered films were deposited by N. Nelson-Fitzpatrick. Optical reflectometry and stress measurements were performed by N. Nelson-Fitzpatrick. Spectroscopic ellipsometry was performed by N. Nelson-Fitzpatrick with helpful input by B. Szeto and N. Wakefield. X-ray diffraction was performed by B. Worfolk and analyzed by N. Nelson-Fitzpatrick. Machining of reactively sputtered and ALD films was performed by N. Nelson-Fitzpatrick. Electron microscopy was performed by N. Nelson-Fitzpatrick

gies have spawned a plethora of sub-technologies (LPCVD, PECVD, MOCVD) (28) and have been well explored to synthesize materials (Poly-Si, Si_3N_4 , PSG) that have proven essential to MEMS and microelectronics technologies.

We can regard ALD as a CVD reaction that is broken into two half reactions (112; 228). In the first half reaction, the ALD chamber is exposed to a “precursor vapour which adsorbs onto the device substrate, subsequently the extra waste vapour is purged from the chamber. The second half reaction is now carried out and the chamber is exposed to a “reactant” vapour that adsorbs onto the substrate and reacts with the precursor chemical. Ideally this reaction will form a one molecule thick layer of our desired material. Excess reactant is purged out of the chamber and we can continue cycling these steps until our synthesized material is of an appropriate thickness. The methodology of ALD, relying on chemical reactions between adsorbed monolayers of precursor vapours, presents an inherent limitation on the growth rate of films which is an incredible blessing for the fabrication of NEMS cantilevers. The cyclical nature of ALD inherently entails a very slow material deposition rate and allows extremely precise control over the thickness of films, which should bode well for repeatability between runs. ALD is also excellent at creating uniform films since deposition is broken into multiple steps whereby we have the luxury to wait until the entire wafer has undergone precursor adsorption before proceeding with the subsequent reaction. This uniformity will result in excellent uniformity of stress and thickness over a wafer, so that NEMS devices that are made from the same wafer will exhibit a very low deviation in device performance.

A review of literature reveals very few papers in the intersection of ALD and MEMS and NEMS. The application of ALD has been mainly limited to surface modification of MEMS devices that are made out of conventional materials. There were only a few papers that used ALD films as the basis for micro and nano-resonant cantilevers (229; 230; 231), all of which concentrated on Al_2O_3 as structural material. Aside from this, there has been some work on applying ALD materials as a cladding layer for cantilever transducers. Waggoner *et al.*

Table 6.1: Mechanical properties for CVD synthesized Nitrides and Oxides (1)

Material name	Density $\frac{g}{cm^3}$	Coeff. of thermal expansion $\frac{10^{-6}}{^{\circ}C}$	Young's mod. GPa
TiN	5.4	9.35	251
Al ₂ O ₃	3.965	7.0 - 8.3	378
Si ₃ N ₄	3.18	2.8 - 3.2	260 - 330

(232) have also applied ALD SiO₂ as a cladding layer to improve silanization and bioaffinity of LPCVD Si₃N₄ resonant cantilever transducers.

While technically poorer than Al₂O₃ as a resonant NEMS material, the material properties of TiN are nonetheless promising for the development of NEMS sensors. TiN is typically employed as a coating on machine tools such as drill bits to improve durability and corrosion resistance. In microelectronics ALD TiN can be used as a gate electrode to interface with Hafnium based gate insulators since TiN is conductive and is effective at preventing Cu diffusion into the gate oxide (233; 112). The main advantage that TiN would have over Al₂O₃ is that it is much more resistant to attack by etchants like KOH and HF that are commonly used to remove sacrificial layers in NEMS fabrication (234). Specifically TiN would enable the fabrication of low-undercut NEMS beams using a KOH release, as applied previously by our group (33). In this study we employ an Oxford FlexAL ALD system with a temperature controlled chuck (up to 400°C) and a remote plasma system which is capable of Al₂O₃, TiO₂, and TiN film deposition.

The plasma assisted ALD deposition recipe used to synthesize TiN in this chapter is provided in table 6.2. The TiCl₄ precursor is introduced into the chamber by releasing a trapped volume of TiCl₄ vapour that was generated from a bubbler containing liquid TiCl₄. The chamber is then purged of excess precursor to ensure that TiN formation only takes place at the substrate surface and not above it. H₂ and N₂ gas flow is started and allowed to stabilize before a plasma is lit. The H₂:N₂ plasma ions react with the adsorbed TiCl₄

Table 6.2: ALD TiN deposition recipe used in this chapter. All films were deposited for 3000 cycles.

Deposition step name	Time s	Pressure mTorr	Power W	Ar flow sccm	H ₂ flow sccm	N ₂ flow sccm
TiCl ₄ Dose	0.03	80	N/A	60	0.1	0.1
TiCl ₄ Purge	1.5	80	N/A	60	0.1	0.1
Gas stabilize	6.5	15	N/A	0.1	40	2
Plasma	20	20	300	0.1	40	2
Plasma purge	5	N/A	N/A	0.1	0.1	0.1

to form TiN, and unreacted H₂ and N₂ gas is pumped out of the chamber.

Five ALD films were synthesized for the work presented in this chapter. All ALD films were grown on <100> silicon prime wafers that were cleaned in a 15 min piranha bath (3H₂SO₄ : 1H₂O₂) prior to deposition. TiN films were synthesized at deposition temperatures of 120°C, 160°C, 200°C, 250°C and 300°C.

6.3 Film Thickness and Deposition Rates

The first step in characterizing the ALD TiN films was to determine the deposition rate of the material per ALD cycle. For films below 100 nm in thickness, the poor resolution of stylus profilometry becomes a significant source of error in thickness measurement and optical methods would provide a better solution. One could use white light interferometry to measure the step height of an opaque film, but TiN isn't opaque thus, optical reflectometry and ellipsometry are more appropriate solutions.

In optical reflectometry, a light is shone through the thin film reflecting back off the substrate and the reflected intensity of the light is recorded for a series of wavelengths. This intensity spectra can then be used to determine the film thickness given the index of refraction of the material over those wavelengths. Ellipsometry is a more powerful tool whereby a linearly polarized beam is

reflected off of the film / substrate interface which changes the polarization state of the light. The resulting p- and s-polarized intensities as well as the phase difference are measured. Ellipsometry can be extremely accurate at measuring the thicknesses of films from hundreds of nanometres down to the <10 nm regime.

Once the films were deposited on the Si wafers, they were taken to a filmetrics reflectometer to determine the film thickness over 13 points. The filmetrics TiN model was found to yield best fits over the wavelength window of 550 - 800 nm. Thickness data was taken over 13 points and error bars were generated from standard error calculations.

The reflectometry data only fit well over a rather narrow wavelength window (550 - 800 nm) so ellipsometry measurements were also performed to ensure that the thickness data was accurate. To this end, spectroscopic ellipsometry data was taken with a J.A. Woolam variable angle spectroscopic ellipsometer. Spectroscopic ellipsometry has been successfully employed in literature to determine the thickness of ALD deposited TiN films (233; 235; 236). Spectroscopic ellipsometry measurements were taken at angles 55° , 65° and 75° over the wavelength range of 300 nm - 1350 nm at a 10 nm wavelength resolution. A Drude-Lorentz model was then constructed along the lines of models described by Langereis *et al.* (235; 236). The data was fitted to the Drude-Lorentz model using the VASE software. In fitting the data, we sought to minimize mean square error of the fit while avoiding simultaneous fitting of parameters with a correlation factor above 0.9 (this would hinder convergence). Films deposited at 200°C and below were modelled with one Drude and one Lorentz oscillator, while films deposited at 250°C and 300°C were modelled with one Drude and two Lorentz oscillators. Measurements were taken from five points on each wafer and error bars were generated from standard error calculations.

Figure 6.1 is a graph of the film thickness of 3000 cycles of ALD TiN deposited on Si at various temperatures. The reflectometry and ellipsometry data yield very similar results indicating that ALD film synthesis efficiency improves dramatically with increased substrate temperature. The deposition rate varies

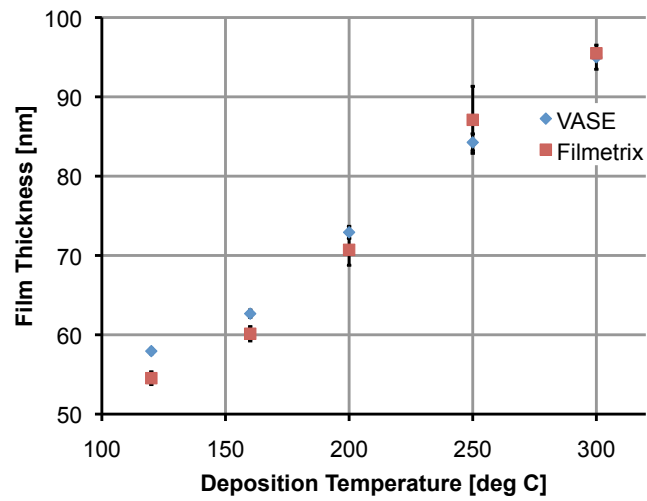


Figure 6.1: Thickness of 3000 cycle TiN films deposited at different temperatures. Red squares are measurements taken with a filmetrics reflectometer and blue lozenges are measurements taken with a spectroscopic ellipsometry.

from as low as $0.193 \frac{\text{\AA}}{\text{cycle}}$ at 120°C substrate temperature to $0.317 \frac{\text{\AA}}{\text{cycle}}$ at 300°C . Heil *et al.* (233) also observed very similar deposition rates (through in situ ellipsometry in a home-built ALD system) as ALD synthesis temperature was varied.

6.4 Film Stress

A constant theme in nanofabrication is the need to understand and control film stresses. In nanomechanical cantilevers, stress should be quantified so that cantilever structures won't deform, aiming for stress as close to zero as possible. In the case of nanobeam resonators stress must be managed so that beams do not undergo destructive buckling (due to any compressive stress) or delamination (due to excessive tensile stress overcoming film adhesion). To this end the stress of the TiN films was measured by a flexus 2320 thin film stress measurement system. TiN film thicknesses were input as 100 nm initially, then corrected using the following equation.

$$\sigma_{actual} = \sigma_{measured} \left(\frac{h_{measured}}{h_{actual}} \right) \quad (6.1)$$

As stated in previous chapters, stress in deposited films can be due to a number of sources such as thermal mismatch stress or intrinsic stress due to sources such as lattice mismatch. ALD TiN film synthesis requires an elevated temperature for film deposition, so we expect thermal mismatch stress to be a significant source of stress. Equation 6.2 is a model for thermal mismatch stress of a deposited film, given E and ν are temperature independent (145).

$$\sigma_{th} = \frac{E_{film}}{1 - \nu_{film}} \int_{T_{amb}}^{T_{dep}} \alpha_{film} - \alpha_{sub} dT \quad (6.2)$$

Figure 6.2 is a graph of stress of ALD deposited TiN films as a function of deposition temperature. The blue lozenges represent the measured stress which

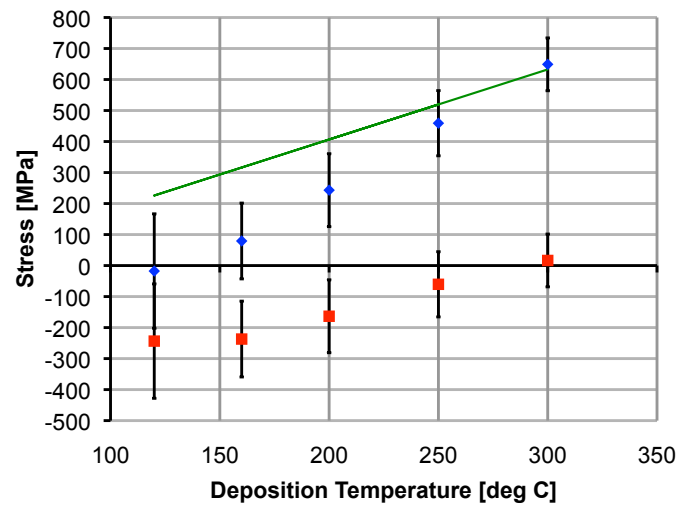


Figure 6.2: Stress of ALD deposited TiN films by deposition temperature. Blue lozenges represent the measured stress while the green line is the ideal stress due to thermal mismatch. The red squares represent stress not due to thermal mismatch sources.

increases significantly with deposition temperature. The green line in figure 6.2 is the thermal mismatch stress of the films calculated using equation 6.2 and assuming that the temperature coefficient of expansion is temperature invariant over the temperature range of 20° - 300° . The red squares on the graph are the measured stress minus the thermal mismatch stress, which gives the intrinsic stress of the film. We can see that thermal mismatch stress is indeed a significant source of film stress and that the TiN films would be intrinsically compressive but for the thermal mismatch in the deposition process. The measured stress of the 120°C film is nearly zero and would be suitable for the machining of single clamped cantilever structures. The tensile stress state of the rest of the films makes them suitable candidates for the fabrication of doubly clamped beam resonators as tensile stresses are known to improve the quality factor of such structures. In subsequent fabrication steps the film deposited at 200°C was chosen for prototyping, since it showed tensile stress which is not so strong as to cause film delamination upon machining.

6.5 X-Ray Diffraction

X-ray diffraction (XRD) scans were conducted to determine the crystalline structure of the ALD TiN films to see if they would be suitable for resonant nanocantilever structures. The yield of single crystal silicon resonators is known to be dramatically reduced as their lateral dimensions are reduced below 50 nm (107). Glassy materials such as SiCN (136) and materials with small grain size are preferred since they do not provide significant intragranular propagation of defects that lead to brittle failure.

XRD measurements of the five ALD TiN films were conducted on a Bruker D8 X-ray diffractometer and showed peaks corresponding to the underlying Si $\langle 100 \rangle$ wafer very prominently. $\langle 200 \rangle$, $\langle 220 \rangle$, $\langle 311 \rangle$, $\langle 222 \rangle$, peaks of TiN were also visible with the $\langle 200 \rangle$ peak of TiN being most prominent. Heil *et al.* observed these peaks in 100°C and 400°C ALD TiN films using XRD, while Li *et al.* (237) observed (200) and (111) grains most commonly

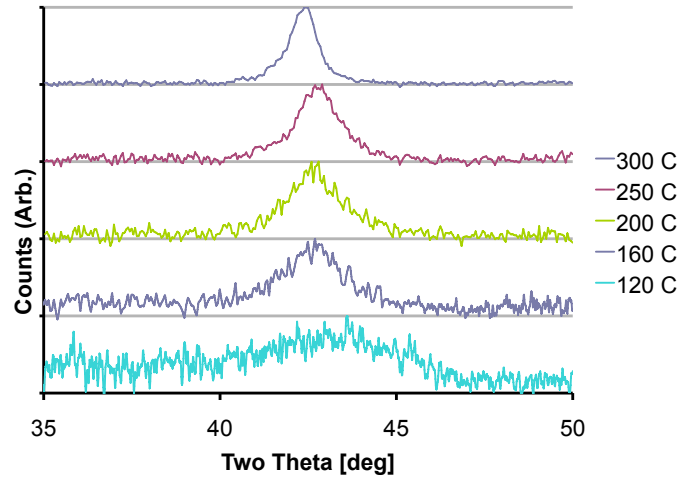


Figure 6.3: XRD scans of the $\langle 200 \rangle$ peak of TiN. This was the only peak in the XRD scan that could not be attributed to the Si wafer.

in their HRTEM studies of ALD TiN grain boundaries. Figure 6.3 shows the XRD curves corresponding to the amplitude normalized peaks of the $\langle 200 \rangle$ plane of TiN film deposited at various temperatures. It is evident that as the deposition temperature is increased, the $\langle 200 \rangle$ peak becomes more narrow and sharply defined. Scherrer's formula (equation 6.3) correlates XRD peak broadening with grain size of the material.

$$t = \frac{0.9\lambda}{FWHM_{peak} \cdot \cos(\theta_{peak})} \quad (6.3)$$

Peak broadening may also be due to instrumental broadening or inhomogeneous strain, but this analysis will neglect those effects. A gaussian fitting algorithm was used to determine the FWHM and angle of the XRD peaks, which was applied to Scherrer's formula to generate the $\langle 200 \rangle$ crystallite sizes plotted in figure 6.4.

Figure 6.4 shows that as TiN deposition temperature is increased, we see larger

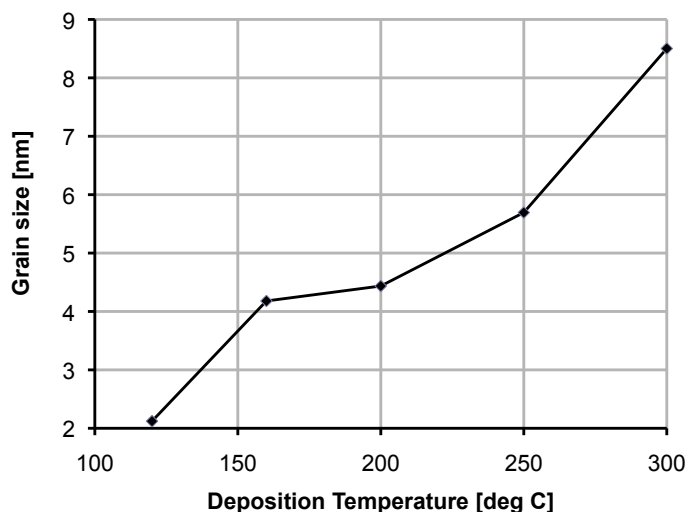


Figure 6.4: Crystallite size derived by application of Scherrer's formula to XRD scans of the $\langle 200 \rangle$ peak of TiN.

crystallite sizes in the $\langle 200 \rangle$ orientation. The grain size for all these films is around 10 nm or below. However, one must note that the films are not of uniform thickness and that the thinner dimensions of the low temperature TiN films would limit its ability to contain very thick crystal grains. This should have a fairly modest effect on lowering the average grain size for thinner films, since grain size in all films is 10 (or more) times smaller than the film thickness. We would like to avoid films with large crystal grains for beam nanoresonator applications. Thus the XRD data indicates that the TiN films grown at low temperature should be best suited for nanoresonator fabrication.

6.6 X-Ray Photoelectron Spectroscopy

X-ray photoelectron spectroscopy (XPS) was conducted to determine the elemental composition of the ALD TiN material as a function of deposition temperature. The mechanism by which XPS operates was explained previ-

Table 6.3: ALD TiN composition as determined by X-ray photoelectron spectroscopy. Note that as Temperature is increased Ti / N ratio approaches 1.

Deposition temp. °C	O %at.	Ti %at.	N %at.	C %at.	Cl %at.	Ti / N ratio unitless
120	28.9	30.0	20.6	8.1	12.4	1.46
160	29.3	31.1	21.2	7.9	10.4	1.47
200	27.0	31.9	22.9	8.7	9.5	1.39
250	25.7	32.1	26.0	8.5	7.8	1.24
300	22.6	34.5	31.4	7.0	4.6	1.10

ously in chapter 5. To accurately determine the elemental composition of the film material, the first few atomic layers were sputtered off with a 2 min Ar plasma before the XPS signal was assayed. This sputter cleaning was done to remove any adventitious C and excess O (due to unbound Ti near the surface binding with O from the laboratory environment). Table 6.3 is a summary of the atomic composition of the ALD synthesized TiN films, which is also illustrated in bargraph form in Figure 6.5.

In our XPS studies we observed three elemental contaminants i.e. O, Cl and C. XPS studies reveal that carbon contamination was relatively constant with deposition temperature and could be due to impurities in the vessels that contain the precursor material or in the ALD chamber. Table 6.3 and figure 6.5 also show that as the temperature is increased, oxygen and chlorine content in the ALD films decreases. We expect that chlorine in the film is entirely due to trapped and unreacted TiCl_4 precursor. The TiCl_4 is a precursor that is common to the ALD synthesis of both Ti and TiN materials and is directly related to the synthesis of Ti in our ALD films. We expected and confirmed that as Cl contamination is reduced, Ti signal is increased. Oxygen contamination in the film is due to the strong affinity of O to Ti (Ti can be used as a getter material in PVD systems for this reason) and thus exposed Ti surfaces in the ALD system will react to any O present. An increased deposition rate will mean that a given Ti atom is exposed to the ALD vessel environment for less

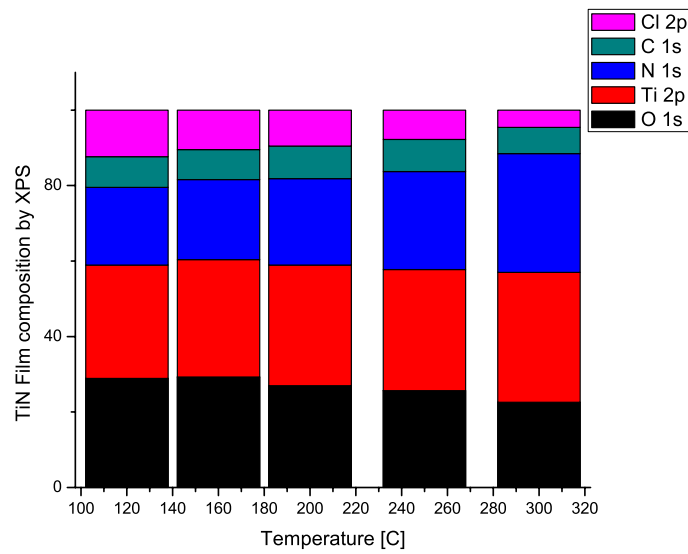


Figure 6.5: Bargraph of TiN film composition by temperature. As temperature increases we see a decrease in O and Cl and an increase in N. Cl is attributed to unreacted TiCl_4 precursor and O is attributed to oxidation of unreacted Ti.

time and thus we expect and indeed observe that as deposition temperature is increased (increasing deposition rate), oxygen contamination is reduced. Water vapour adsorbed on the sidewalls of the ALD reactor could also be another source of O contamination and higher process temperature will also ensure efficient removal of these vapours during pumpdown of the chamber.

The two non-contaminant species in our film are Ti and N. As stated previously, Ti synthesis is dependant on the reduction of the TiCl_4 precursor, which takes place with slightly improved efficiency at higher temperatures. The more prominent change in TiN composition is the vastly increased N content at higher temperatures. The Ti / N ratio goes from 1.46 at 120°C to 1.10 at 300°C due to the improved TiN synthesis in the plasma step.

High resolution XPS data was inspected to give further insight into the binding state of the atoms in the TiN films (221). Figure 6.6 gives a series of high resolution XPS plots for Ti, N, O and Cl. The high resolution XPS of the Ti 2p orbital shows a strong peak at 455 eV with a shoulder at 458 eV. These peaks also appear to have doublets approximately 6.1 eV higher (238), which has been observed previously for Ti and TiCl_4 XPS scans (239). The Ti $2p_{3/2}$ peak is typically located at 454 eV whereas TiN is expected to be slightly higher at 455 eV, which is approximately where this peak was observed. This most prominent Ti $2p_{3/2}$ peak is likely attributable to the presence of TiN and a small amount of metallic Ti. The presence of the 458 eV shoulder can be attributed to the presence of TiO_2 and/or TiCl_4 , which should decrease with increasing temperature.

The high resolution scan of N shows a 1s orbital peak at 397 eV which increases with increased temperature and consistent with the presence of TiN (239). The high resolution scan for oxygen shows a 1s orbital peak around 530 eV consistent with the presence of generic metal oxides (221) such as TiO_2 (239). The oxygen in the TiN films is clearly attributable to the presence of TiO_2 , which decreases at higher temperatures. The chlorine high resolution scan shows the Cl $2p_{3/2}$ doublet at 198 eV which has also been observed for TiCl_4 (238). All of these scans are consistent with the presence of TiO_2 and TiCl_4

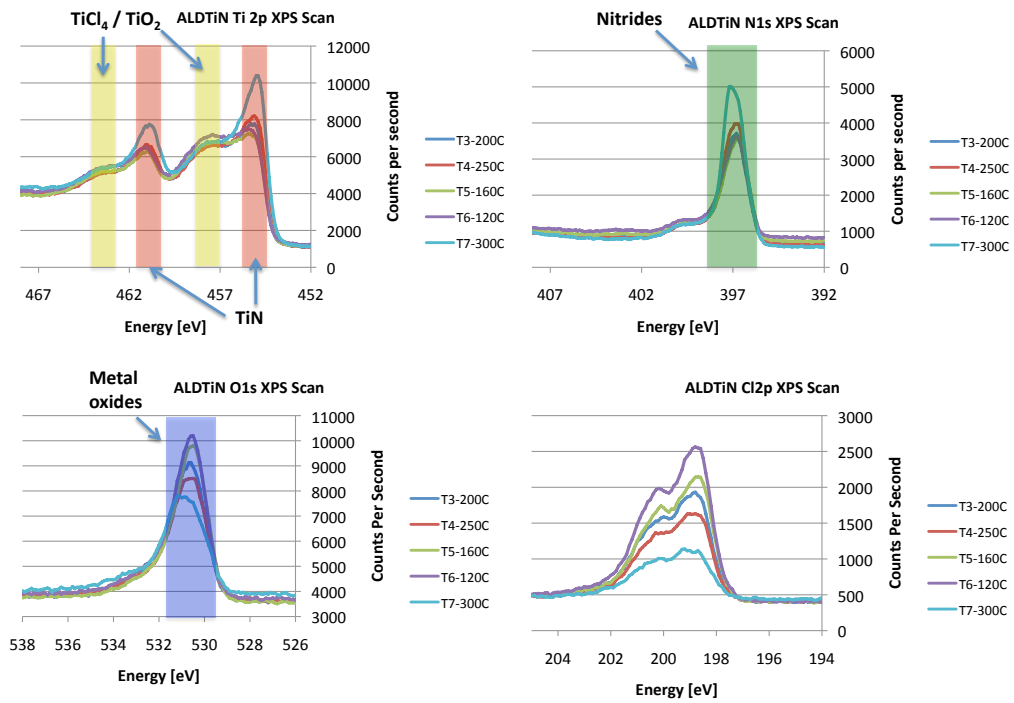


Figure 6.6: High resolution XPS spectra of ALD synthesized TiN films.

as the main impurities in the TiN films and none of the high resolution XPS peak features are inconsistent with this conclusion.

6.7 Cantilever Resonator Fabrication

The fabrication of TiN nanobeam resonators was conducted using a surface machining methodology very similar to that described in Figure 2.3 and in chapter 3 for SOI cantilever resonators. The substrates of ALD TiN film deposited at 200°C were cleaved into approximately 1 cm x 1 cm dies and cleaned with isopropyl alcohol to gently remove organics (piranha solution will etch TiN quickly). The samples were then dehydrated on a hot plate at 200°C for 5 min in the ambient atmosphere of a class 10 environment. A 60 nm thick polymethylmethacrylate (PMMA) 495K electron beam resist was spun and then baked at 180°C for 30 min. This step was repeated with a 60 nm thick PMMA 950K resist, creating a bilayer for lift-off. The substrates were patterned with a Raith150-TWO Electron Beam Lithography (EBL) system (10 kV, 10 μ m aperture, anchors defined as areas with dose 120 $\frac{\mu C}{cm^2}$, beams defined by single pixel line with dose 2500 $\frac{\mu C}{cm}$) and developed in a methylisobutylketone based developer (1 MIBK: 3 IPA). The application of single pixel line doses enabled the patterning of features narrower than 30 nm. The patterned resist is then subjected to a light O₂ “descum” plasma to smooth any roughness in the resist template resulting from nonideal developing. The patterned resist was then used to generate a 50 nm thick SiO₂ masking layer by electron beam evaporation and lift-off of the unexposed areas with an ultrasonic acetone bath.

The patterned TiN dies were then mounted on a Si wafer with vacuum grease, taken to an Oxford Plasmalab DRIE tool and subjected to a Cl₂ etch for 36 s at 20°C. Lemme *et al.* (240) demonstrated the etching of TiN in a similar reactor with a combination of Cl₂ and HBr gas chemistries. Previous etch testing determined the etch rate of the Cl₂ recipe to be 2.3 $\frac{nm}{s}$ + 4.9 nm for the strike step. After etching, the SiO₂ masking layer is removed by a 5

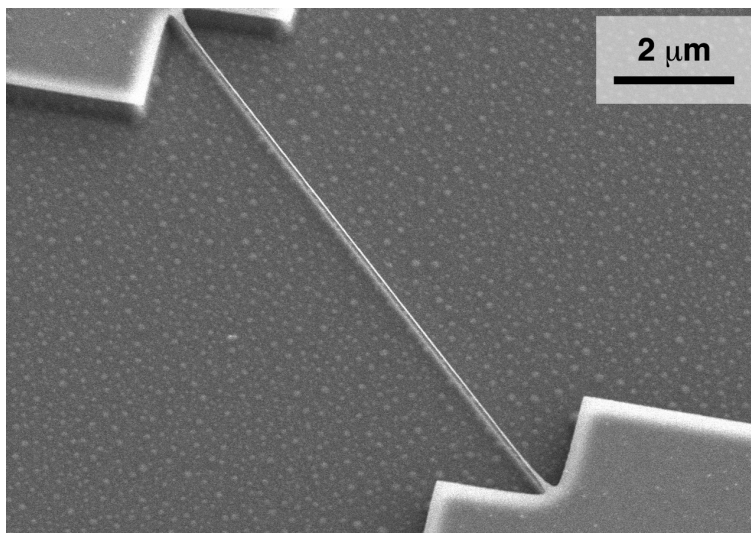


Figure 6.7: Scanning electron micrograph of a fabricated TiN beam resonator from the 200°C deposition run. Beam dimensions are 11.3 μm long, 30 nm wide and 72.9 nm thick.

min bath in BOE and the cantilever is released from the substrate using an isotropic SF_6 RIE release for 4 min. This release step is conceptually similar to the release step employed in chapter 5. Originally, a KOH etch release step was intended since it is highly anisotropic and thus minimizes clamping point undercut while it etches downwards quickly to avoid stiction when drying (33). However, SF_6 release was chosen for initial prototyping since it is a dry and relatively gentle process. The nanoresonator beams were imaged in SEM and a representative image of a fabricated beam is shown in figure 6.7.

Nanoresonator beams were fabricated with four different lengths (5.7 μm , 8.5 μm , 11.3 μm , 14.1 μm) using a single-pixel line exposure. The majority of the 5.7 and 8.5 μm beams survived fabrication, but few 11.3 μm and no 14.1 μm were successfully fabricated. We attempted to assay the resonance frequencies of the nanoresonator beams in an interferometric resonance testing setup (as described in section 2.7.1 and used in chapters 3 and 4). Unfortunately, due to time constraints and relative inexperience with such narrow line features no resonance data was acquired.

6.8 Summary

We explored the synthesis of TiN films using atomic layer deposition in order to fabricate nanoresonator beams. Atomic layer deposition (ALD) is conceptually similar to CVD technologies, except that film growth is broken into half-reactions that are alternated to form the desired material, rather than a constant reaction in the case of traditional CVD. ALD technologies yield very thin highly conformal films with fewer defects. As lateral dimensions for nanoresonators are scaled down below 10 nm, it is important to be able to synthesize films with well controlled thicknesses to enable reliable device machining. Additionally, the synthesis of extremely thin films will enable improved gravimetric sensitivity in resonant NEMS transducers.

To this end, TiN films were grown on silicon substrates at different deposition temperatures for 3000 cycles and were characterized using several thin film characterization tools. The film thicknesses were measured by reflectometry and variable angle spectroscopic ellipsometry to determine the film deposition rate per cycle. Film's stress was assessed by measuring wafer bowing with a laser interferometer. X-ray diffraction was performed to determine the crystal structure of the film and X-ray photoelectron spectroscopy was conducted to determine the elemental composition of the TiN films.

The TiN deposition rate increased significantly with substrate temperature from $0.193 \frac{\text{\AA}}{\text{cycle}}$ at 120°C to $0.317 \frac{\text{\AA}}{\text{cycle}}$ at 300°C . The stress of the ALD films went from near -17.7 MPa (compressive) for 120°C to 649.0 MPa (tensile) for 300°C . Thermal mismatch stress was associated with most of the increase in tensile stress. A simple model for thermal mismatch stress was used to subtract this effect from the measured stress revealing that the intrinsic stress of the TiN film does change with deposition temperature from -243.6 MPa (compressive) for 120°C to 16.5 MPa (tensile) for 300°C . X-ray diffraction revealed peaks corresponding to $\langle 200 \rangle$ crystallographic orientation with additional weaker peaks corresponding to $\langle 220 \rangle$, $\langle 311 \rangle$, and $\langle 222 \rangle$. The Scherrer formula was used to reveal that average crystallite size of the $\langle 200 \rangle$ crystals increased

dramatically with temperature, but remained smaller than 10 nm in all cases. High resolution XPS revealed that the TiN films suffered from significant Cl and O contamination which decreased as temperature was increased. The source of the Cl contamination was the TiCl_4 precursor, while O contamination is in the form of TiO_2 formed during film synthesis since Ti is a very effective getter material. As deposition temperature was increased N presence increased dramatically, the ratio of Ti / N went from 1.46 at 120°C to 1.10 at 300°C due to the vastly improved TiN synthesis in the plasma step.

Resonator beams were fabricated out of the 200°C TiN film. The 200°C composition was used due to its smaller crystallite size and its mildly tensile (~ 250 MPa) stress state. Beam structures were patterned in PMMA using single pixel line electron beam lithography and this pattern was used to deposit an SiO_2 mask using a liftoff process and electron beam evaporation. The pattern was transferred into the TiN with a Cl_2 RIE, masking layer was removed with a 5 min BOE bath and the TiN beam were released by etching away silicon below with a 4 min isotropic SF_6 RIE. The nanobeams were inspected with SEM and their yield decreased dramatically as beam length was increased. Resonance assaying was not performed due to time constraints. The fabrication of nanobeams based on ALD TiN materials was quite successful considering time constraints. ALD TiN is very light and elastically stiff making it a good candidate for a resonant transducer. Additionally the ALD process is inherently rate-limited in deposition, making the synthesis of ultrathin layers quite simple and repeatable compared to other CVD processes. TiN is also resistant to etching by KOH, so this method may be used in the future to release TiN nanobeams without significant undercut at clamping points. Ultimately, the low deposition rate and high uniformity of ALD deposited materials makes them ideal material candidates for the fabrication of large arrays of nanobeam resonators.

CHAPTER 7

A Summary and Outlook at Future Directions

7.1 Summary

This work demonstrated the application of gold-tantalum metal nanocomposite films for the fabrication of static microcantilever transducers. Metals have largely been overlooked for dynamic resonators due to their low elastic modulus, high density, polycrystalline nature, and large intrinsic sources of mechanical loss. Conversely, the sensitivity of a static cantilever transducer is very strongly dependant on its dimensions and less on its mechanical characteristics. The application of gold-tantalum as a structural material for these transducers confers a number of advantages. Firstly, the cantilever's top side is inherently sensitive to binding to thiol groups, enabling the application of a vast library of intermediate chemistries to sensitize these cantilever transducers for chemical and biological sensing applications. Secondly, the cantilever's backside is inherently inert to thiol binding due to the application of pure Ta as an adhesion layer, this simplifies cantilever transducer application by removing the need to subject the cantilever transducer's backside to a technically difficult blocking layer treatment. Thirdly, the demonstrated ability to control stress and fabricate cantilevers with an extremely high length to thickness ratio makes the compliance of these cantilevers (and thus their sen-

sitivity to surface stresses) among the most sensitive in known literature. As a proof of concept, these transducers were applied to detect the presence of self-assembled monolayers of dodecanethiol. Self-assembled monolayers are commonly used as an intermediate layer enabling functionalization of a cantilever transducer to its desired analyte (97; 98; 15; 205). Using white light interferometry we determined that the assembly of dodecanethiol on Au-5% at. Ta cantilevers caused a deflection that corresponded to $1.07 \frac{N}{m}$, a stress comparable to that observed by previous investigators who used traditional Au coated Si or Si₃N₄ cantilevers.

First, cantilever fabrication and resonance testing was explored in silicon using SIMOX wafers. Silicon is a commonly used material for cantilever transducers since it is light, stiff, and has a plethora of technologies available for its machining. Since the speed of sound ($\sqrt{\frac{E}{\rho}}$) of a material can be inferred from the resonance of a cantilever structure using the Euler-Bernoulli equation, we chose to test this analysis on single crystal silicon before applying this technique to determine the stiffness of our gold-tantalum materials. In machining silicon nanocantilevers we developed electron beam lithography techniques that would be applied throughout this thesis, and demonstrated the use of a novel cryogenic etching technique.

Secondly, we applied co-sputtering to synthesize a series of films of gold-tantalum nanocomposite alloy films. We assessed the film structure with varying Ta content using atomic force and scanning electron microscopy as well as X-ray diffraction. Film conductivities were assessed with four-point probe measurements. Hardness and elastic modulus were measured with nanoindentation. Deposited film stress was measured with an interferometer, and a low stress composition was identified at Au-5 at.% Ta. The XRD data indicated that below 50 at.% Ta the FCC structure of gold is retained with a very strong $\langle 111 \rangle$ orientation, indicating that these films should still have an affinity for thiolized molecules. The films exhibited an increased elastic modulus and hardness as well as a significant grain size reduction with the introduction of tantalum. Cantilevered resonators constructed out of Au-5 at.% Ta were man-

ufactured and their fundamental resonance frequencies were assessed. These measurements indicated that the speed of sound in the Au-5 at.% Ta was $2406 \frac{m}{s}$. The observed Q factors of the resonators ranged from 304 to 640 at room temperature, and up to 10000 when cooled to 77 K. Finite element analysis was also performed and corroborated the resonance frequencies measured and speed of sound extracted through application of the Euler-Bernoulli PDE.

Thirdly, we endeavoured to determine the effect incorporated Ta would have on the film's affinity for alkanethiol molecules and if appropriate, fabricate static cantilever transducers out of low stress Au-5 at.% Ta material. We performed contact angle measurements, x-ray photoelectron spectroscopy and fourier transform infrared spectroscopy to determine the presence of dodecanethiol on a series of Au-Ta composition films. We indeed observed that there was reduced but significant thiol binding on Au-Ta films until Ta content reaches 20% at. Commercially sourced silicon microcantilevers were coated with the same series of Au-Ta compositions and the stress imparted by exposure to dodecanethiol was measured. The silicon microcantilevers underwent measurable compressive stress due to dodecanethiol exposure which decreased with increasing Ta in the Au-Ta coating film until no stress was detectable for films with 20% at. Ta and above. We fabricated Au-Ta static microcantilever transducers with spring constants as low as $10.5 \frac{mN}{m}$ using the low-stress Au-5 at.% Ta material. These highly compliant Au-Ta cantilever transducers were exposed to dodecanethiol vapours for two hours and underwent deflection corresponding to a $1.07 \pm 0.09 \frac{N}{m}$ surface stress.

Lastly, we fabricated and characterized nanoresonant beams machined from ALD synthesized thin films. The rate limitation, uniformity, lightness and stiffness of ALD synthesized materials makes them ideal for the fabrication of resonant nanobeam transducers with superior gravimetric sensitivity. TiN was grown on silicon wafers at different temperatures between 120°C and 300°C. The films' thicknesses were measured by reflectometry and ellipsometry. Film stresses were determined by measuring the silicon wafer bowing with an interferometer. XRD and XPS were conducted to ascertain information about the

films' crystallinity and chemical composition respectively. We observed that as synthesis temperature was increased, film thickness and stress increased markedly. Film thickness increased due to increased TiN synthesis efficiency and film stress increased mainly due to thermal mismatch stress (with a small contribution from increased intrinsic stress). XRD data showed that the TiN grew preferentially in the $\langle 200 \rangle$ direction and an application of Scherrer's formula showed that there was a significant increase in crystallite size with increased deposition temperature. XPS analysis showed that the primary contaminants in the films were O, C, and Cl, of which O and Cl contamination was reduced with increased deposition temperature. Additionally, the Ti / N ratio went from 1.46 to 1.10 as deposition temperature was increased from 120°C to 300°C, indicating improved TiN synthesis efficiency at higher temperatures. Nanobeam resonators were fabricated out of the 200°C TiN film, however time constraints limited the ability to assay the resonance frequencies of these devices.

7.2 Future Directions

There are still some avenues for improvement of the Au-Ta static cantilever transducer designs. Most obviously the cantilever dimensions could be modified to increase sensitivity by increasing the cantilever length and decreasing its thickness. In order to increase these dimensions it is imperative to control the mean and gradient stress of the deposited Au-Ta. An in situ stress monitoring system like the k-space kSA 400 could be used in the sputter chamber to monitor the stress state of the deposited film so that we would have a more accurate value for the stress state of thinner Au-Ta films, and could make adjustments to stoichiometry to further reduce mean and gradient stresses.

A major inconvenience in the synthesis of Au-Ta nanocomposites is maintaining accurate deposition rate and stoichiometry data. As a magnetron sputter target is depleted, a "racetrack" pattern forms on the sputter target where electron confinement by the magnetron causes the majority of the sputtering

to take place. This “racetrack” pattern increases the surface area of the target in this high yield area and thus increases the sputter rate. To mitigate this effect rates were recalculated and power-stoichiometry relationships were recalibrated approximately every 30-60 minutes of gold sputter time (since most films were predominantly gold). A simple solution to this problem would be the inclusion of crystal thickness rate monitors and substrate shutters so that deposition rates could be determined on every sputter run and power-stoichiometry relationship could then be computed, ensuring more accuracy in designed stoichiometry.

One major design improvement would be to utilize a bulk machining methodology to fabricate the Au-Ta cantilever transducers. Bulk machining would allow us to fabricate cantilever transducers without an Si substrate underneath, allowing easier application of these transducers in liquid environments without concerns about stiction when drying the cantilevers during pretreatments or experiments. We had explored bulk machining of Au-Ta with TMAH, but there were many complications with regards to synthesizing a masking layer that would withstand the etch times required. However, one could use a different approach by applying bulk machining techniques to fabricate a cantilever out of a sacrificial material like highly doped Si or SiO₂, deposit the Au-Ta mechanical layer and finally remove the sacrificial cantilever with RIE, XeF₂, HF vapour or wet etch techniques. This would be a great improvement in the ruggedness of the Au-Ta cantilever design.

One last improvement in the fabrication of Au-Ta cantilevers that could be explored would be the fabrication of a cantilever structure that simplifies laser spot alignment in an AFM style readout system. Many commercial cantilever readout systems operate by this method, and AFM style readouts are able to operate with the cantilever in a liquid environment. As stated previously, the biggest weakness with these split photodiode setups for static cantilever readout is that it is difficult to accurately and reliably place the laser spot on the same location of the cantilever which leads to errors in translating the cantilever deflection to a surface stress value. Some investigators have

used triangular cantilevers for this reason because the intersection of the two cantilever arms near the apex is rather simple to locate reliably. However triangular cantilever designs are stiffer than similarly dimensioned rectangular cantilevers, lowering their sensitivity. Ideally for this design, one would fabricate a cantilever geometry whereby the cantilever is much narrower than the beam spot, but has a dramatically wider paddle near its tip. A camera in the AFM setup could be used to locate the laser spot on this paddle reliably, significantly reducing the uncertainty in the beam spot location.

In summary, in situ stress and deposition rate measurement abilities would improve the consistency of the cantilever's physical properties enabling more stress sensitive designs. Bulk machining methodologies could be pursued to improve the applicability and robustness of the Au-Ta cantilever devices. Triangular or paddle cantilever designs would then be useful to improve the ability to readout cantilever deflection with AFM type setups, which are common in commercial cantilever transducer platform like the Concentris Cantisens CSR-801.

Bibliography

- [1] H. O. Pierson, *Handbook of chemical vapor deposition (CVD) : principles, technology, and applications*. Norwich, NY : Noyes Publications, 2nd ed., 1999.
- [2] M. Ratner and D. Ratner, *Nanotechnology: A Gentle Introduction to the Next Big Idea*. Prentice Hall, 2002.
- [3] R. P. Feynman, “There’s plenty of room at the bottom [data storage],” *J Microelectromech S*, vol. 1, no. 1, pp. 60–66, 2002.
- [4] J. D. Watson and F. H. C. Crick, “Molecular structure of nucleic acids: A structure for deoxyribose nucleic acid (reprinted from nature, april 25, 1953),” *Nature*, vol. 224, pp. 470–471, 1969.
- [5] M. C. Roco, “National nanotechnology initiative: The initiative and its implementation plan,” *National Science and Technology Council Committee on Technology Subcommittee on Nanoscale Science, Engineering and Technology*, vol. 30, no. 2.10, p. 2000, 2002.
- [6] G. Binnig, H. Rohrer, C. Gerber, and E. Weibel, “Tunneling through a controllable vacuum gap,” *Appl Phys Lett*, vol. 40, no. 2, pp. 178–180, 1982.
- [7] A. Ulman, “Formation and structure of self-assembled monolayers,” *Chem Rev*, vol. 96, no. 4, pp. 1533–1554, 1996.

- [8] J. Chai and J. M. Buriak, "Using cylindrical domains of block copolymers to self-assemble and align metallic nanowires," *ACS Nano*, vol. 2, no. 3, pp. 489–501, 2008.
- [9] X. Zhang, K. D. Harris, N. L. Y. Wu, J. N. Murphy, and J. M. Buriak, "Fast assembly of ordered block copolymer nanostructures through microwave annealing," *ACS Nano*, 2010.
- [10] A. J. Murray, "Synthesis of tungsten trioxide thin films for gas detection," Master's thesis, University of Alberta, Oct 2009.
- [11] M. Lau, L. Dai, K. Bosnick, and S. Evoy, "Synthesis and characterization of tio_x nanowires using a novel silicon oxide support layer," *Nanotechnology*, vol. 20, p. 025602, 2009.
- [12] M. Belov, N. J. Quitariano, S. Sharma, W. K. Hiebert, T. I. Kamins, and S. Evoy, "Mechanical resonance of clamped silicon nanowires measured by optical interferometry," *J Appl Phys*, vol. 103, p. 074304, Jan 2008.
- [13] N. J. Quitariano, M. Belov, S. Evoy, and T. I. Kamins, "Single-crystal, silicon nanotubes, and their mechanical resonant properties," *Nano lett*, vol. 9, no. 4, pp. 1511–1516, 2009.
- [14] J. J. Ramsden, "Biomimetic protein immobilization using lipid bilayers," *Biosens Bioelectron*, vol. 13, pp. 593–598, Jan 1998.
- [15] L. Gervais, M. Gel, B. Allain, M. Tolba, L. Brovko, M. Zourob, R. Mandeville, M. Griffiths, and S. Evoy, "Immobilization of biotinylated bacteriophages on biosensor surfaces," *Sensor Actuat B-Chem*, vol. 125, no. 2, pp. 615–621, 2007.
- [16] A. Singh, N. Glass, M. Tolba, L. Brovko, M. Griffiths, and S. Evoy, "Immobilization of bacteriophages on gold surfaces for the specific capture of pathogens," *Biosens Bioelectron*, vol. 24, no. 12, pp. 3645–3651, 2009.

- [17] D. M. Eigler and E. K. Schweizer, "Positioning single atoms with a scanning tunnelling microscope," *Nature*, vol. 344, no. 6266, pp. 524–526, 1990.
- [18] M. F. Crommie, C. P. Lutz, and D. M. Eigler, "Confinement of electrons to quantum corrals on a metal surface," *Science*, vol. 262, no. 5131, pp. 218–220, 1993.
- [19] R. D. Piner, J. Zhu, F. Xu, S. Hong, and C. A. Mirkin, "dip-pen' nanolithography," *Science*, vol. 283, no. 5402, p. 661, 1999.
- [20] G. E. Moore, "Cramming more components onto integrated circuits," *Electronics*, vol. 38, no. 8, pp. 82–85, 1965.
- [21] S. D. Senturia, *Microsystem design*. Boston : Kluwer Academic Publishers, 2001.
- [22] M. Elwenspoek and R. Wiergerink, *Mechanical Microsensors*. Springer, 2001.
- [23] "ADXL312 datasheet," tech. rep., Analog Devices, Dec 2010.
- [24] "Spatial light valve datasheet," tech. rep., Micralyne, Jun 2010.
- [25] "DLP5500 datasheet," tech. rep., Texas Instruments, Jun 2010.
- [26] H. Becker and L. E. Locascio, "Polymer microfluidic devices," *Talanta*, vol. 56, no. 2, pp. 267–287, 2002.
- [27] G. Binnig, C. F. Quate, and C. Gerber, "Atomic force microscope," *Phys Rev Lett*, vol. 56, no. 9, pp. 930–933, 1986.
- [28] J. Sit, *ECE 558 Course Notes*. University of Alberta, 2006.
- [29] G. Binnig, C. Gerber, E. Stoll, T. R. Albrecht, and C. F. Quate, "Atomic resolution with atomic force microscope," *Surf Sci*, vol. 189, pp. 1–6, 1987.

- [30] L. Gross, F. Mohn, N. Moll, P. Liljeroth, and G. Meyer, "The chemical structure of a molecule resolved by atomic force microscopy," *Science*, vol. 325, pp. 1110–1114, Aug 2009.
- [31] B. Ilic, D. Czaplewski, M. Zalalutdinov, H. G. Craighead, P. Neuzil, C. Campagnolo, and C. Batt, "Single cell detection with micromechanical oscillators," *J Vac Sci Technol B*, vol. 19, no. 6, pp. 2825–2828, 2001.
- [32] B. Ilic, Y. Yang, and H. G. Craighead, "Virus detection using nanoelectromechanical devices," *Appl Phys Lett*, vol. 85, no. 13, p. 2604, 2004.
- [33] L. M. Fischer, V. A. Wright, C. Guthy, N. Yang, M. T. McDermott, J. M. Buriak, and S. Evoy, "Specific detection of proteins using nanomechanical resonators," *Sensor Actuat B-Chem*, vol. 134, no. 2, pp. 613–617, 2008.
- [34] B. Ilic, H. G. Craighead, S. Krylov, W. Senaratne, C. Ober, and P. Neuzil, "Attogram detection using nanoelectromechanical oscillators," *J Appl Phys*, vol. 95, p. 3694, 2004.
- [35] A. K. Naik, M. S. Hanay, W. K. Hiebert, X. L. Feng, and M. L. Roukes, "Towards single-molecule nanomechanical mass spectrometry," *Nat Nanotechnol*, vol. 4, no. 7, pp. 445–450, 2009.
- [36] S. Dutt, "Use of surfaces functionalized with phage tailspike proteins to capture and detect bacteria in biosensors," Master's thesis, University of Alberta, Jun 2010.
- [37] D. R. O'Connor, "Report of the walkerton inquiry," pp. 1–38, Jan 2002.
- [38] A. M. Wendel, D. H. Johnson, U. Sharapov, J. Grant, J. R. Archer, T. Monson, C. Koschmann, and J. P. Davis, "Multistate outbreak of escherichia coli O157:H7 infection associated with consumption of packaged spinach, august–september 2006: The wisconsin investigation," *Clin Infect Dis*, vol. 48, no. 8, pp. 1079–1086, 2009.

- [39] D. G. Maki, "Don't eat the spinach—controlling foodborne infectious disease," *New Engl J Med*, vol. 355, no. 19, p. 1952, 2006.
- [40] A. W. Martinez, S. T. Phillips, G. M. Whitesides, and E. Carrilho, "Diagnostics for the developing world: microfluidic paper-based analytical devices," *Anal Chem*, vol. 82, no. 1, pp. 3–10, 2010.
- [41] A. W. Martinez, S. T. Phillips, and G. M. Whitesides, "Three-dimensional microfluidic devices fabricated in layered paper and tape," *P Natl Acad Sci USA*, vol. 105, no. 50, p. 19606, 2008.
- [42] L. Senesac and T. G. Thundat, "Nanosensors for trace explosive detection," *Mater Today*, vol. 11, no. 3, pp. 28–36, 2008.
- [43] H. P. Lang, R. Berger, F. Battiston, J. P. Ramseyer, E. Meyer, C. Andreoli, J. Brugger, P. Vettiger, M. Despont, T. Mezzacasa, L. Scandella, H. J. Guntherodt, C. Gerber, and J. K. Gimzewski, "A chemical sensor based on a micromechanical cantilever array for the identification of gases and vapors," *Appl Phys A-Mater*, vol. 66, pp. 61–64, 1998.
- [44] Y. Yang, H. Ji, and T. Thundat, "Nerve agents detection using a Cu^{2+} /l-cysteine bilayer-coated microcantilever," *J Am Chem Soc*, vol. 125, no. 5, pp. 1124–1125, 2003.
- [45] X. Yan, Y. Tang, H. Ji, Y. Lvov, and T. Thundat, "Detection of organophosphates using an acetyl cholinesterase (ache) coated microcantilever," *Instrum Sci Technol*, vol. 32, no. 2, pp. 175–183, 2004.
- [46] H.-F. Ji, Y. Zhang, V. V. Purushotham, S. Kondu, B. Ramachandran, T. Thundat, and D. T. Haynie, "1,6-hexanedithiol monolayer as a receptor for specific recognition of alkylmercury," *Analyst*, vol. 130, p. 1577, Jan 2005.
- [47] D. Blowes, "Environmental chemistry: Tracking hexavalent Cr in groundwater," *Science*, vol. 295, pp. 2024–2025, Mar 2002.

- [48] C. K. O'Sullivan and G. G. Guilbault, "Commercial quartz crystal microbalances-theory and applications," *Biosens Bioelectron*, vol. 14, no. 8-9, pp. 663-670, 1999.
- [49] K. A. Marx, "Quartz crystal microbalance: A useful tool for studying thin polymer films and complex biomolecular systems at the solution surface interface," *Biomacromolecules*, vol. 4, no. 5, pp. 1099-1120, 2003.
- [50] J. Janata, M. Josowicz, and D. M. DeVaney, "Chemical sensors," *Anal Chem*, vol. 66, no. 12, pp. 207-228, 1994.
- [51] C. Kößlinger, E. Uttenthaler, S. Drost, F. Aberl, H. Wolf, G. Brink, A. Stanglmaier, and E. Sackmann, "Comparison of the QCM and the SPR method for surface studies and immunological applications," *Sensor Actuat B-Chem*, vol. 24, no. 1-3, pp. 107-112, 1995.
- [52] M. Ohring, *Materials science of thin films: deposition and structure*. San Diego, CA : Academic Press, 2nd ed., 2002.
- [53] G. Sauerbrey, "Verwendung von schwingquarzen zur wägung dünner schichten und zur mikrowägung," *Zeitschrift für Physik A Hadrons and Nuclei*, vol. 155, no. 2, pp. 206-222, 1959.
- [54] N. R. Glass, "Specific phage based bacteria detection using microcantilever sensors," Master's thesis, University of Alberta, Jun 2009.
- [55] H. Wohltjen and R. Dessy, "Surface acoustic wave probes for chemical analysis. I. introduction and instrument description," *Anal Chem*, vol. 51, no. 9, pp. 1458-1464, 1979.
- [56] K. Länge, B. E. Rapp, and M. Rapp, "Surface acoustic wave biosensors: a review," *Anal Bioanal Chem*, vol. 391, no. 5, pp. 1509-1519, 2008.
- [57] E. Benes, M. Gröschl, W. Burger, and M. Schmid, "Sensors based on piezoelectric resonators," *Sensor Actuat A-Phys*, vol. 48, no. 1, pp. 1-21, 1995.

- [58] H. Wohltjen and R. Dessy, "Surface acoustic wave probes for chemical analysis. II. gas chromatography detector," *Anal Chem*, vol. 51, no. 9, pp. 1465–1470, 1979.
- [59] H. Wohltjen and R. Dessy, "Surface acoustic wave probes for chemical analysis. III. thermomechanical polymer analyzer," *Anal Chem*, vol. 51, no. 9, pp. 1470–1475, 1979.
- [60] E. Benes, M. Groschl, F. Seifert, and A. Pohl, "Comparison between BAW and SAW sensor principles," *1997 IEEE International Frequency Control Symposium*, pp. 5–20, 1997.
- [61] J. Homola, S. S. Yee, and G. Gauglitz, "Surface plasmon resonance sensors: review," *Sensor Actuat B-Chem*, 1999.
- [62] J. Homola, S. S. Yee, and D. Myszka, *Optical Biosensors: Today and Tomorrow, Chapter 4: Surface plasmon resonance biosensors*. Elsevier B.V., 2nd ed., 2008.
- [63] H. Mukundan, A. S. Anderson, W. K. Grace, K. M. Grace, N. Hartman, J. S. Martinez, and B. I. Swanson, "Waveguide-based biosensors for pathogen detection," *Sensors*, vol. 9, no. 7, pp. 5783–5809, 2009.
- [64] J. D. Joannopoulos, P. R. Villeneuve, and S. Fan, "Photonic crystals: putting a new twist on light," *Nature*, vol. 386, pp. 143–149, 1997.
- [65] G. Anderson and C. R. Taitt, *Optical Biosensors: Today and Tomorrow, Chapter 2: Evanescent Wave Fiber Optic Biosensors*. Elsevier B. V., 2nd ed., 2008.
- [66] M. El-Sherif, *Optical Guided-Wave Chemical and Biosensors II*. Springer, 2010.
- [67] Y. Fang, A. M. Ferrie, N. H. Fontaine, J. Mauro, and J. Balakrishnan, "Resonant waveguide grating biosensor for living cell sensing," *Biophys J*, vol. 91, no. 5, pp. 1925–1940, 2006.

- [68] J. B. Jensen, P. E. Hoiby, G. Emiliyanov, O. Bang, L. H. Pedersen, and A. Bjarklev, "Selective detection of antibodies in microstructured polymer optical fibers," *Opt Express*, vol. 13, no. 15, pp. 5883–5889, 2005.
- [69] L. Rindorf, J. B. Jensen, M. Dufva, L. H. Pedersen, P. E. Høiby, and O. Bang, "Photonic crystal fiber long-period gratings for biochemical sensing," *Opt Express*, vol. 14, no. 18, pp. 8224–8231, 2006.
- [70] S. C. Buswell, V. A. Wright, J. M. Buriak, V. Van, and S. Evoy, "Specific detection of proteins using photonic crystal waveguides," *Opt Express*, vol. 16, no. 20, pp. 15949–15957, 2008.
- [71] Y. Fang, "Non-invasive optical biosensor for probing cell signaling," *Sensors*, pp. 1–14, 2007.
- [72] T. Thundat, P. I. Oden, and R. J. Warmack, "Microcantilever sensors," *Microscale Therm Eng*, 1997.
- [73] N. V. Lavrik, M. J. Sepaniak, and P. G. Datskos, "Cantilever transducers as a platform for chemical and biological sensors," *Rev Sci Instrum*, vol. 75, no. 7, p. 2229, 2004.
- [74] M. D. Ward and D. A. Buttry, "In situ interfacial mass detection with piezoelectric transducers," *Science*, vol. 249, no. 4972, pp. 1000–1007, 1990.
- [75] J. R. Barnes, R. J. Stephenson, C. N. Woodburn, S. J. O'Shea, M. E. Welland, T. Rayment, J. K. Gimzewski, and C. Gerber, "A femtojoule calorimeter using micromechanical sensors," *Rev Sci Instrum*, vol. 65, no. 12, pp. 3793–3798, 1994.
- [76] J. R. Barnes, R. J. Stephenson, C. N. Woodburn, S. J. O'Shea, M. E. Welland, T. Rayment, J. K. Gimzewski, and C. Gerber, "Erratum: A femtojoule calorimeter using micromechanical sensors [rev. sci. instrum. 65, 3793 (1994)]," *Rev Sci Instrum*, vol. 66, no. 4, p. 3083, 1994.

- [77] J. K. Gimzewski, C. Gerber, E. Meyer, and R. R. Schlittler, "Observation of a chemical reaction using a micromechanical sensor," *Chem Phys Lett*, vol. 217, no. 5-6, pp. 589–594, 1994.
- [78] T. Thundat, G. Y. Chen, R. J. Warmack, D. P. Allison, and E. A. Wachter, "Vapor detection using resonating microcantilevers," *Anal Chem*, vol. 67, no. 3, pp. 519–521, 1995.
- [79] G. Y. Chen, T. Thundat, E. A. Wachter, and R. J. W. Warmack, "Adsorption-induced surface stress and its effects on resonance frequency of microcantilevers," *J Appl Phys*, 1995.
- [80] C. D. Bain, E. B. Troughton, Y. T. Tao, J. Evall, G. M. Whitesides, and R. G. Nuzzo, "Formation of monolayer films by the spontaneous assembly of organic thiols from solution onto gold," *J Am Chem Soc*, vol. 111, no. 1, pp. 321–335, 1989.
- [81] N. Tillman, A. Ulman, and T. L. Penner, "Formation of multilayers by self-assembly," *Langmuir*, vol. 5, no. 1, pp. 101–111, 1989.
- [82] R. Berger, E. Delamarche, H. P. Lang, C. Gerber, J. K. Gimzewski, E. Meyer, and H. J. Güntherodt, "Surface stress in the self-assembly of alkanethiols on gold probed by a force microscopy technique," *Appl Phys A-Mater*, vol. 66, pp. 55–59, 1998.
- [83] M. Godin, P. J. Williams, V. Tabard-Cossa, O. Laroche, L. Y. Beaulieu, R. B. Lennox, and P. Grutter, "Surface stress, kinetics, and structure of alkanethiol self-assembled monolayers," *Langmuir*, vol. 20, pp. 7090–7096, 2004.
- [84] M. Godin, V. Tabard-Cossa, Y. Miyahara, T. Monga, P. J. Williams, L. Y. Beaulieu, R. B. Lennox, and P. Grutter, "Cantilever-based sensing: the origin of surface stress and optimization strategies," *Nanotechnology*, vol. 21, no. 7, p. 075501, 2010.

- [85] R. Desikan, S. Armel, H. M. Meyer, and T. Thundat, "Effect of chain length on nanomechanics of alkanethiol self-assembly," *Nanotechnology*, vol. 18, no. 42, p. 424028, 2007.
- [86] T. Thundat and L. Maya, "Monitoring chemical and physical changes on sub-nanogram quantities of platinum dioxide," *Surf Sci*, vol. 430, no. 1-3, pp. L546-L552, 1999.
- [87] X. M. H. Huang, M. Manolidis, S. C. Jun, and J. Hone, "Nanomechanical hydrogen sensing," *Appl Phys Lett*, vol. 86, no. 14, p. 143104, 2005.
- [88] D. Then, A. Vidic, and C. Ziegler, "A highly sensitive self-oscillating cantilever array for the quantitative and qualitative analysis of organic vapor mixtures," *Sensor Actuat B-Chem*, vol. 117, no. 1, pp. 1-9, 2006.
- [89] L. A. Pinnaduwege, H. F. Ji, and T. Thundat, "Moore's law in homeland defense: an integrated sensor platform based on silicon microcantilevers," *IEEE Sens J*, 2005.
- [90] B. Ilic, D. Czaplewski, H. G. Craighead, P. Neuzil, C. Campagnolo, and C. Batt, "Mechanical resonant immunospecific biological detector," *Appl Phys Lett*, vol. 77, p. 450, 2000.
- [91] A. Gupta, D. Akin, and R. Bashir, "Detection of bacterial cells and antibodies using surface micromachined thin silicon cantilever resonators," *J Vac Sci Technol B*, vol. 22, no. 6, p. 2785, 2004.
- [92] G. A. Campbell and R. Mutharasan, "Detection of pathogen escherichia coli O157:H7 using self-excited PZT-glass microcantilevers," *Biosens Bioelectron*, vol. 21, no. 3, pp. 462-473, 2005.
- [93] T. P. Burg, M. Godin, S. M. Knudsen, W. Shen, G. Carlson, J. S. Foster, K. Babcock, and S. R. Manalis, "Weighing of biomolecules, single cells and single nanoparticles in fluid," *Nature*, vol. 446, no. 7139, pp. 1066-1069, 2007.

- [94] J. L. Arlett and M. L. Roukes, “Ultimate and practical limits of fluid-based mass detection with suspended microchannel resonators,” *J Appl Phys*, vol. 108, no. 8, p. 084701, 2010.
- [95] A. Gupta, D. Akin, and R. Bashir, “Single virus particle mass detection using microresonators with nanoscale thickness,” *Appl Phys Lett*, vol. 84, no. 11, p. 1976, 2004.
- [96] K. M. Hansen, H. F. Ji, G. Wu, R. Datar, R. Cote, A. Majumdar, and T. Thundat, “Cantilever-based optical deflection assay for discrimination of DNA single-nucleotide mismatches,” *Anal Chem*, vol. 73, no. 7, pp. 1567–1571, 2001.
- [97] G. Wu, R. H. Datar, K. M. Hansen, T. Thundat, R. J. Cote, and A. Majumdar, “Bioassay of prostate-specific antigen (PSA) using microcantilevers,” *Nat Biotechnol*, vol. 19, no. 9, pp. 856–860, 2001.
- [98] J. W. Ndieyira, M. Watari, A. D. Barrera, D. Zhou, M. Vögtli, M. Batchelor, M. A. Cooper, T. Strunz, M. A. Horton, C. Abell, T. Rayment, G. Aeppli, and R. A. Mckendry, “Nanomechanical detection of antibiotic–mucopeptide binding in a model for superbug drug resistance,” *Nat Nanotechnol*, vol. 3, no. 11, pp. 691–696, 2008.
- [99] Z. Lee, C. Ophus, L. M. Fischer, N. Nelson-Fitzpatrick, K. L. Westra, S. Evoy, V. Radmilovic, U. Dahmen, and D. Mitlin, “Metallic NEMS components fabricated from nanocomposite Al–Mo films,” *Nanotechnology*, vol. 17, no. 12, pp. 3063–3070, 2006.
- [100] C. Ophus, N. Nelson-Fitzpatrick, Z. Lee, E. Lubber, C. Harrower, K. Westra, U. Dahmen, V. Radmilovic, S. Evoy, and D. Mitlin, “Resonance properties and microstructure of ultracompliant metallic nanoelectromechanical systems resonators synthesized from Al-32at.%Mo amorphous-nanocrystalline metallic composites,” *Appl Phys Lett*, vol. 92, no. 12, p. 123108, 2008.

- [101] E. Lubber, R. Mohammadi, C. Ophus, Z. Lee, N. Nelson-Fitzpatrick, K. Westra, S. Evoy, U. Dahmen, V. Radmilovic, and D. Mitlin, "Tailoring the microstructure and surface morphology of metal thin films for nano-electro-mechanical systems applications," *Nanotechnology*, vol. 19, no. 12, p. 125705, 2008.
- [102] E. J. Lubber, B. C. Olsen, C. Ophus, V. Radmilovic, and D. Mitlin, "All-metal AFM probes fabricated from microstructurally tailored Cu-Hf thin films," *Nanotechnology*, vol. 20, p. 345703, 2009.
- [103] M. T. A. Saif and N. C. MacDonald, "Measurement of forces and spring constants of microinstruments," *Rev Sci Instrum*, vol. 69, no. 3, pp. 1410–1422, 1998.
- [104] M. T. A. Saif and N. C. MacDonald, "Micro mechanical single crystal silicon fracture studies torsion and bending," *1996 IEEE International Workshop on Micro Electro Mechanical Systems*, pp. 105–109, 1996.
- [105] Y. Zhu, F. Xu, Q. Qin, W. Y. Fung, and W. Lu, "Mechanical properties of vapor liquid solid synthesized silicon nanowires," *Nano Lett*, vol. 9, no. 11, pp. 3934–3939, 2009.
- [106] X. Li, T. Ono, Y. Wang, and M. Esashi, "Ultrathin single-crystalline-silicon cantilever resonators: fabrication technology and significant specimen size effect on young's modulus," *Appl Phys Lett*, vol. 83, no. 15, p. 3081, 2003.
- [107] S. Evoy, "Yield of single crystal Si beam resonators." Personal Communications.
- [108] D. W. Carr, S. Evoy, L. Sekaric, H. G. Craighead, and J. M. Parpia, "Measurement of mechanical resonance and losses in nanometer scale silicon wires," *Appl Phys Lett*, vol. 75, no. 7, pp. 920–922, 1999.
- [109] L. Sekaric, D. W. Carr, S. Evoy, J. M. Parpia, and H. G. Craighead, "Nanomechanical resonant structures in silicon nitride: fabrication, op-

- eration and dissipation issues,” *Sensor Actuat A-Phys*, vol. 101, pp. 215–219, 2002.
- [110] L. M. Fischer, N. Wilding, M. Gel, and S. Evoy, “Low-stress silicon carbonitride for the machining of high-frequency nanomechanical resonators,” *J Vac Sci Technol B*, vol. 25, no. 1, pp. 33–37, 2007.
- [111] M. A. Mohammad, C. Guthy, S. Evoy, S. K. Dew, and M. Stepanova, “Nanomachining and clamping point optimization of silicon carbon nitride resonators using low voltage electron beam lithography and cold development,” *J Vac Sci Technol B*, vol. 28, no. 6, pp. C6P36–C6P41, 2010.
- [112] H. Kim, H.-B.-R. Lee, and W. J. Maeng, “Applications of atomic layer deposition to nanofabrication and emerging nanodevices,” *Thin Solid Films*, vol. 517, no. 8, pp. 2563–2580, 2009.
- [113] K. Westra, *EE 457 Course Notes*. University of Alberta, 2005.
- [114] N. Maluf and K. Williams, *Introduction to microelectromechanical systems engineering*. Boston : Artech House, c2004., 2nd ed., 2004.
- [115] G. T. A. Kovacs, N. I. Maluf, and K. E. Petersen, “Bulk micromachining of silicon,” *P IEEE*, vol. 86, no. 8, pp. 1536–1551, 1998.
- [116] K. E. Petersen, “Silicon as a mechanical material,” *P IEEE*, vol. 70, pp. 420–457, Jan 1982.
- [117] C. R. Yang, P. Y. Chen, C. H. Yang, Y. C. Chiou, and R. T. Lee, “Effects of various ion-typed surfactants on silicon anisotropic etching properties in KOH and TMAH solutions,” *Sensor Actuat A-Phys*, vol. 119, no. 1, pp. 271–281, 2005.
- [118] P. Pal, K. Sato, and S. Chandra, “Fabrication techniques of convex corners in a (100)-silicon wafer using bulk micromachining: a review,” *J Micromech Microeng*, vol. 17, pp. R111–R133, 2007.

- [119] H. Jansen, M. de Boer, R. Legtenberg, and M. Elwenspoek, “The black silicon method: a universal method for determining the parameter setting of a fluorine-based reactive ion etcher in deep silicon trench etching with profile control,” *J Micromech Microeng*, vol. 5, pp. 115–120, 1995.
- [120] M. J. de Boer, J. G. E. Gardeniers, H. V. Jansen, M. J. Gilde, G. Roelofs, J. N. Sasserath, and M. Elwenspoek, “Guidelines for etching silicon mems structures using fluorine high-density plasmas at cryogenic temperatures,” *J Microelectromech S*, vol. 11, no. 4, pp. 385–401, 2002.
- [121] N. Tas, T. Sonnenberg, H. Jansen, R. Legtenberg, and M. Elwenspoek, “Stiction in surface micromachining,” *J Micromech Microeng*, vol. 6, p. 385, 1996.
- [122] P. G. Datskos, T. Thundat, and N. V. Lavrik, “Micro and nanocantilever sensors,” *Encyclopaedia of NanoScience and Nanotechnology*, 2004.
- [123] W. J. Palm, *Mechanical vibration*. Hoboken, NJ : John Wiley, 2007.
- [124] M. DiVentra, S. Evoy, and J. R. Hefflin, eds., *Introduction to nanoscale science and technology*. Boston : Kluwer Academic Publishers, 2004.
- [125] S. S. Verbridge, D. F. Shapiro, H. G. Craighead, and J. M. Parpia, “Macroscopic tuning of nanomechanics: substrate bending for reversible control of frequency and quality factor of nanostring resonators,” *Nano Lett*, vol. 7, no. 6, pp. 1728–1735, 2007.
- [126] S. Evoy, A. Olkhovets, L. Sekaric, J. M. Parpia, H. G. Craighead, and D. W. Carr, “Temperature-dependent internal friction in silicon nanoelectromechanical systems,” *Appl Phys Lett*, vol. 77, no. 15, pp. 2397–2399, 2000.
- [127] T. H. Metcalf, X. Liu, B. H. Houston, J. W. Baldwin, J. E. Butler, and T. Feygelson, “Low temperature internal friction in nanocrystalline diamond films,” *Appl Phys Lett*, vol. 86, no. 8, p. 081910, 2005.

- [128] Y. Wang, J. A. Henry, A. T. Zehnder, and M. A. Hines, “Surface chemical control of mechanical energy losses in micromachined silicon structures,” *J Phys Chem B*, vol. 107, no. 51, pp. 14270–14277, 2003.
- [129] Y. Wang, J. A. Henry, D. Sengupta, and M. A. Hines, “Methyl monolayers suppress mechanical energy dissipation in micromechanical silicon resonators,” *Appl Phys Lett*, vol. 85, no. 23, p. 5736, 2004.
- [130] P. S. Waggoner and H. G. Craighead, “Micro- and nanomechanical sensors for environmental, chemical, and biological detection,” *Lab Chip*, vol. 7, no. 10, p. 1238, 2007.
- [131] N. Liu, F. Giesen, M. Belov, J. Losby, J. Moroz, A. E. Fraser, G. McKinnon, T. J. Clement, V. Sauer, W. K. Hiebert, and M. R. Freeman, “Time-domain control of ultrahigh-frequency nanomechanical systems,” *Nat Nanotechnol*, vol. 3, no. 12, pp. 715–719, 2008.
- [132] S. S. Verbridge, H. G. Craighead, and J. M. Parpia, “A megahertz nanomechanical resonator with room temperature quality factor over a million,” *Appl Phys Lett*, vol. 92, p. 013112, 2008.
- [133] Z. J. Davis and A. Boisen, “Aluminum nano-cantilevers for high sensitivity mass sensors,” *Appl Phys Lett*, vol. 87, p. 013102, 2005.
- [134] K. Ekinici, Y. Yang, and M. Roukes, “Ultimate limits to inertial mass sensing based upon nanoelectromechanical systems,” *Journal of Applied Physics*, vol. 95, p. 2682, 2004.
- [135] N. J. Quitoriano, M. Belov, S. Evoy, and T. I. Kamins, “Single-crystal, si nanotubes, and their mechanical resonant properties,” Jan 2009.
- [136] C. Guthy, R. M. Das, B. Drobot, and S. Evoy, “Resonant characteristics of ultranarrow SiCN nanomechanical resonators,” *J Appl Phys*, vol. 108, no. 1, p. 014306, 2010.

- [137] Y. Yang, C. Callegari, X. Feng, K. Ekinici, and M. Roukes, “Zeptogram-scale nanomechanical mass sensing,” *Nano Lett*, vol. 6, no. 4, pp. 583–586, 2006.
- [138] R. R. Grüter, Z. Khan, R. Paxman, J. W. Ndieyira, B. Dueck, B. A. Bircher, J. L. Yang, U. Drechsler, M. Despont, R. A. Mckendry, and B. W. Hoogenboom, “Disentangling mechanical and mass effects on nanomechanical resonators,” *Appl Phys Lett*, vol. 96, no. 2, p. 023113, 2010.
- [139] A. W. McFarland, M. A. Poggi, M. J. Doyle, L. A. Bottomley, and J. S. Colton, “Influence of surface stress on the resonance behavior of microcantilevers,” *Appl Phys Lett*, vol. 87, no. 5, p. 053505, 2005.
- [140] J. R. Barnes, R. J. Stephenson, M. E. Welland, C. Gerber, and J. K. Gimzewski, “Photothermal spectroscopy with femtojoule sensitivity using a micromechanical device,” *Nature*, vol. 372, pp. 79–81, 1994.
- [141] H. Ibach, “Adsorbate-induced surface stress,” *J Vac Sci Technol A*, vol. 12, no. 4, pp. 2240–2245, 1994.
- [142] R. Shuttleworth, “The surface tension of solids,” *P Phys Soc Lond A*, vol. 63, p. 444, 1950.
- [143] J. J. Headrick, M. J. Sepaniak, N. V. Lavrik, and P. G. Datskos, “Enhancing chemi-mechanical transduction in microcantilever chemical sensing by surface modification,” *Ultramicroscopy*, 2003.
- [144] G. G. Stoney, “The tension of metallic films deposited by electrolysis,” *P Roy Soc Lond A Mat*, 1909.
- [145] S. A. Campbell, *The science and engineering of microelectronic fabrication*. New York : Oxford University Press, 2nd ed., 2001.
- [146] C. A. Klein, “How accurate are stoney’s equation and recent modifications,” *J Appl Phys*, vol. 88, p. 5487, 2000.

- [147] J. E. Sader, "Surface stress induced deflections of cantilever plates with applications to the atomic force microscope: Rectangular plates," *J Appl Phys*, vol. 89, p. 2911, 2001.
- [148] M. Godin, *Surface Stress, Kinetics, and Structure of Alkanethiol Self-Assembled Monolayers*. PhD thesis, McGill, Aug 2005.
- [149] R. Raiteri, M. Grattarola, H. J. Butt, and P. Skládal, "Micromechanical cantilever-based biosensors," *Sensor Actuat B-Chem*, vol. 79, no. 2-3, pp. 115–126, 2001.
- [150] C. Wang, D. Wang, Y. Mao, and X. Hu, "Ultrasensitive biochemical sensors based on microcantilevers of atomic force microscope.," *Anal Biochem*, vol. 363, no. 1, p. 1, 2007.
- [151] G. Meyer and N. M. Amer, "Novel optical approach to atomic force microscopy," *Appl Phys Lett*, vol. 53, no. 12, pp. 1045–1047, 1988.
- [152] G. Meyer and N. M. Amer, "Optical-beam-deflection atomic force microscopy: The NaCl (001) surface," *Appl Phys Lett*, vol. 56, no. 21, pp. 2100–2101, 1990.
- [153] L. G. Carrascosa, M. Moreno, M. Alvarez, and L. M. Lechuga, "Nanomechanical biosensors: a new sensing tool," *TrAC-Trend Anal Chem*, vol. 25, no. 3, pp. 196–206, 2006.
- [154] U. C. Hubler, F. M. Battiston, and B. A. Hermann, "Cantilever apparatus and method for detecting microorganisms," *EP Patent 1,342,789*, Jan 2005.
- [155] D. W. Carr and H. G. Craighead, "Fabrication of nanoelectromechanical systems in single crystal silicon using silicon on insulator substrates and electron beam lithography," *J Vac Sci Technol B*, vol. 15, no. 6, pp. 2760–2763, 1997.
- [156] H. G. Craighead, "Nanoelectromechanical systems," *Science*, 2000.

- [157] P. Hariharan, *Basics of interferometry*. Amsterdam ; Boston : Elsevier Academic Press, 2nd ed., 2007.
- [158] C. O'Mahony, M. Hill, M. Brunet, R. Duane, and A. Mathewson, "Characterization of micromechanical structures using white-light interferometry," *Meas Sci Technol*, vol. 14, no. 10, pp. 1807–1814, 2003.
- [159] W. Fang and J. A. Wickert, "Determining mean and gradient residual stresses in thin-films using micromachined cantilevers," *J Micromech Microeng*, vol. 6, no. 3, pp. 301–309, 1996.
- [160] E. M. Lawrence, K. E. Speller, and D. Yu, "Mems characterization using laser doppler vibrometry," *Proc SPIE*, vol. 4980, p. 51, 2003.
- [161] C. Rembe, R. Kant, and R. S. Muller, "Optical measurement methods to study dynamic behavior in mems," *Proc SPIE*, vol. 4400, pp. 127–137, 2001.
- [162] C. Rembe and T. Haist, "Interferometer for optically measuring an object," *US Patent App. 2010/201,990*, Jan 2010.
- [163] C. Rembe, G. Siegmund, and T.-H. Xu, "Vibrometer and method for optically measuring an object," *US Patent App. 2009/251706*, Jan 2009.
- [164] X. Liu, J. F. Vignola, H. J. Simpson, B. R. Lemon, B. H. Houston, and D. M. Photiadis, "A loss mechanism study of a very high q silicon micromechanical oscillator," *J Appl Phys*, vol. 97, no. 2, p. 023524, 2005.
- [165] J. F. Vignola, X. Liu, S. F. Morse, B. H. Houston, J. A. Bucaro, M. H. Marcus, D. M. Photiadis, and L. Sekaric, "Characterization of silicon micro-oscillators by scanning laser vibrometry," *Rev Sci Instrum*, vol. 73, no. 10, pp. 3584–3588, 2002.
- [166] E. M. Lawrence and C. Rembe, "Mems characterization using new hybrid laser doppler vibrometer/strobe video system," *Proc SPIE*, vol. 5343, p. 45, 2004.

- [167] T. W. Kenny, W. J. Kaiser, J. A. Podosek, H. K. Rockstad, J. K. Reynolds, and E. C. Vote, "Micromachined tunneling displacement transducers for physical sensors," *J Vac Sci Technol A*, vol. 11, no. 4, pp. 797–802, 1993.
- [168] D. V. Scheible, A. Erbe, and R. H. Blick, "Dynamic control and modal analysis of coupled nano-mechanical resonators," *Appl Phys Lett*, 2003.
- [169] D. V. Scheible, C. Weiss, and R. H. Blick, "Effects of low attenuation in a nanomechanical electron shuttle," *J Appl Phys*, 2004.
- [170] J. Thaysen, "Piezoresistive microcantilever sensor," *WO Patent WO/2005/100,235*, Jan 2005.
- [171] M. Li, H. X. Tang, and M. L. Roukes, "Ultra-sensitive nems-based cantilevers for sensing, scanned probe and very high-frequency applications," *Nat Nanotechnol*, vol. 2, no. 2, pp. 114–120, 2007.
- [172] A. Johansson, O. Hansen, J. Hales, and A. Boisen, "Temperature effects in Au piezoresistors integrated in SU-8 cantilever chips," *J Micromech Microeng*, vol. 16, p. 2564, 2006.
- [173] A. Johansson, G. Blagoi, and A. Boisen, "Polymeric cantilever-based biosensors with integrated readout," *Appl Phys Lett*, vol. 89, no. 17, p. 173505, 2006.
- [174] N. Blanc, J. Brugger, N. F. de Rooij, and U. Durig, "Scanning force microscopy in the dynamic mode using microfabricated capacitive sensors," *J Vac Sci Technol B*, vol. 14, no. 2, pp. 901–905, 1996.
- [175] N. Nelson-Fitzpatrick, K. Westra, P. Li, S. McColman, N. Wilding, and S. Evoy, "Fabrication of nanoelectromechanical resonators using a cryogenic etching technique," *J Vac Sci Technol B*, vol. 24, p. 2769, 2006.
- [176] K. L. Ekinici and M. L. Roukes, "Nanoelectromechanical systems," *Rev Sci Instrum*, vol. 76, no. 6, p. 061101, 2005.

- [177] G. K. Celler and S. Cristoloveanu, "Frontiers of silicon-on-insulator," *J Appl Phys*, vol. 93, p. 4955, 2003.
- [178] M. Bruel, "Application of hydrogen ion beams to silicon on insulator material technology," *Nucl Instrum Meth B*, vol. 108, no. 3, pp. 313–319, 1996.
- [179] K. Izumi, M. Doken, and H. Ariyoshi, "CMOS devices fabricated on buried SiO₂ layers formed by oxygen implantation into silicon," *Electron Lett*, vol. 14, no. 18, pp. 593–594, 1978.
- [180] G. L. Weibel and C. K. Ober, "An overview of supercritical CO₂ applications in microelectronics processing," *Microelectron Eng*, vol. 65, no. 1-2, pp. 145–152, 2003.
- [181] B. Houli, V. Umansky, and M. Heiblum, "Low-energy electron beam lithography with 30 nm resolution," *Semicond Sci Tech*, vol. 8, p. 1490, 1993.
- [182] S. C. Buswell, "Planar photonic crystals for biosensing and nonlinear polymer integration," Master's thesis, University of Alberta, 2008.
- [183] D. Drouin, A. R. Couture, D. Joly, X. Tastet, V. Aimez, and R. Gauvin, "Casino v2. 42-a fast and easytouse modeling tool for scanning electron microscopy and microanalysis users," *Scanning*, vol. 29, no. 3, pp. 92–101, 2007.
- [184] R. Dussart, M. Boufnichel, G. Marcos, P. Lefauchaux, A. Basillais, R. Benoit, T. Tillocher, X. Mellhaoui, H. Estrade-Szwarczkopf, and P. Ranson, "Passivation mechanisms in cryogenic SF₆ / O₂ etching process," *J Micromech Microeng*, vol. 14, no. 2, pp. 190–196, 2003.
- [185] T. J. Clement, R. G. DeCorby, N. Ponnampalam, T. W. Allen, A. Hryciw, and A. Meldrum, "Nanocluster sensitized erbium-doped silicon monoxide waveguides," *Opt Express*, vol. 14, no. 25, pp. 12151–12162, 2006.

- [186] N. Nelson-Fitzpatrick, C. Ophus, E. Lubber, L. Gervais, Z. Lee, V. Radmilovic, D. Mitlin, and S. Evoy, "Synthesis and characterization of au-ta nanocomposites for nanomechanical cantilever devices," *Nanotechnology*, vol. 18, no. 35, p. 355303, 2007.
- [187] A. Chand, M. B. Viani, T. E. Schaffer, and P. K. Hansma, "Micro-fabricated small metal cantilevers with silicon tip for atomicforce microscopy," *J Microelectromech S*, 2000.
- [188] C. Ophus, *Nanoscale Resonators Fabricated from Metallic Alloys, and Modeling and Simulation of Polycrystalline Thin Film Growth*. PhD thesis, University of Alberta, 2010.
- [189] H. Okamoto and T. B. Massalski, "The Au-Ta (gold-tantalum) system," *J Phase Equilib*, vol. 6, no. 4, pp. 365–368, 1985.
- [190] F. Pan, Y. G. Chen, Z. J. Zhang, and B. X. Liu, "Size effect on glass-forming ability in the Au-Ta system upon ion mixing," *J Non-Cryst Solids*, vol. 194, no. 3, pp. 305–311, 1996.
- [191] K. Robbie, L. J. Friedrich, S. K. Dew, T. Smy, and M. J. Brett, "Fabrication of thin films with highly porous microstructures," *J Vac Sci Technol A*, vol. 13, no. 3, pp. 1032–1035, 1995.
- [192] A. Greer, *Thermodynamics of nanostructured materials*. Kluwer: Dordrecht and Boston, 1993.
- [193] B. X. Liu, "Prediction of metallic glass formation by ion mixing," *Mater Lett*, vol. 5, no. 9, pp. 322–327, 1987.
- [194] B. S. Murty, D. H. Ping, and K. Hono, "Nanoquasicrystallization of binary Zr-Pd metallic glasses," *Appl Phys Lett*, vol. 77, no. 8, p. 1102, 2000.
- [195] B. D. Cullity and S. R. Stock, *Elements of X-ray Diffraction*. Prentice-Hall, 2003.

- [196] J. Musil and J. Vlcek, "Magnetron sputtering of alloy and alloy-based films," *Thin solid films*, vol. 343, pp. 47–50, 1999.
- [197] A. B. Bhatia and D. E. Thornton, "Structural aspects of the electrical resistivity of binary alloys," *Phys Rev B*, vol. 2, no. 8, pp. 3004–3012, 1970.
- [198] W. C. Oliver and G. M. Pharr, "Measurement of hardness and elastic modulus by instrumented indentation: Advances in understanding and refinements to methodology," *J Mater Res*, vol. 19, no. 1, pp. 1–18, 2004.
- [199] C. C. Lo, J. A. Augis, and M. R. Pinnel, "Hardening mechanisms of hard gold," *J Appl Phys*, vol. 50, no. 11, 1979.
- [200] M. Zhang, B. Yang, J. Chu, and T. G. Nieh, "Hardness enhancement in nanocrystalline tantalum thin films," *Scripta Mater*, vol. 54, no. 7, pp. 1227–1230, 2006.
- [201] D. S. Lin and H. Wilman, "Friction, wear and surface hardness in abrasion of binary solid-solution alloys in the copper-gold system," *J Phys D Appl Phys*, vol. 1, no. 2, pp. 561–571, 1968.
- [202] Y. Arntz, J. D. Seelig, H. P. Lang, J. Zhang, P. Hunziker, J. P. Ramseyer, E. Meyer, M. Hegner, and C. Gerber, "Label-free protein assay based on a nanomechanical cantilever array," *Nanotechnology*, vol. 14, pp. 86–90, 2003.
- [203] M. Calleja, J. Tamayo, A. Johansson, P. Rasmussen, L. Lechuga, and A. Boisen, "Polymeric cantilever arrays for biosensing applications," *Sens Lett*, vol. 1, no. 1, pp. 20–24, 2003.
- [204] J. Pei, F. Tian, and T. Thundat, "Novel glucose biosensor based on the microcantilever," *Anal Chem*, vol. 76, no. 2, pp. 292–297, 2004.
- [205] M. Calleja, J. Tamayo, M. Nordstrom, and A. Boisen, "Low-noise polymeric nanomechanical biosensors," *Appl Phys Lett*, vol. 88, no. 11, p. 113901, 2006.

- [206] V. Seena, A. Rajorya, P. Pant, S. Mukherji, and V. Rao, "Polymer microcantilever biochemical sensors with integrated polymer composites for electrical detection," *Solid State Sci*, vol. 11, no. 9, pp. 1606–1611, 2009.
- [207] L. Gammelgaard, P. A. Rasmussen, M. Calleja, P. Vettiger, and A. Boisen, "Microfabricated photoplastic cantilever with integrated photoplastic/carbon based piezoresistive strain sensor," *Appl Phys Lett*, vol. 88, p. 113508, 2006.
- [208] N. S. Kale, S. Nag, R. Pinto, and V. R. Rao, "Fabrication and characterization of a polymeric microcantilever with an encapsulated hotwire cvd polysilicon piezoresistor," *J Microelectromech S*, vol. 18, no. 1, pp. 79–87, 2009.
- [209] S. Keller, D. Haefliger, and A. Boisen, "Fabrication of thin SU-8 cantilevers: initial bending, release and time stability," *J Micromech Microeng*, vol. 20, p. 045024, 2010.
- [210] R. G. Nuzzo, B. R. Zegarski, and L. H. Dubois, "Fundamental-studies of the chemisorption of organosulfur compounds on Au(111) - implications for molecular self-assembly on gold surfaces," *J Am Chem Soc*, vol. 109, no. 3, pp. 733–740, 1987.
- [211] L. H. Dubois and R. G. Nuzzo, "Synthesis, structure, and properties of model organic surfaces," *Annu Rev Phys Chem*, vol. 43, no. 1, pp. 437–463, 1992.
- [212] G. M. Whitesides and P. E. Laibinis, "Wet chemical approaches to the characterization of organic-surfaces - self-assembled monolayers, wetting, and the physical organic-chemistry of the solid liquid interface," *Langmuir*, vol. 6, no. 1, pp. 87–96, 1990.
- [213] D. K. Schwartz, "Mechanisms and kinetics of self-assembled monolayer formation," *Annu Rev Phys Chem*, vol. 52, no. 1, p. 107, 2001.

- [214] J. C. Love, L. A. Estroff, J. K. Kriebel, R. G. Nuzzo, and G. M. Whitesides, "Self-assembled monolayers of thiolates on metals as a form of nanotechnology," *Chem Rev*, vol. 105, no. 4, pp. 1103–1170, 2005.
- [215] G. Poirier, "Characterization of organosulfur molecular monolayers on Au (111) using scanning tunneling microscopy," *Chem Rev*, vol. 97, no. 4, pp. 1117–1128, 1997.
- [216] G. E. Poirier and E. D. Pylant, "The self-assembly mechanism of alkanethiols on Au (111)," *Science*, vol. 272, no. 5265, pp. 1145–1148, 1996.
- [217] P. G. DeGennes, "Wetting: statics and dynamics," *Rev Mod Phys*, vol. 57, no. 3, pp. 827–863, 1985.
- [218] A. Ulman, *An introduction to ultrathin organic films*. Academic Press, 1991.
- [219] H. Ron, S. Matlis, and I. Rubinstein, "Self-assembled monolayers on oxidized metals. 2. gold surface oxidative pretreatment, monolayer properties, and depression formation," *Langmuir*, vol. 14, no. 5, pp. 1116–1121, 1998.
- [220] C. D. Bain and G. M. Whitesides, "Modeling organic surfaces with self-assembled monolayers," *Angew Chem Int Edit*, vol. 28, no. 4, pp. 506–512, 1989.
- [221] J. Chastain and R. King, eds., *Handbook of x-ray photoelectron spectroscopy : a reference book of standard spectra for identification and interpretation of XPS data*. Eden Prairie, Minn. : Physical Electronics, 1995.
- [222] M. Buck, F. Eisert, J. Fischer, M. Grunze, and F. Trager, "Investigation of self-organizing thiol films by optical 2nd-harmonic generation and x-ray photoelectron-spectroscopy," *Appl Phys A-Mater*, vol. 53, no. 6, pp. 552–556, 1991.

- [223] T. Ishida, S. Tsuneda, N. Nishida, M. Hara, H. Sasabe, and W. Knoll, "Surface-conditioning effect of gold substrates on octadecanethiol self-assembled monolayer growth," *Langmuir*, vol. 13, no. 17, pp. 4638–4643, 1997.
- [224] J. Coates, "Interpretation of infrared spectra, a practical approach," *Enc Anal Bhem*, pp. 10815–10837, 2000.
- [225] L. M. Fischer, M. Tenje, A. R. Heiskanen, N. Masuda, J. Castillo, A. Bientien, J. Émneus, M. H. Jakobsen, and A. Boisen, "Gold cleaning methods for electrochemical detection applications," *Microelectron Eng*, vol. 86, pp. 1282–1285, 2009.
- [226] "Concentris CLA500-010-08, <http://www.concentris.com/>," 2011 Jan.
- [227] M. Godin, V. Tabard-Cossa, P. Grütter, and P. Williams, "Quantitative surface stress measurements using a microcantilever," *Appl Phys Lett*, vol. 79, no. 4, pp. 551–553, 2001.
- [228] T. Suntola, "Cost-effective processing by atomic layer epitaxy," *Thin Solid Films*, vol. 225, no. 1-2, pp. 96–98, 1993.
- [229] Y. J. Chang, J. M. Gray, A. Imtiaz, D. Seghete, T. M. Wallis, S. M. George, P. Kabos, C. T. Rogers, and V. M. Bright, "Micromachined resonators of high Q-factor based on atomic layer deposited alumina," *Sensor Actuat A-Phys*, vol. 154, no. 2, pp. 229–237, 2009.
- [230] M. K. Tripp, C. Stampfer, C. F. Herrmann, C. Hierold, S. George, and V. M. Bright, "Low stress atomic layer deposited alumina for nano electro mechanical systems," *The 13th International Conference on Solid-State Sensors, Actuators and Microsystems*, vol. 1, pp. 851–854, 2005.
- [231] D. Seghete, B. D. Davidson, R. A. Hall, Y. J. Chang, V. M. Bright, and S. M. George, "Sacrificial layers for air gaps in NEMS using alucone molecular layer deposition," *Sensor Actuat A-Phys*, vol. 155, no. 1, pp. 8–15, 2009.

- [232] P. S. Waggoner, C. P. Tan, and H. G. Craighead, "Atomic layer deposited silicon dioxide films on nanomechanical silicon nitride resonators," *Journal of Applied Physics*, vol. 107, p. 114505, Jan 2010.
- [233] S. B. S. Heil, E. Langereis, F. Roozeboom, M. C. M. van de Sanden, and W. M. M. Kessels, "Low-temperature deposition of TiN by plasma-assisted atomic layer deposition," *J Electrochem Soc*, vol. 153, no. 11, p. G956, 2006.
- [234] K. R. Williams, K. Gupta, and M. Wasilik, "Etch rates for micromachining processing-part II," *J Microelectromech S*, vol. 12, no. 6, pp. 761–778, 2003.
- [235] E. Langereis, S. B. S. Heil, M. C. M. V. D. Sanden, and W. M. M. Kessels, "In situ spectroscopic ellipsometry study on the growth of ultrathin TiN films by plasma-assisted atomic layer deposition," *J Appl Phys*, vol. 100, p. 023534, 2006.
- [236] E. Langereis, S. B. S. Heil, H. C. M. Knoop, W. Keuning, M. C. M. van de Sanden, and W. M. M. Kessels, "In situ spectroscopic ellipsometry as a versatile tool for studying atomic layer deposition," *J Phys D Appl Phys*, vol. 42, no. 7, pp. 73001–73019, 2009.
- [237] S. Li, C. Q. Sun, and H. S. Park, "Grain boundary structures of atomic layer deposited TiN," *Thin Solid Films*, vol. 504, no. 1-2, pp. 108–112, 2006.
- [238] C. Mousty-Desbuquoit, J. Riga, and J. J. Verbist, "Electronic structure of titanium (III) and titanium (IV) halides studied by solid-phase x-ray photoelectron spectroscopy," *Inorg Chem*, vol. 26, pp. 1212–1217, 1987.
- [239] "NIST XPS database, <http://srdata.nist.gov/xps/default.aspx>," March 2011.

- [240] M. C. Lemme, J. K. Efavi, T. Mollenhauer, M. Schmidt, H. D. B. Gottlob, T. Wahlbrink, and H. Kurz, “Nanoscale TiN metal gate technology for CMOS integration,” *Microelectron Eng*, vol. 83, pp. 1551–1554, 2006.
- [241] L. Fischer, “Development of silicon carbonitride nanomechanical resonators for biological detection applications,” Master’s thesis, University of Alberta, 2007.
- [242] J. R. Taylor, *An Introduction to Error Analysis*. University Science Books, 2nd ed., 1997.

APPENDIX A

Au-Ta Static Cantilever Wafermap

A.1 Wafermap for Static Au-Ta cantilevers

A 5" contact photolithography mask was designed for the patterning of the static Au-Ta cantilevers described in chapter 5. Figure A.1 is an image of the liftoff mask as designed using Tanner L-Edit 12.1. This mask image is inverted (orange polygons are clear on the actual mask) due to our use of liftoff technique for patterning. Additional masks were fabricated to protect cantilever clamping points and beams from attack during the SF₆ etch release; unfortunately these masking steps proved insufficient and were omitted in later fabrication runs.

Figure A.2 is an image of the cantilever unit cell with the dimensions of the cantilevers.

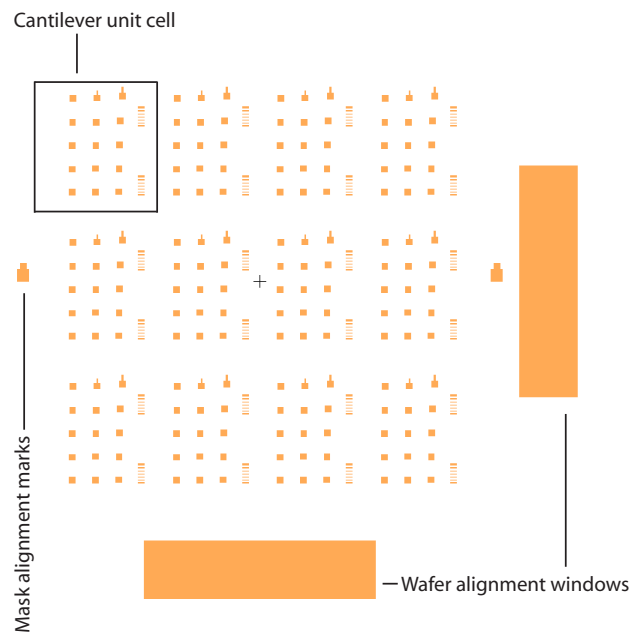


Figure A.1: Mask pattern for the AuTa static cantilevers.

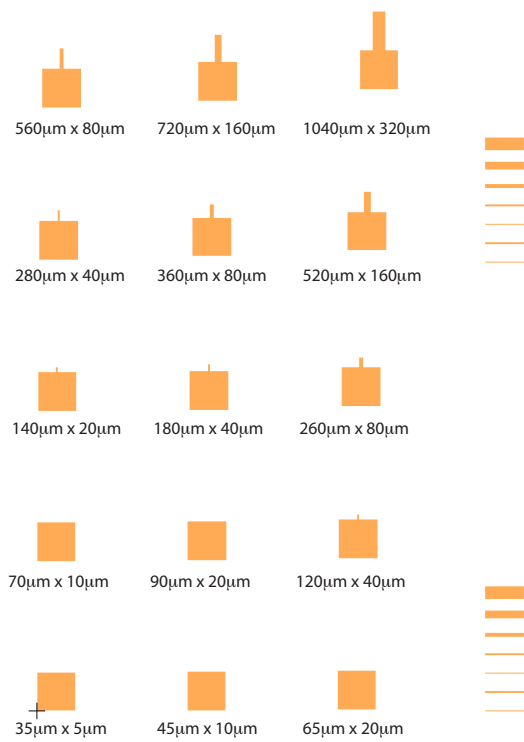


Figure A.2: One cell of AuTa static cantilever mask, with cantilever dimensions.

APPENDIX B

Reactive sputtered TiN

B.1 Reactive Sputter Background

The ALD system relies on a mechanically delicate dry pump system that can be unreliable. Due to the possibility of downtime we explored alternative methods of depositing TiN. One such method is to sputter Ti in a nitrogen rich environment, this process is termed reactive sputtering. When employing reactive sputtering one must be aware of the stoichiometric state of the material. Typically in DC reactive sputtering of insulating compounds as gaseous reactant flow is increased beyond a critical level the formation of an insulating layer on the target is promoted and the sputter rate drops precipitously. However in the case of TiN we are depositing a relatively conductive material and we should not expect dramatic target “poisoning” effects as one would expect with reactive deposition of an insulating material.

Table B.1: Reactively sputtered TiN recipe summary

Recipe name	Ar flow sccm	N ₂ flow sccm	Pressure mTorr	Power W	t _{rev} μs	Frequency kHz	dep. rate $\frac{nm}{s}$
SpTiN 1	14.6	14.5	6.7	250	0.5	150	3.16
SpTiN 2	14.6	16.0	6.7	250	0.5	150	3.29

Table B.2: Reactively sputtered TiN composition as determined by X-ray photoelectron spectroscopy.

Recipe Name	Deposition temp. °C	O %at.	Ti %at.	N %at.	C %at.	Ti / N ratio unitless
SpTiN 1	150	36.8	31.6	22.5	9.1	1.41
SpTiN 2	150	36.9	32.6	23.6	6.9	1.38
SpTiN 1	20	37.0	32.8	22.2	8.0	1.48
SpTiN 2	20	35.8	30.0	21.7	12.4	1.38

We developed two separate recipes for the deposition of TiN (outlined in table B.1). The N₂ flow rate was chosen by conducting a test deposition and monitoring for a drop in target voltage as N₂ flow was increased, this was a small effect. The recipes employed are summarized in a table below.

To ensure close to stoichiometric films we wish to deposit the material at a gas flow rate that is just below this critical level. To this end a target voltage test was performed on our DC reactive sputter system to determine the point at which we are forming TiN on the target. Target voltage was observed to increase erratically with added N₂ flow from since TiN is a relatively conductive material

B.2 XPS

X-ray photoelectron spectroscopy was conducted for the reactively sputtered films as outlined in chapter 6 for the ALD TiN films. Films surfaces were sputtered away with a 2 min Ar sputter step, then high resolution XPS count were taken for O, Ti, N, C, and Cl. Cl was not present in any samples since there is no source for it in the reactive sputter process. Table B.2 contains composition data for the reactively sputtered TiN films.

From Table B.2 we can see that all films are highly Ti rich, as we had observed before in the ALD TiN films. Additionally, there is significant O content, which

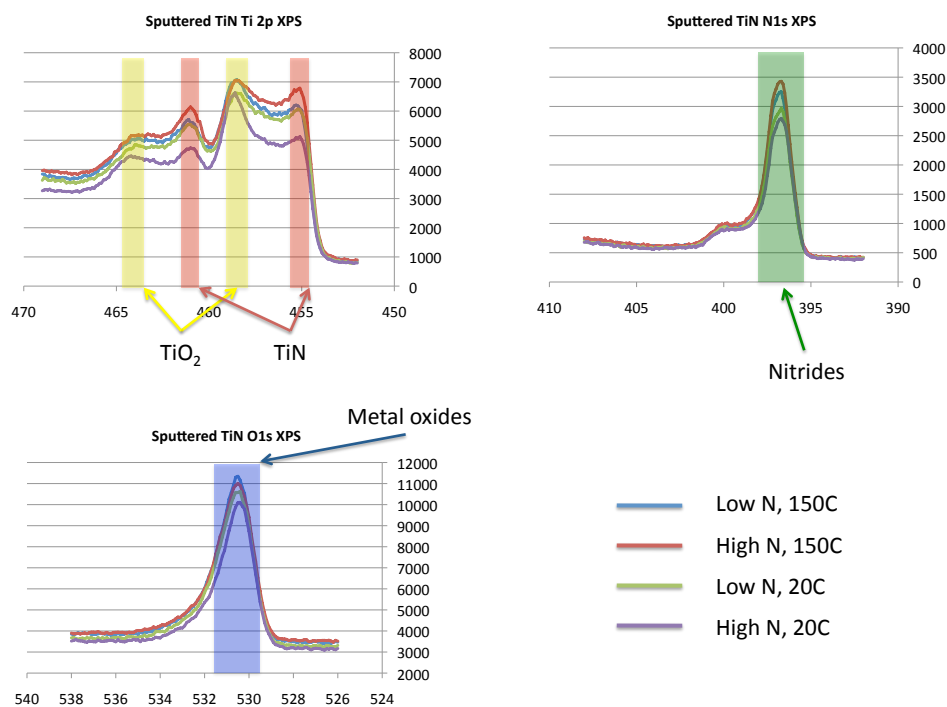


Figure B.1: High resolution XPS scans of Ti, N and O for reactively sputtered TiN films.

is likely due to the presence of TiO_2 in the films. A shoulder peak (of $\text{Ti } 2p_{3/2}$) was observed at 458 eV in the reactively sputtered films as we had observed in the ALD TiN films. This 458 eV peak can be conclusively tied to the presence of TiO_2 in the reactively sputtered films, as there is no other plausible contaminant species in that energy range. The source of TiO_2 in these films is the presence of oxygen from water vapour and trace gases left from pumping down to the 10^{-6} Torr range combined with Ti's great affinity for oxygen. The Ti / N ratio observed in the reactively sputtered films is comparable to ratios observed in low temperature ALD TiN films. Carbon contamination is also comparable to the amounts observed in the ALD synthesized films.

Table B.3: Deposited stress of reactively sputtered TiN films.

Sample Name	Recipe Name	Deposition temp. °C	Avg. Stress MPa	St. Dev. Stress MPa
Sp7	SpTiN 1	150	49.5	133.6
Sp8	SpTiN 2	150	38.5	100.5
Sp9	SpTiN 1	20	17.5	180.5
Sp10	SpTiN 2	20	33.7	102.2

B.3 Stress

Stress measurements for the reactively sputtered TiN were taken with the Flexus 2320 thin films stress measurement system. Table B.3 is a summary of these measurements.

From Table C.3 we can see that all the reactively sputtered TiN films are mildly tensile. There appears to be little to no difference in the deposited stress between high and low deposition temperatures. It is likely that the effect of thermal mismatch stress is being counteracted by some modification of the intrinsic stress. The low tensile stress state in all cases means that any of these film recipes and temperatures would be suitable for cantilever resonator fabrication.

B.4 Fabrication

The fabrication of TiN nanobeam resonators from sputtered TiN was conducted using a bulk machining methodology similar to one described by Fischer *et al.* (241; 33). 50 nm of Reactively sputtered TiN was first deposited onto a piranha cleaned Si wafer using the SpTiN 2 recipe (at 150°C, as outlined in table B.3). Dies were cleaved into approximately 1 cm x 1 cm dies and cleaned with isopropyl alcohol to gently remove organics (piranha solution will etch TiN quickly). The samples were then dehydrated on a hot plate at 250°C

for 5 min in the ambient atmosphere of a class 10 environment. A 60 nm thick hydrogen silsesquioxane (HSQ) electron beam resist was spun and then baked at 150°C for 5 min. The substrates were patterned with a Raith150-TWO Electron Beam Lithography (EBL) system (30 kV, 10 μ m aperture, anchors defined as areas with dose 650 $\frac{\mu\text{C}}{\text{cm}^2}$, beams defined by single pixel line with dose 4000 $\frac{\mu\text{C}}{\text{cm}}$) and developed in a 30% TMAH solution. HSQ is a negative tone resist, upon development in TMAH the HSQ crosslinks and hardens into an SiO₂-like film. The patterned HSQ is used as a mask for the subsequent RIE step.

The patterned TiN dies were then mounted on a Si wafer with vacuum grease, taken to an Oxford Plasmalab DRIE tool and subjected to a Cl₂ etch for 23 s at 20°C. Lemme *et al.* (240) demonstrated the etching of TiN in a similar reactor with a combination of Cl₂ and HBr gas chemistries. Previous etch testing determined the etch rate of the Cl₂ recipe to be 2.3 $\frac{\text{nm}}{\text{s}}$ + 4.9 nm for the strike step. After etching, the SiO₂ masking layer is removed by a 5 min bath in BOE. A KOH solution (961 ml 45% KOH, 567 ml deionized water, 250 ml isopropyl alcohol) is now prepared for the etch release step. A KOH solution is employed because it etches silicon anisotropically, enabling rapid etching of the <110> and <100> planes over the <111> plane of the wafer. This attribute can be leveraged to allow for very deep etching below most of the cantilever beam while the clamping point undergoes relatively little underetching. The capillary force associated with stiction is inversely proportional to the gap between the released structure and the substrate, thus the KOH release can be used to avoid stiction without having to resort to critical point drying. The patterned dies are etched in the KOH solution for 2 min at 75°, then rinsed successively in isopropyl alcohol and pentane. A representative SEM image of a released sputtered TiN beam is provided in figure B.2.

All nanoresonator beams fabricated by this method were observed suffer from fracturing within 1 μ m of the clamping point. Furthermore, all the broken beams were curled upwards indicating that there was a significant stress gra-

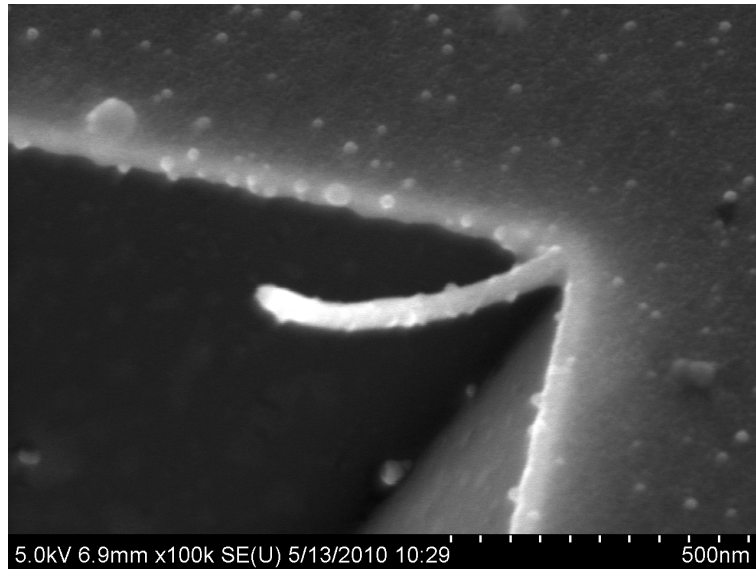


Figure B.2: Scanning electron micrograph of a beam structure fabricated from reactively sputtered TiN. All beams fabricated in this manner experienced similar fracturing.

dient in the reactively sputtered TiN. The use of reactively sputtered TiN for nanobeam resonators was not pursued after this point, due to the extremely low yield.

APPENDIX C

Au-Ta AFM, nanoindentation and stress data

C.1 AFM, Nanoindentation and Stress measurement Data for Au-Ta films

Table C.1: Data from nanoindentation testing - Nanohardness

Ta content % at.	Average GPa	Standard deviation GPa	Standard error GPa
0	2.36	0.0851	0.01702
2	3.72	0.1079	0.02158
10	6.11	0.1495	0.02990
18	7.65	0.2985	0.05970
26	8.65	0.4438	0.08876
34	9.49	0.3640	0.0728
42	8.94	0.5510	0.1102
50	8.67	0.3316	0.06632
65	11.63	0.3792	0.07584
100	18.48	0.6678	0.1336

Table C.2: Data from nanoindentation testing - Reduced modulus

Ta content % at.	Average GPa	Standard deviation GPa	Standard error GPa
0	135.21	15.78	3.156
2	145.22	10.85	2.170
10	140.62	10.77	2.154
18	158.90	9.66	1.932
26	163.04	10.32	2.064
34	162.74	13.02	2.604
42	164.57	6.78	1.356
50	143.72	3.82	0.764
65	161.56	5.19	1.038
100	175.69	7.02	1.404

Table C.3: Data from nanoindentation testing - Contact depth

Ta content % at.	Average GPa	Standard deviation GPa	Standard error GPa
0	80.02	1.690	0.3380
2	60.74	1.070	0.2140
10	45.12	0.6527	0.1305
18	39.57	0.8730	0.1746
26	36.88	1.090	0.2180
34	34.94	0.7569	0.1514
42	36.20	1.290	0.2580
50	36.79	0.8140	0.1628
65	31.11	0.5719	0.1144
100	24.01	0.4924	0.09848

Table C.4: Data from atomic force microscopy testing - roughness

Ta content % at.	RMS roughness nm
0	4.38
2	2.44
10	2.09
18	1.99
42	1.80
50	1.31
65	0.546

Table C.5: Data from film stress testing

Ta content % at.	Average MPa	Min MPa	Max MPa	Standard deviation MPa
0	-30.73	-104.00	7.11	15.01
3.2	-30.19	-77.80	35.42	16.80
5	20.35	-48.50	186.43	31.08
10	46.84	-17.10	112.07	21.43
18	60.77	3.23	117.23	20.02
26	-36.05	-103.00	18.33	17.63
50	-450.03	-546.00	-371.18	25.76
65	319.43	242.50	395.80	22.86

APPENDIX D

Determination of Au-Ta speed of sound using resonating cantilever method

D.1 Analysis for speed of sound in Au-Ta nanocantilevers

To extract the speed of sound for a material using the resonating cantilever method first we must recall the results from the Euler-Bernoulli PDE. The flexural modes of a cantilever are described by

$$\omega = \beta^2 \sqrt{\frac{EI}{\rho A}} \quad (\text{D.1})$$

where,

$$\omega = 2\pi f \quad (\text{D.2})$$

and for a rectangular cross section beam,

$$I = \frac{wt^3}{12} \quad (\text{D.3})$$

and for the first mode of resonance,

$$\beta = \frac{3.516}{l^2} \quad (\text{D.4})$$

Of course, the cantilever's length has two components, its designed length, and the undercut that results from wet etch release processing, so l is replaced with $l+u$. Equation D.1 can therefore be simplified to the following

$$f = \frac{t}{2\pi 0.98(l+u)^2} \sqrt{\frac{E}{\rho}} \quad (\text{D.5})$$

This equation can be rearranged to

$$\frac{1}{\sqrt{f}} = (l+u) \sqrt{\frac{2\pi 0.98}{t}} \left(\frac{E}{\rho}\right)^{\frac{1}{4}} \quad (\text{D.6})$$

which has the form of

$$y = mx + b \quad (\text{D.7})$$

A series of lengths of Au-Ta cantilevers had their resonance frequencies assayed, the data was fitted to a Lorentz probability distribution function in order to determine the centre frequency reliably. Error bars were defined according to the resolution of the scan on the spectrum analyzer. The inverse square root of these frequencies were plotted against cantilever length and a least squares linear fit was performed in figure D.1. Note please that the error bars in figure D.1 are so small that their the data point is vastly larger. 20 cantilevers in total were assayed, the data is summarized in table D.1.

From figure D.1 we get a slope

$$m = 220.03952 \pm 0.33124 \quad (\text{D.8})$$

Table D.1: Assayed cantilever data - Au-Ta nanocantilever beams

length μm	frequency Hz	frequency resolution Hz
1	10941100	500
1	10945000	500
2	3673810	125
2	3674050	125
2	3674820	125
2	3674670	125
3	1821240	250
3	1821120	500
3	1821280	250
4	1064090	250
4	1064010	250
4	1064570	250
5	707096.04	140.345
5	707059	140.345
5	707375.33	140.345
7	370507.85	125
7	370468.83	125
7	370482.49	125
7	371897.04	125
8	284884.56	125

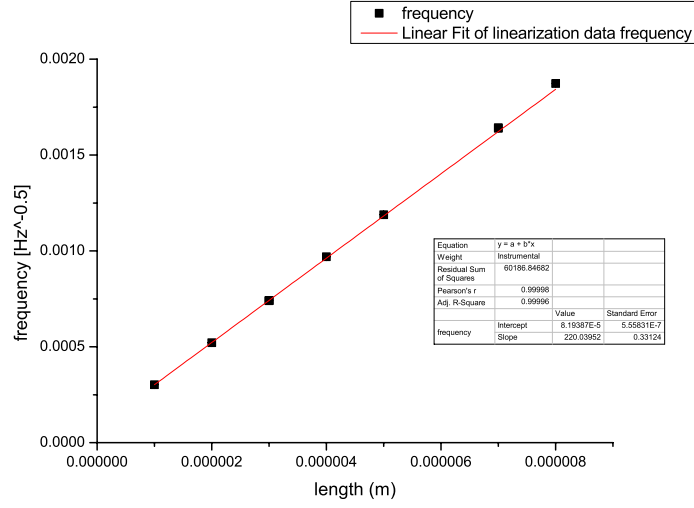


Figure D.1: Plot of inverse square root of frequency versus cantilever length for Au-Ta 5% nanocantilevers

with 95% confidence that

$$219.3436 \leq m \leq 220.73543 \quad (\text{D.9})$$

recalling

$$m = \sqrt{\frac{2\pi \cdot 0.98}{t}} \left(\frac{E}{\rho}\right)^{\frac{1}{4}} \quad (\text{D.10})$$

We attribute a thickness of 51 ± 2.55 nm to the Au-Ta cantilever beams. Using error propagation formulae from (242) we therefore determine that the fractional error in $\sqrt{\frac{E}{\rho}}$ is:

$$\frac{\delta \sqrt{\frac{E}{\rho}}}{|\sqrt{\frac{E}{\rho}}|} = \left(2 \frac{\delta m}{|m|} + \frac{\delta t}{|t|}\right) \quad (\text{D.11})$$

The speed of sound in the Au-Ta cantilevers is therefore:

$$\sqrt{\frac{E}{\rho}} = 2493.64 \pm 132.19 \frac{m}{s} \quad (\text{D.12})$$